Präparation, Charakterisierung und elektronische Eigenschaften von dünnen Schichten des Hochtemperatursupraleiters $HgReBa_2Ca_{n-1}Cu_nO_y$

Dissertation
zur Erlangung des Grades
Doktor der Naturwissenschaften (Dr. rer. nat.)
am Fachbereich Physik
der Johannes Gutenberg-Universität Mainz

von
Abouelwafa Abouelmaaref Mohamed Salem
aus Qena (Ägypten)

Mainz, 2004

Tag der Einreichung: 21.12.2004
Tag der mündliche Prüfung : 06.06.2005

Preparation, Characterization, and Electronic Properties of Thin Films of the High-Temperature Superconductor $HgReBa_2Ca_{n-1}Cu_nO_y$

Ph.D. thesis

by

Abouelwafa Abouelmaaref Mohamed Salem

Mainz, Germany 2004

to my parents, my wife, and Rana

Zusammenfassung

Ziel dieser Arbeit war die Präparation, Charakterisierung und Untersuchung der elektronischen Eigenschaften von dünnen Schichten des Hochtemperatursupraleiters $HgReBa_2Ca_{n-1}Cu_nO_y$, die mittels gepulster Laser-Deposition hergestellt wurden. Die HgRe1212-Filme zeigen in der AC-Suszeptibilität einen scharfen Übergang in die supraleitende Phase bei 124 K mit einer Übergangsbreite von 2 K. Die resistiven Übergänge der Proben wurden mit zunehmender Stärke des externen Magnetfeldes breiter. Aus der Steigung der Arrheniusplots konnte die Aktivierungsenergie für verschiedene Feldstärken bestimmt werden. Weiterhin wurde die Winkelabhängigkeit des Depinning-Feldes $B_{dp}(\theta)$ der Filme gemessen. Hieraus wurde ein Anisotropiewert von $\gamma = 7.7$ bei 105 K ermittelt. Dies ist relevant, um den für Anwendungen wichtigen Bereich im T-B-θ-Phasenraum des Materials abschätzen zu können. Die kritische Stromdichte J_c der dünnen Filme aus HgRe-1212 wurde mit Hilfe eines SQUID-Magnetometers gemessen. Die entsprechenden M-H Kurven bzw. das magnetische Moment dieser Filme wurde für einen weiten Temperatur- und Feldbereich mit einem magnetischen Feld senkrecht zum Film aufgenommen. Für einen HgRe-1212-Film konnte bei 5 K eine kritische Stromdichte von 1.2 x 10^7 A/cm^2 und etwa 2 x 10^6 A/cm^2 bei 77 K ermittelt werden. Es wurde die Magnetfeld- und die Temperaturabhängigkeit des Hall-Effekts im normalleitenden und im Mischzustand in Magnetfeldern senkrecht zur ab-Ebene bis zu 12 T gemessen. Oberhalb der kritischen Temperatur T_c steigt der longitudinale spezifische Widerstand ρ_{xx} linear mit der Temperatur, während der spezifische Hall-Widerstand ρ_{yx} sich umgekehrt proportional zur Temperatur ändert. In der Nähe von T_c und in Feldern kleiner als 3 T wurde eine doppelte Vorzeichenänderung des spezifischen Hall-Widerstandes beobachtet. Der Hall-Winkel im Normalzustand, $\cot\theta_H = \alpha T^2 + \beta$, folgt einer universellen T^2-Abhängigkeit in allen magnetischen Feldern. In der Nähe des Nullwiderstand-Zustandes hängt

der spezifische Hall-Widerstand ρ_{yx} über ein Potenzgesetz mit dem longitudinalen Widerstand ρ_{xx} zusammen. Das Skalenverhalten zwischen ρ_{yx} und ρ_{xx} weist eine starke Feld-Abhängigkeit auf. Der Skalenexponent β in der Gleichung ρ_{yx} =A ρ_{xx}^{β} steigt von 1.0 bis 1.7, während das Feld von 1.0 bis 12 T zunimmt.

Summary

Mercury superconductors possess excellent superconducting properties, even above 77 K. This work studies the preparation, characterization, and electronic properties of thin films of the high-temperature superconductor $HgBa_2Ca_{n-1}Cu_nO_{2n+2+\delta}$. The main goal of this thesis was to achieve a reliable technology for reproducible high quality thin film preparation by understanding the film growth mechanism, the phase formation, and the influence of different synthesis routes with cationic substitutions. Fully textured $(Hg_{0.9}Re_{0.1})Ba_2CaCu_2O_{6+\delta}$ HTSC thin films were successfully prepared by pulsed laser deposition (PLD) of a precursor on (100)-oriented $SrTiO_3$ substrates and then followed by annealing in controlled mercury vapor. The films exhibit sharp superconducting transitions at T_c= 124 K with transition width $\Delta T_c \simeq 2$ K. The resistive transitions and the activation energy of thermally activated flux-motion have been investigated in magnetic fields up to 12 T parallel and perpendicular to the c-axis. The irreversibility line for the $(Hg_{0.9}Re_{0.1})Ba_2CaCu_2O_{6+\delta}$ thin films has been deduced from the electrical resistance measurements and is compared with published data for other high T_c cuprates. At different temperatures magnetization loops were measured with a magnetic field applied normal to the film in a SQUID magnetometer and the corresponding critical current densities J_c were calculated. Under variation of the angle θ between the field direction and the c-axis of the film the anisotropic properties of the vortex state and the depinning field $B_{dp}(\theta)$ have been studied. The films exhibit a rather low critical field anisotropy of 7.7. The angular dependence $B_{dp}(\theta)$ close to T_c resembles the functional form expected for an anisotropic vortex flux liquid, which consists of pancake vortices and in-plane vortex segments. This way of determining the anisotropy yields an effective anisotropy of the material relevant for estimations of the useful range in the T-B-θ phase space of the material. The Hall resistivity (ρ_{xy}) of thin films has been measured in the ab-plane at

up to 12 T. In the mixed state a power-law behavior is observed, where ρ_{xy} scales as a power-law $\rho_{xy} = A\rho_{xx}^{\beta}$, with $\beta = 1.4 \pm 0.1$. Above 130 K the T^{2} dependence of the cotangent of the Hall angle is observed. The total Hall conductivity for these compounds is well described by $\sigma_{yx}(B) = C_1/B + C_2B + C_3$.

Contents

List of Figures

List of Tables

Introduction

0.1 A short history of superconductivity

Firstly, a short historical account of some important discoveries in the field of superconductivity and of the gradual increase of the superconducting critical temperature T_c in time is given.
Superconductivity received a lot of media coverage following the discovery of the high T_c superconductors by J. G. Bednorz and K. A. Müller in 1986 [1]. Many non-physicists therefore have the conception that superconductivity is a new scientific phenomenon. However, superconductivity was first discovered by H. Kamerlingh Onnes [2] at the University of Leiden, Netherlands in 1911. He observed that the resistivity of mercury abruptly vanishes when it is cooled to very low temperatures. With this observation, the field of superconductivity was born. The next year Onnes discovered that application of a sufficiently strong axial magnetic field restored the resistance to its normal value. The low temperature needed to reach the superconducting state in the elements of the periodic table prevented the observation until helium had been liquefied by Onnes in 1908 in his laboratory at Leiden, which provided a medium to cool experimental objects to just a few degrees above absolute zero. Also for lead, tin, and aluminum, the electrical resistance disappears completely in a narrow temperature range at a critical temperature T_c (typically a few Kelvin) specific to each metal. The transition temperatures were too low to allow for any realistic applications. The theoretical situation was equally frustrating for a long time. No microscopic understanding was developed during the first 40 years. It is natural to wonder why superconductivity represents such a difficult problem in physics that forty six years had to pass before it was finally solved in principle. For almost twenty years the physics community did not possess the basic building blocks needed to

formulate a solution — the quantum theory of normal metals. It was not until 1934 that a key experiment was performed, the demonstration by W. Meissner and R. Ochsenfeld [3] that another basic property of a superconductor was its perfect diamagnetism, its ability to shield out an external magnetic field of modest size in a microscopic distance. The Meissner effect implies a critical field H_c, above which superconductivity is destroyed. Once the building blocks were in place, it quickly became clear that the characteristic energy associated with the formation of the superconducting state is tiny, roughly a ten thousands of the normal state characteristic electronic energies. Theorists focussed their attention on developing a phenomenological description of superconductivity. The way was led by Fritz London [4], with his brother, Heinz, who pointed out that superconductivity is a quantum phenomenon on a macroscopic scale. The next theoretical advance came in 1950 with the theory of Ginzburg and Landau [5], which described superconductivity in terms of an order parameter and provided a derivation for the London equations. In the same year H. Fröhlich [6] pointed out that two electrons could be attracted to each other via a phonon interaction and suggested that the transition temperature T_c would vary with M, where M is the atomic mass. This was experimentally confirmed the same year by the discovery of the isotope effect (IE), i.e., the proportionality of T_c to $M^{-\alpha}$ for isotopes of the same elements [7, 8]. The isotope effect provided support for the electron-phonon interaction mechanism of superconductivity. The late fifties and early sixties marked a first period of theoretical success. The BCS theory proposed by J. Bardeen, L. Cooper, and J. R. Schrieffer in 1957 [9] put the phenomenon on firm theoretical ground. This theory is based on the assumption that the supercurrent is not carried by single electrons, but rather by pairs of electrons of opposite momenta and spin, the so-called Cooper Pairs. All pairs occupy a single quantum state, the BCS ground state, whose energy is separated from the single-electron states by an energy gap that can be related to T_c. The Ginzburg-Landau [5] and London [10] results fit well into the BCS formalism. The discovery of the Josephson effects [11] led to physical insights and to several commercial products. Alloys and compounds have been extensively studied, especially the so-called *A15* compounds, such as Nb_3Sn, Nb_3Ga, and Nb_3Ge, which held the record for the highest transition temperatures from 1954 to 1986. The highest known critical temperature was raised successfully towards the long standing record of

23 K in Nb_3Ge, discovered in 1973 [12]. Many other types of compounds have been studied in following years, particularly the so-called heavy fermion systems in which the superconducting electrons have high effective masses of 100 m_e or more. Despite strong efforts the critical temperature was not further raised for more than 10 years. With this background in mind one can understand that the superconductivity discovered in the Ba-La-Cu-O system [1] caused a lot of excitement. Soon many other researchers became active, and the recorded transition temperature began a rapid rise. By the beginning of 1987, scientists had fabricated the lanthanum compound, which went superconducting at close to 40 K at atmospheric pressure [13, 14] and at up to 52 K under high pressure [15]. Soon thereafter, and in the year after that pioneering work in the Ba-La-Cu-O system a new cuprate with T_c above 90 K was discovered by Wu et al. [16] in the yttrium-barium system. This discovery was soon followed by others [17, 18]. Superconductivity reached 105 K with the discovery of the Bi-Sr-Ca-Cu-O system [19], and then the 120-125 K range in the Tl-Ba-Ca-Cu-O system [20, 21, 22, 23]. Berkley at al. [24] reported $T_c = 131.8$ K for $Tl_2Ba_2Cu_3O_{10-x}$ at a pressure of 7 GPa. Several researchers [25, 26, 27, 28, 29] have reported T_c above 130 K for the Hg series of compounds $HgBa_2Ca_{n-1}Cu_nO_{2n+2+\delta}$, where n is the number of CuO_2 layers per unit cell, sometimes with Pb doping for Hg. Today the highest known T_c at atmospheric pressure is about 135 K in $HgBa_2Ca_2Cu_3O_{8-\delta}$ [27] and 138 K for samples with a nominal composition of $Hg_{0.8}Tl_{0.2}Ba_2Ca_2Cu_3O_{8+\delta}$ [30]. High pressure has been employed extensively in the study of high T_c superconductivity, where the transition temperature increases by applying pressure [31, 32, 33, 34, 35]. At high pressure of 30 GPa the superconducting transition temperature T_c for the $Hg_{1-x}Pb_xBa_2Ca_2Cu_3O_{8+\delta}$ compound increases to above 164 K, the highest up to date [35]. Since the discovery of high T_c cuprate superconductors the field has grown enormously and attracted many scientists. A large number of new high T_c oxide superconductors have been found. Magnesium diboride (MgB_2) is a new superconducting material outside the cuprate family with a critical temperature of about 39 K. The material was discovered in January 2001 [36], and it soon attracted the interest of many research groups. Extremely interesting is that MgB_2 is a simple metallic compound with a relatively high T_c. The period from 1930 to 1986 can be called the Niobium Era of superconductivity because the niobium compounds such as NbTi and Nb_3Sn had dominated

the field of superconducting applications. The new period that began in 1986 is the Copper Oxide Era because, thus far, the presence of copper and oxygen has, with rare exceptions, been found essential for T_c above 40 K. While MgB_2 seems to be well described by BCS theory, much of the theoretical debate still centers whether BCS theory can also explain the properties of high-temperature superconductors.

Superconductors are grouped according to their transition temperature: low-temperature superconductors (LTS or conventional superconductors) have transition temperatures (T_c) of 23 K(Nb_3Ge) or below. These materials are cooled by liquid helium with a boiling point of 4.2 K. The term high-temperature superconductors (HTSCs) is used for compounds that remain superconducting above the boiling point of nitrogen, 77 K.

It is also interesting to observe that mercury was the first known superconductor, and now 92 years later mercury compounds have become the ones with highest T_c values.

Chapter 1

Fundamentals of high-T_C superconductivity

1.1 Basic properties of superconductors

The purpose of this chapter is to describe the fundamental properties of superconductivity and to make an introduction to high-T_c superconductivity and its applications.
Interesting applications of superconductors use four phenomena:
(i) the absence of resistivity, used for the transmission of electricity without losses and the generation of large magnetic fields,
(ii) the nonlinear transition from the superconducting state to normal conductance, applied in fault current limiters,
(iii) the diamagnetic behavior, applicable for bearings in connection with permanent magnets, and
(iv) phase coherence is exploited in superconducting quantum interference device (SQUID). It involves quantum tunnelling between two SC, is a highly sensitive instrument employed for non-destructive measurements of magnetic fields, with a host of applications in both biophysics and materials technology.
Superconductors possess a unique collection of physical properties which are definitely well known.

1.1.1 Zero resistivity

Zero resistivity is the property that has given the name to superconductivity. In a superconducting metal, zero resistivity means that there is no voltage drop along the metal when a current is passed through, and by consequence no power is dissipated. In normal metals, when a current is passed, losses will occur due to scattering effects. At high temperatures phonon scattering dominates. Decreasing the temperature reduces the number of phonons and the resistivity decreases accordingly. At low temperature impurity scattering will finally dominate and the resistivity saturates. However, for superconductors the resistance will abruptly fall to zero with decreasing temperature at a critical temperature T_c.

1.1.2 Meissner-Ochsenfeld effect (Perfect diamagnetism)

Superconductors have a unique combination of electric and magnetic properties. Diamagnetism is the ability of a body to repel a magnetic field, characterized by negative susceptibility values (χ) ranging from 0 to -1. Meissner and Ochsenfeld measured the flux distribution of metal superconductors, cooled down to their T_c while in a magnetic field [3]. Surprisingly, they found out that a metal in the superconducting state never allows a magnetic flux density to exist in its interior, i.e. the Meissner-Ochsenfeld effect is the perfect diamagnetic behavior of a superconducting material and inside superconductors the magnetic induction is zero, $B = 0$. This is a true material property of the superconductor and essential for superconductivity as a thermodynamic phase. In contrast to a perfect conductor the interior of a superconductor is field free independent of the history of cooling and field application. A perfect conductor will prevent a magnetic field from penetration upon field changes due to the induction law. However, if a magnetic field is applied in the normal state it will penetrate. Cooling below the critical temperature, where only perfect conductivity exist, will not induce any screening currents. Therefore the field will not be repelled in a field cooled (fc) experiment for a perfect conductor, but it will be repelled for a true superconductor.
Two years after this discovery, H. and F. London [4] proposed an equation which offered a phenomenological description of the Meissner-Ochsenfeld effect.

1.1.3 Critical magnetic field

Both current and magnetic field have a profound effect upon the characteristics of a superconducting material. At any given temperature, $T < T_c$, there is a certain field $H_c(T)$, called the critical field, the maximum amount of magnetic field that a superconductor can experience and remain in the superconducting state. Higher fields will quench the superconductivity. The temperature dependence of $H_c(T)$ near T_c is approximately given by

$$H_c(T) = H_c(0)[1 - (T/T_c)^2]. \tag{1.1}$$

This critical field can be attained via two different mechanisms. There is the externally applied magnetic field that has already been mentioned, the other contribution to the critical field can come from current transport through the material itself, generally being supplied from an external source.

1.1.4 Penetration depth and coherence length

It was mentioned previously that screening currents form upon the surface of a superconductor when a magnetic field is applied to the material, these currents generate a field, which everywhere is equal but of opposite direction of that being applied. As there is no flux density in the body of the superconductor then it stands to reason that there cannot be any current flowing through the material. This is why it is said that the current is restricted to flow over the surface, but this current simply cannot exist within an infinitely small layer, as the current density would be infinite. To be more exact, the field does exist inside a surface layer of a thickness, which is called the penetration depth λ. This depth varies with different materials. Within this layer the magnetic induction $\overrightarrow{B}$ decreases exponentially from its external value to zero

$$B(x) = B_0 \exp(-x/\lambda) \tag{1.2}$$

where it is assumed that the external magnetic field is parallel to the surface of the sample. B_0 is the value of the magnetic field at the surface and x is the distance from the surface. The penetration depth λ is given by

$$\lambda = \sqrt{\frac{m}{\mu_0 n e^2}} \tag{1.3}$$

and n is the density of superconducting electrons. Typical values of λ range from 10 to 100 nm.

The penetration depth varies with temperature according to the empirical formula:

$$\lambda(T) \approx \lambda_0 \frac{1}{\sqrt{1-(\frac{T}{T_c})^4}} \tag{1.4}$$

where λ_0 is the penetration depth at 0 K. $\lambda(T)$ becomes infinite as T approaches T_c, so $\lambda \to \infty$ at $T \to T_c$, i.e., the applied magnetic field penetrates more into the sample.

One of the characteristic lengths for the description of superconductors is called the coherence length ξ. It is the characteristic length scale over which the Cooper pair density can change, and an important parameter in determining the class of superconducting material. It is related to the Fermi velocity for the material and the energy gap associated with the condensation to the superconducting state. For most pure superconducting metals, the coherence length is around 1000 nm, which is around an order of magnitude greater than the penetration depth λ of the material, this behavior will characterize the superconductor as type-I. The coherence length in a type- II superconductors is shorter than the penetration depth. Both $\lambda(T)$ and $\xi(T)$ vary as $(1 - T/T_c)^{-1/2}$ with temperature, so that their ratio is independent of temperature,

$$\kappa = \frac{\lambda(T)}{\xi(T)} \tag{1.5}$$

κ is known as the Ginzburg-Landau parameter. A precise calculation from the microscopic theory gives a weak temperature dependence for κ, with κ increasing as T decreases [37]. In Ginzburg-Landau (GL) theory, a superconductor is called type-Iif $\kappa < 1/\sqrt{2}$ and type-IIif $\kappa > 1/\sqrt{2}$.

1.2 Type-I and type-II superconductors

1.2.1 Type-I superconductors

There are two types of superconducting materials. The elemental superconductors such as titanium, aluminium, tin, mercury, lead, zinc and others, were the first superconductors to be discovered and have been later classified as type I

superconductors. The identifying characteristics are zero electrical resistivity below a critical temperature T_c, zero internal magnetic field (Meissner effect), and a constant critical magnetic field $H_c(T)$ for any given temperature. Type I superconductors have been of limited practical usefulness because the critical magnetic field are so small and the transition from superconducting to normal state is sharp when an external magnetic field is applied and the superconducting state disappears suddenly above $T_c(H)$, i.e., no transition region is found. For a type-II material, this behavior has a higher degree of complexity.

1.2.2 Type-II superconductors

A significant contribution to the theory of superconductivity was made by the Russian physicist Alexei A. Abrikosov in 1957 (Nobel-prize 2003) when he published a paper describing some new phenomena related to the Ginzburg-Landau (GL) theory, quite different from the behaviour of the earlier type-I superconductors [38]. He pointed out the existence of some new materials, which exhibit a continuous increase in flux penetration starting at a first critical field H_{c1} with reaching $B = \mu_0 H$ at a second critical field H_{c2}, instead of showing a discontinuous disappearance of superconductivity at the thermo-dynamical field H_c. While the class of type-I superconductors is composed entirely of metallic chemical elements, type-II superconductors may be metal alloys or even some pure metals, such as Niobium (Nb) and Vanadium (V), and also different oxide compounds.

Vortex state and phase diagram of a type-II superconductor

Below T_c, in the presence of an externally applied magnetic field H, three distinct phases are recognizable, dependent on the strength of the applied field. Below a lower critical field H_{c1} the superconductor is in the Meissner state with full expulsion of magnetic flux from its interior. For an applied field above an upper critical field H_{c2}, magnetic flux fully penetrates the type-II material and returns it to its normal state. If the applied field lies between H_{c1} and H_{c2}, there is a partial penetration of flux into the sample leading to regions in the interior which are superconducting and others which are in the normal state; this is often referred to as the mixed state or the vortex state, which allows the existence of normal regions in the material. In the vortex state there are cores of material with normal conductivity of radius ξ surrounded by superconductive material. As the

magnetic field increases the density of vortices in the superconductor increases until the normal cores overlap. In the vortex state, the Meissner effect is no longer present and magnetic flux may partially penetrate the superconductor; the superconductivity, however, is not lost. The existence of the mixed state or the vortex state can be explained by the fact that the material always tends to assume the state with lowest total free energy and when the surface energy between normal and superconducting regions is negative, the appearance of normal regions will reduce the total free energy and lead to a more favorable energy state [39]. It turns out that the configuration in which the ratio of surface to volume of normal material is a maximum is a cylindrical normal region, parallel to the external field and threading the superconductor, as shown in Fig. 1.1. These cylindrical normal cores are arranged in a regular pattern, forming a lattice, sometimes called fluxon lattice. It was predicted by Abrikosov that the magnetic flux would penetrate in a regular array of flux tubes, named fluxons, each one having the quantum of flux $\Phi_0 = h/2e = 2.6678 \times 10^{-15}$ Wb (h = Planck's constant and e = electron charge).

Abrikosov considered the case where the externally applied magnetic field H is only slightly below H_{c2}; for in this region one obtains approximate solutions resembling those of the linearized GL equations [41]. The solutions reveal the presence of a periodic microscopic magnetic field distribution, transverse to the applied field. More precisely, his efforts predict a periodic square array of thin filaments of magnetic flux in the mixed state. Consequently, literature sometimes refers to the mixed state as the Abrikosov regime or for reasons soon to be made apparent, the vortex state. In the core region of a filament, the magnetic field is high and the material is not a superconductor; that is these regions are in the normal state. The magnetic field is screened from the rest of the sample by supercurrents which circulate around each filament. It is common to refer to the filaments as vortex lines and the array of filaments as a vortex lattice. At the vortex center where the magnitude of the local field is largest, the density of superconducting electrons n_s and hence the order parameter $\Psi(\vec{r})$ is zero. As one moves radially out from the center of a vortex core, n_s increases and the supercurrents screen a greater amount of flux. At a radius of the order of the coherence length $\xi(T)$, n_s approaches the value in the bulk of the sample.

Abrikosov calculated the relation of the lower (H_{c1}) and upper (H_{c2}) critical field

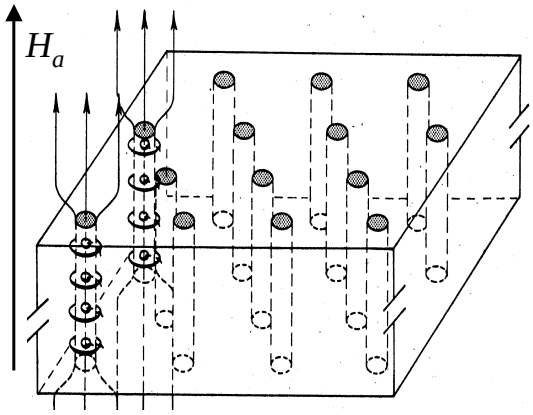

Figure 1.1: *Schematic representation of the mixed state. Magnetic field and supercurrent are only illustrated for two flux tubes [40].*

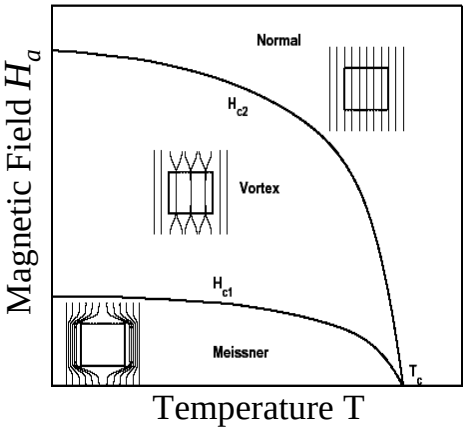

Figure 1.2: *Phase diagram of a type-II superconductor.*

to the thermodynamical critical field H_c for type-II superconductors as follows:

$$\begin{aligned} H_{c1} &\simeq H_c/\kappa \\ H_{c2} &\simeq \sqrt{2}\kappa H_c \end{aligned} \tag{1.6}$$

In the classic pure superconductors, $\kappa < 1$, but in dirty superconductors or in high-temperature superconductors, κ may be much greater than 1 [5].
Several years after Abrikosov, the irreversible magnetization of type-II superconductors was experimentally described by Bean [42, 43]. He presented a macroscopic model of the current and magnetic flux distribution, and showed that the flux penetration in such materials is not uniform in the presence of pinning, there is a flux density gradient. Bean's model has been named the critical state model. Figure 1.2 shows the phase diagram of a Type-II superconductor.
Most applications such as Magnetic Resonance Imaging (MRI) magnets require type-II superconductors such as niobium-titanium alloys and the newly discovered high-temperature superconductors, which all work in the presence of strong magnetic fields.

Magnetization of type-II superconductors

The sketch in Fig. 1.3-a shows that in an ideal type-II superconductor H and M are uniquely related to one another and the magnetization curve is reversible. The state of perfect diamagnetism, $B = \mu_0(M + H) = 0$, exists only below H_{c1},

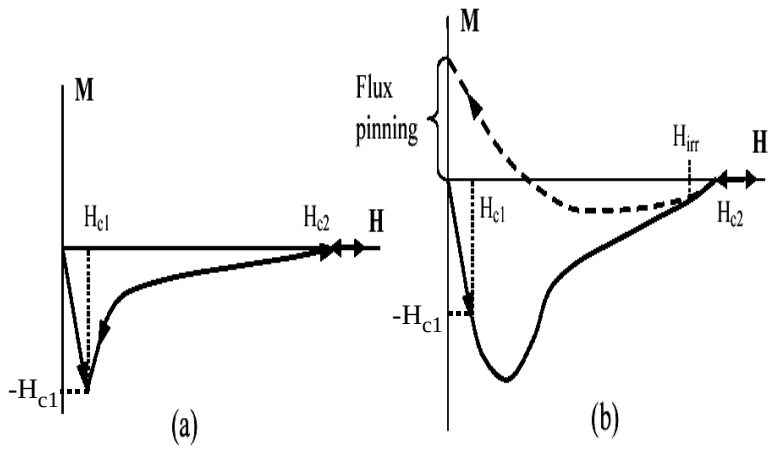

Figure 1.3: *(a) Magnetization of ideal type-II superconductor. The state of perfect diamagnetism exists below H_{c1}. Above H_{c2} the material is in normal state. (b) Magnetization of real type-II superconductor, the curve is reversible only above H_{irr}. The magnetic flux at $H = 0$ is trappedör pinnedïn the material [44].*

afterwards the flux starts to penetrate, and above H_{c2} there is no magnetization at all and the material returns to its normal state. As the magnetic field is decreased below H_{c2}, the reverse magnetization path will exactly retrace the forward one. However, no real material exhibits the exact retracing of the idealized curve. Structural imperfections or chemical impurities act as barriers for flux movement into the crystal; this is referred to as flux pinning. As a matter of fact, it is the practical goal of material engineers to introduce as many pinning sites as possible in order to allow high currents to flow under high magnetic fields. A real type-II superconductor has a more complicated magnetization path, which is depicted in Fig. 1.3-b. The noticeable difference is the absence of a sudden change in the magnetization M as H passes through H_{c1}. Only the slight deviation from linearity conveys that the diamagnetic state is no longer perfect, and that flux has started to penetrate into the material. The increase of H leads to more extensive flux penetration, and at H_{c2} the state of full penetration is achieved, $B = \mu_0 H$ and the material becomes normal. In the superconducting state, some of the flux is trapped within the material. After reaching H_{c2}, when H is reduced, flux lines are free to move at first, and so the $H - M$ curve retraces its path until a point H_{irr}, the irreversibility field, when flux pinning becomes

stronger, B declines slower than H, and M deviates from the forward curve. As H is further decreased, B remains high and since $B = \mu_0(H + M), M$ rises to a positive value. At the end of the reverse cycle, when $H = 0$, the value of B remains finite due to the flux trapped by the superconductor.

Flux pinning, creep and flow

In a perfectly pure material, the flux lines would be able to easily move and adjust their density according to the applied field. However, due to impurities and inhomogeneities in type-II superconductors, the fluxons are pinned and an energy barrier is created that has to be overcome in order to move them. Flux pinning can be imagined as if the fluxons are situated in pinning wells of depth U_0 (pinning energy or strength) and placed at a given distance, which the fluxons need to jump from one well to another, see Fig. 1.4.

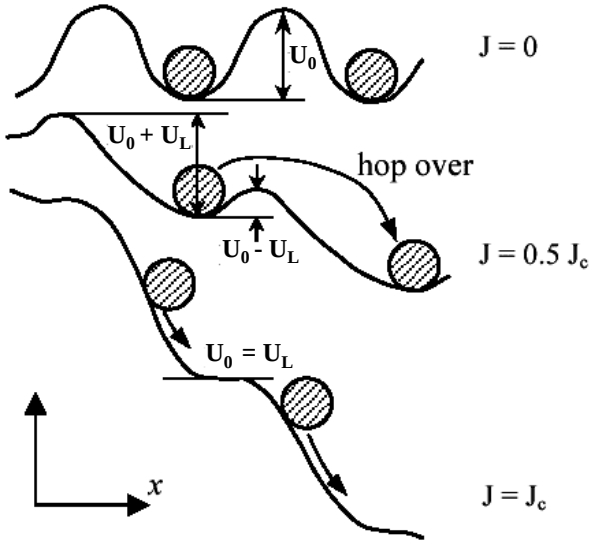

Figure 1.4: *The mechanism of flux-flow. The presence of current in a magnetic field generates a Lorentz force, which tilts the potential, so it turns into a staircase. This allows the flux lines to hop out of their pinning wells more easily. The upper curve shows the pinning potential in the absence of any applied force (unperturbed potential U_0), and the lower curve shows depinning with an applied current for a given external magnetic field B ($U_0 = U_L$) [44, 45].*

When electric current with density **J** is carried by a type-II superconductor, it passes the flux lines and creates a Lorenz force $\mathbf{f}_\mathrm{L} = \mathbf{J} \times \Phi_0$ upon each vortex.

The fluxons will remain in place as long as their pinning strength U_0 is larger than the Lorenz potential U_L, however, the effective depth of the pinning wells gets smaller with the increase of $\mathbf{J}$. At a certain value J_c, the Lorentz force will become greater than the pinning energy, and all fluxons will start to move, see Fig. 1.4. This movement is referred to as flux-flow. J_c is called the critical current density and is a very important characteristic, since it gives the maximum current the superconductor can carry. Above J_c the material becomes normal again. The study of vortex dynamics in high-temperature superconducting (HTSC) materials has both fundamental and technological importance. For example, the materials must provide strong vortex pinning in order to transport large current without power dissipation. In HTSC materials, thermally activated depinning of the flux line introduces severe problems for their application [46]. One of the common methods used to investigate the vortex dynamics is to study the measured voltage-current or resistivity-current density characteristics. The motion of flux lines in the mixed state of type-II superconductors gives rise to energy dissipation in the material, and therefore the term flux-flow resistivity has been coined. The origin of energy dissipation is the Lorenz force. If the flux line is not well pinned, it will then move in a direction transverse to the current under the effect of $\mathbf{f}_\mathrm{L}$. The movement of the flux line with velocity $\mathbf{v}_\mathrm{L}$ will induce an electric field $\mathbf{E} = \mathbf{B} \times \mathbf{v}_\mathrm{L}$, which is parallel to $\mathbf{J}$ and acts like a resistive voltage causing power dissipation. In HTSCs, certain flux motion may be activated by thermal fluctuation of the fluxon lattice; this motion is slower and more sporadic and has been named flux-creep.

1.3 Epitaxially grown cuprate films on single crystalline oxide substrates

The structure of epitaxially grown films is of importance for many areas of technology. Various thin-film technologies are well established for high quality semiconductor growth today. Similar methods cannot be applied directly to the growth of oxide films because of particular features related to their complex and often anisotropic crystal structures which contain a relatively large number of elements in addition to oxygen. Fortunately, high-T_c superconducting materials are layered

and, with the development of advanced growth techniques, they allow engineering of oxide films at an atomic level to some extend. The field of epitaxial oxide films has greatly advanced over the last decade, driven by the need to synthesize high quality films of high-T_c superconductors (HTSCs). Small changes of parameters like chemical composition, temperature and pressure may drastically modify the physical properties of a transition metal oxide compound. Pressure can be employed to induce remarkable changes in the electronic structure and properties. For example, the transition temperature towards the superconductive state in $Hg_{1-x}Pb_xBa_2Ca_2Cu_3O_{8+\delta}$ increases from 133 K at ambient pressure to 164 K at 30 GPa [35], the highest up to date. Effects similar to those induced by high pressure, i.e., the modification of the crystalline and electronic structure, can be also attained by epitaxial growth. One important difference between epitaxially grown thin films and the bulk compound is that the lattice mismatch between film and substrate induces strain in the film. This may substantially modify the physical properties of the material. There is of course a basic difference between epitaxial and hydrostatic strain. In epitaxial growth, the sample is allowed to expand or contract along the direction perpendicular to the surface. This implies that the unit cell of the film is slightly deformed, e. g., a cubic cell becomes tetragonal. This effect may also induce changes of certain physical properties. For the development of a reliable deposition technology for high-quality HTSC thin films, the choice of the substrate material is of primary importance. Thin films are usually grown on single crystal substrates for which the lattice parameters are different from those of the material of the film as in its bulk form. As for defects, the situation for substrates suited for HTSC deposition is still far away from the level reached in Si technology. Nevertheless, $SrTiO_3$ (STO), $LaAlO_3$ (LAO), $NdGaO_3$ (NGO), MgO and Yttria-stabilized Zirconia (YSZ) have reached a certain standard. For STO, even atomically flat substrates are available [47, 48]. The basic requirements for the substrates can be summarized as follows:

- Crystallographic lattice match between HTSC film and substrate. Substrates have to provide a suitably lattice-matched crystal matrix to align the HTSC grains in uniform orientation. Most suitable for applications is the c-axis orientation of the HTSC films where the CuO_2 planes are parallel to the substrate which preserves the isotropy of the electrical properties in the film plane. Fortunately, this film orientation is promoted by the faster

growth of HTSC films along the CuO_2 plane directions compared to the c-axis direction.

- Similar thermal expansivities of HTSCs and substrate, matching of the thermal expansion coefficients of the substrates and the HTSC films is an additional requirement since the HTSC deposition takes place at 900 K to 1200 K, with the application temperature below 100 K.

- No chemical interaction are required at the interface between HTSC film and substrate.

- Suitably polished surface, which are stable and reasonably robust must be used.

1.4 Aim of this work

Presently, four groups of HTSC are being considered for application: $YBa_2Cu_3O_{7-\delta}$ (YBCO), $Bi_2Sr_2Ca_{n-1}Cu_nO_{2n+4+\delta}$ (BSCCO), $Tl_2Ba_2Ca_{n-1}Cu_nO_{2n+4+\delta}$ (TBCCO), and $HgBa_2Ca_{n-1}Cu_nO_{2n+2+\delta}$ (HBCCO). Each of these four groups contains several superconducting phases, numerous cation substitution, and many different processing methods. This work is concerned with the $HgBa_2$ $Ca_{n-1}Cu_nO_{2n+2+\delta}$ family of superconductor thin films.
The discovery of superconductivity in the mercury based $HgBa_2Ca_{n-1}Cu_nO_{2n+2+\delta}$ cuprates has attracted considerable interest due to their record high superconducting transition temperatures [49]. These high critical temperatures suggest the possibility of superconducting applications at 77 K and even a few degrees above. However, the highly volatile nature and toxicity of HgO, combined with the complexity of processing, has retarded the development of thin film technology, though high-performance grain-boundary Josephson junctions and dc superconducting quantum interference devices (SQUIDs) have been fabricated using c-axis oriented (Hg, Re)$Ba_2CaCu_2O_y$ thin films grown on bicrystal $SrTiO_3$ substrates [50]. Also critical current densities at 77 K on the order 10^5 A/cm^2 and irreversibility fields of $\mu_0 H_{irr}$ (100 K) = 0.5 T demonstrate the great potential of these superconductor materials for applications [51]. The Hg-based family has several important features, such as relatively simple structures, the possibility to

vary T_c in a wide range by reducing/oxidizing gaseous treatment etc. Therefore, they can be considered as excellent objects to study superconductivity phenomena in Cu-based oxides. At present there are only about one dozen research groups in the world involved in the development of Hg-based films. In this work the transport properties by measuring the resistivity and magnetization of epitaxial $HgBa_2Ca_{n-1}Cu_nO_{2n+2+\delta}$ films are investigated.

Because of the reactivity and the toxic nature of the Hg-based compounds, the synthesis of the Hg-based superconductors requires extraordinary care during all steps of the sample preparation to minimize the detrimental effect of air. This results in a poor reproducibility as well as a poor stability of the Hg-based HTSC thin films and has hindered research and application. A systematic study is therefore necessary to overcome these difficulties.

The main goal of the thesis was to yield a dependable technology for reproducible high quality thin film preparation. This was achieved by understanding the film growth mechanism, the phase formation, and the influence of different synthesis routes with cationic substitutions.

Chapter 2

Mercury-based superconductors

Since the discovery of high temperature superconductivity [1], many cuprate superconductors with a variety of T_c values have been found. It is one thing to demonstrate the existence of HTSC by making a sample in a laboratory with a mortar and pestle and a simple furnace. It is quite another to prepare samples with superconducting properties good enough for scientific and applied studies. The latter requires great effort dedicated to synthesis. This is attributed to the complex chemistry of the high temperature superconducting compounds. Fortunately, various techniques have been adapted or developed successfully for the synthesis and fabrication of high quality HTSC materials in various forms, from polycrystal to single crystal, from bulk to thin film, and from disk to wire, for scientific pursuit and device development. Since the discovery of Hg-based superconducting Cu mixed oxides, $HgBa_2Ca_{n-1}Cu_nO_{2n+2+\delta}$, in 1993 [27, 49], a lot of papers have been published illustrating different chemical and structural characteristics of these materials. The goal of the present chapter is to review some important chemical and structural features of the Hg-based family, with special attention to the structure property relationship.

2.1 General aspects of the crystal structure of cuprate superconductors

All HTSCs known so far are ceramics and their common structural elements are copper-oxide planes, in which the supercurrent flows, and insulating lay-

ers that separate blocks of 1 to 7 copper-oxide planes. These materials are highly anisotropic, and therefore the microstructure of a polycrystalline conductor strongly influences the properties. The main structural features of Cu-based superconductors have been described in numerous papers and can be summarized as follows:

(1) The copper-oxygen layer (CuO_2) is the main structural unit, which is responsible for the appearance of superconducting properties. Copper atoms in this layer have square or near square coordination, the squares are joined together by common vertices, forming infinite (CuO_2) layers.

(2) Formal copper valence should be between +2.05 and +2.25 or between +1.8 and +1.9 for the appearance of superconductivity in HTSCs where conductivity of carriers by holes.

(3) The in-plane Cu-O distance is another important structural parameter for the appearance of superconducting properties. In order to form delocalized carriers in the partially filled conductivity band, the Cu-O distance should be in the 1.88−1.97 Å range. Copper atoms can be bonded to oxygen atoms located in neighboring layers, but these bonds should be significantly longer, and weaker, than in-plane ones, thus providing a layered type of structure. Complex copper oxides with three-dimensional network structures (Cu-O bonds have close distances in all three dimensions) have not yet been shown to be superconductors.

This negatively charged CuO_2 layer should be placed in the structure between positively charged or neutral cation oxygen layers such as (AO) or (A□) (□: oxygen vacancy) layers.

Intergrowth structures are built of different structural blocks, alternating along the longest period of the unit cell: a perovskite block with superconducting CuO_2 layers, a rock salt block and/or a fluorite block, and structurally matched to so-called blocking layers (charge reservoir), which contain different structural elements (Ba-O, Bi-O, Hg-O, Sr-O, Tl-O, CO_3 layers, Cu-O chains, etc.). The insulating layers provide conditions for the stability of the structure compensating the negative charge of the perovskite block, and in particular create the necessary carrier concentration in the conducting band. In $(La,Sr)_2$ CuO_4 [1], the ratio between La and Sr acts as charge balance (reservoir). The charge reservoir layer is responsible for donating charge to or accepting charge from the superconducting layer to achieve a proper hole concentration. In addition the oxygen content

in some charge reservoir layer is variable and is usually affected by oxidizing or reducing atmospheres during synthesis. The high-temperature cuprate superconductors have been known to have strong dependence of the superconducting transition transition temperature T_c on the hole concentration in the CuO_2 planes (n_h) and the number of CuO_2 planes (n) in the SC blocks. In general, they evolve from an insulator through a superconductor to a normal metal with the increase of n_h [52]. It is established that in the layered cuprates the T_c increases with increasing n up to $n = 3$. A simple model of HTSC is, that the CuO_2 planes act as electrical conductors, whereas the intermediate parts function as charge reservoirs, supplying charge to the participate in the CuO_2 planes. The charge carrier density in the CuO_2 planes, or the deviation of the formal Cu^{2+} valence, is a primary parameter determining the superconducting transition temperature T_c in the homologues HTSC family [53]. The carrier concentration in the CuO_2 layers can be adjusted by varying the oxygen content or by chemical substitutions outside the CuO_2 planes. Various defects in the CuO_2 planes or adjacent layers lead to a lower T_c. In most cases, at least for the highest transition temperatures, the charge carriers are holes.

2.2 Hg-based superconductors and their crystal structure

It is assumed that in the layered high-T_c superconductors (HTSC) $Bi_2Sr_2Ca_{n-1}Cu_n O_{2n+4+\delta}$ (BSCCO), $Tl_2Ba_2Ca_{n-1}Cu_nO_{2n+4+\delta}$ (TBCCO), and $HgBa_2Ca_{n-1}Cu_n O_{2n+2+\delta}$ (HBCCO) the superconductivity in a unit cell is located in blocks of n closely spaced CuO_2 layers intercalated by Ca [54]. Each of these high-T_c superconductors contains several superconducting phases, numerous cation substitution, and many different processing methods. This work is concerned with the $HgBa_2Ca_{n-1}Cu_nO_{2n+2+\delta}$ (HBCCO) family of superconductor thin films. The structure of all these compounds is relatively simple and, their transition temperatures T_c are the highest observed. Thus, this homologous series is a very good candidate for studies.

The cuprate superconductors can contain different numbers of Cu-O layers. To make this possible, an extra intermediate layer of the smaller alkaline-earth (AE)

metals has to be added. Structures differing by one Cu layer and the extra AE layer are called homologues of the same family. Like other families of known high-temperature superconducting ceramics [16, 19, 55], the Hg superconductor contains several superconducting phases of $HgBa_2Ca_{n-1}Cu_nO_{2n+2+\delta}$, with n = 1, 2, 3,... [32], n is the number of Cu-O layers. To date, n = 1.....6 members of the $HgBa_2Ca_{n-1}Cu_nO_{2n+2+\delta}$ homologous series, have been identified, Hg-1201 (T_c =97 K) [49, 56], Hg-1212 (T_c =128 K) [56, 57, 58], Hg-1223 (T_c =135 K) [27, 58], Hg-1234 (T_c =127 K) [59], Hg-1245 (T_c =110 K) [60], Hg-1256 [61] (T_c =107 K). There exists another homologous series $Hg_2Ba_2Ca_{n-1}Cu_nO_{2n+4+\delta}$, with n = 2...4, Hg-2212 (T_c =44 K) [62, 63], Hg-2223 [64, 65] (T_c =44 K) , Hg-2234 (T_c =114 K) [64]. $Hg_mBa_2Ca_{n-1}Cu_nO_{2n+2+m+\delta}$, where m = 1, 2 and n = 1, 2, 3,..., is general formula of all superconducting mercury cuprate members. All these homologous have a similar free energy and in a solid state reaction starting from a definite stoichiometric composition, it is difficult to achieve a phase pure sample. In addition to the dominant Hg superconducting phase the homologous phases can also form even within the same crystallite. The phase content of each member in the fabricated sample depends on a number of fabrication factors such as the sintering temperature, the molar ratio of Hg, Ba, Ca and Cu chemical oxides and the sintering time [66, 67]. The first member of the series, namely $HgBa_2CuO_{4+\delta}$ (Hg-1201) with n=0, has no [–Ca] layer and a relatively low transition temperature of 97 K, which is the highest of all single-layered compounds. The highest known transition temperatures have been found at atmospheric pressure is about 135 K in $HgBa_2Ca_2Cu_3O_{8-\delta}$ [27]. The first mercury-bearing compound $HgBa_2RCu_2O_{6-\delta}$ (Hg-12R12) was synthesized in 1991[68], with R = rare earth element. However, with a structure similar to the thallium-containing superconductor $TlBa_2CaCu_2O_7$ (Tl-1212), which has one TlO layer and two CuO_2 layers per unit cell, and a T_c of 85 K [69]. But in spite of its resemblance to Tl-1212, Hg-12R12 was initially found not to be superconducting. It was suggested that the hole concentration in these phases was not high enough for inducing superconductivity and that this could be achieved by replacing the trivalent rare-earth cations (R^{3+}) by divalent ones such as Ca^{2+} [68]. The continued research by Putilin et al. [49] resulted in the synthesis of the first superconducting mercury cuprate, $HgBa_2CuO_{4+\delta}$ (Hg-1201) with T_c up to 94 K, at the end of 1992.

Figure 2.1: *Structural models for the series* $HgBa_2Ca_{n-1}Cu_nO_{2n+2+\delta}$*(*$n$*= 1, 2, 3 and 4). Black spheres correspond to oxygen atoms. Little spheres at top and bottom correspond to partially occupied oxygen positions.*

The $HgBa_2Ca_{n-1}Cu_nO_{2n+2+\delta}$ polytype phases exhibit a layered structure and consist of HgO_δ, 2BaO, (n-1)Ca and $n$$CuO_2$ layers. The rock-salt block has the same structure for all members and consists of three alternating layers (BaO)(HgO_δ) (BaO). The perovskite block contains conducting (CuO_2) layers and the thickness of this block may vary by insertion of (Ca)(CuO_2) fragments resulting in a formation of the sequence of layers, alternating along the c-axis of the unit cell:

$$(HgO_\delta)(BaO)(CuO_2)\{(Ca)(CuO_2)\}_{n-1}(BaO)(HgO_\delta).$$

Figure 2.1 is a schematic drawing of the atom arrangement in the unit cells of four members of the Hg-12[n-1]n family. While values of n =1 to 6 are possible, only four compounds are considered, for which the layer structure becomes clearly visible. Short notations Hg-1201, Hg-1212, Hg-1223, and Hg-1234 have been used. These compounds are also refereed as one-, two-, three-, and four-layered systems. All phases crystallize in primitive tetragonal unit cells with the space group $P4/mmm$, the lattice parameter is $a \sim 3.85$ Å for all of them, and a variable c-axis parameter depending on the thickness of the perovskite block (n)

Table 2.1: Experimental data for the Hg-1201, Hg-1212, Hg1223, and Hg-1234 systems under ambient pressure. Given are the unit cell volume V, the lattice constants a and c together with their ratio, and a reference to the corresponding experiment.

Compound	$V[a.u.^3]$	$a[a.u.]$	$c[a.u.]$	c/a	Ref.
Hg-1201	967.7	7.332	18.000	2.455	[70]
Hg-1212	1278.7	7.300	23.995	3.287	[71]
Hg-1223	1578.0	7.278	29.790	4.093	[72]
Hg-1234	1901.1	7.278	35.890	4.931	[72]

in accordance with the formula: c (Å)= [3.2 (n-1) + 9.5]. Experimental values for the lattice constants a and c can be found in Table 2.1. The symbol δ represents a small excess of oxygen located in the center of the top and bottom layers, at positions ($\frac{1}{2}\frac{1}{2}0$) and ($\frac{1}{2}\frac{1}{2}1$). If this oxygen were included the level symbol would be [Hg-O] instead of [Hg–]. The ideal structure of (CuO_2) layers in the Hg-based superconductors allows one to reach optimal conditions for the overlap of Cu 3d and O 2p orbitals. We can see the relationship between the layering schemes of aligned Hg-based superconducting compounds (Fig. 2.2) and those of the other cuprates. For example, we see that the $n = 1$ compound $HgBa_2CaCu_2O_{6+\delta}$ is quite similar in structure to $YBa_2Cu_3O_{7-\delta}$ with Ca replacing Y in the center and Hg replacing the chains [CuO -]. The similarity between the arrangement of the atoms in the unit cell of each $HgBa_2Ca_{n-1}Cu_nO_{2n+2}$ compounds and the arrangement of the atoms in the semi-unit of the corresponding $Tl_2Ba_2Ca_{n-1}Cu_nO_{2n+4}$ compounds is strong. Their structure is the same except for the replacement of the [Tl-O] layer by [Hg–]. The superconducting properties of the homologues in the same family differ, and T_c changes non-linearly with the number of layers. T_c of $HgBa_2Ca_{n-1}Cu_nO_{2n+2+\delta}$ phases strongly depend on parameters such as doping, oxygen content (δ), pressure, and number (n) of (CuO_2) layers in their structures. The role of the interstitial oxygen site in the HgO_δ plane is fundamental in controlling the electronic properties of these materials. Controlling the occupancy (δ) of this interstitial oxygen site allows one to chemically tunethe electronic properties of the mercury cuprates from insulating, through

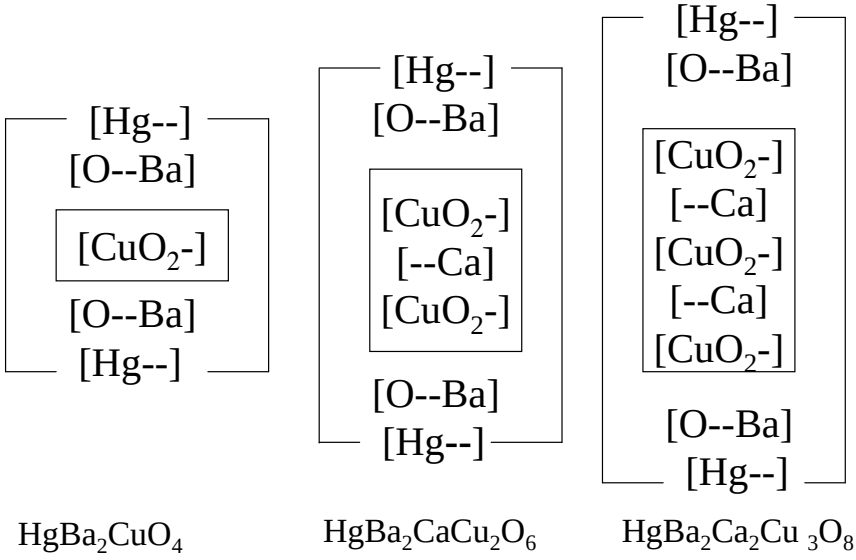

Figure 2.2: *Layering schemes of three $HgBa_2Ca_{n-1}Cu_nO_{2n+2}$ compounds. The CuO_2 planes layers are enclosed in small inner boxes, and the layers that make up a formula unit are enclosed in larger boxes.*

superconducting, to metallic behavior. However, δ is rather small, i.e., $\delta < 0.4$, as a result of the linear oxygen coordination of Hg^{2+} in the compound [73]. For a phase with a given number of CuO_2 layers n, the maximal critical temperature T_c (and correspondingly the maximum superconducting gap Δ_s) can be achieved by the variation of the excess oxygen concentration (δ) in the spacers [74, 75]. The excess oxygen attracts electrons from the CuO_2 layers without introducing a significant scattering of charge carriers in the superconducting blocks (distant doping). In addition the excess oxygen forms traps in the spacers, thus strongly influencing the transport in c-direction due to resonant tunnelling effects [76, 77]. Samples with the maximum critical temperature T_c corresponding to the excess oxygen concentration $\delta = \delta_{opt}$ are defined as optimally doped. For the optimally doped HTSC samples the dependence of the critical temperature T_c on the number of CuO_2 layers n is strongly nonlinear [78]. In particular, an increase of the transition temperature with increasing n has been verified within the different cuprate families, such as the Bi-, Tl-, or Hg-based compounds. Although it seemed tempting to add more and more such CuO_2 layers to the crystal structure, there is a limit in that for $n > 3$ the superconducting properties become worse,

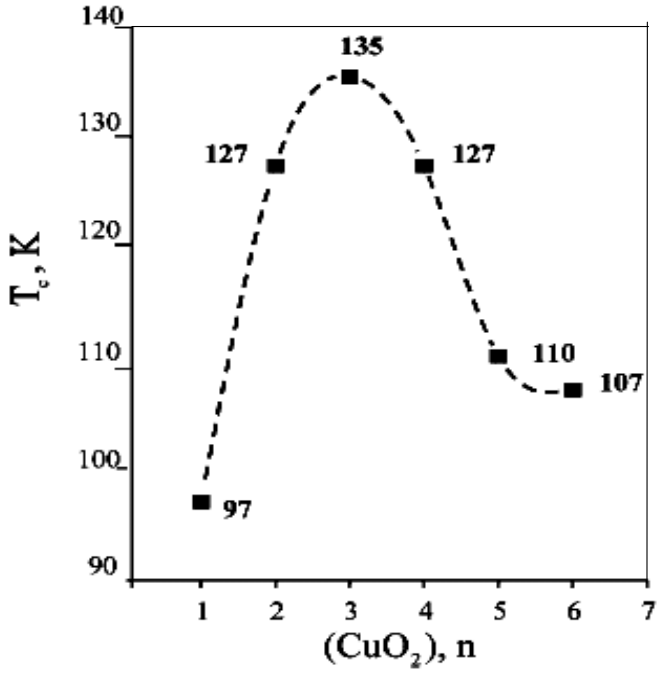

Figure 2.3: *T_c plotted as a function of the number of superconducting layers in the unit cell for the Hg-based family.*

i.e., T_c decreases again. Figure 2.3 shows the dependence of T_c versus n. T_c values correspond to the highest detected transition temperature for each phase. The transition temperature sequentially increases from the first member (97 K) of the homologous series through the second (127 K) to the third one (135 K), and then gradually goes down for the fourth (127 K), fifth (110 K) and sixth (107 K): the result is a bell-shaped curve. The obtained dependence of T_c versus the number of layers is similar to that found for Bi- and Tl-containing phases. Several theoretical models have been proposed to explain the nontrivial dependencies $T_c(n)$ in HTSC materials [52, 78, 79, 80, 81, 82, 83]. Unfortunately, this phenomenon remains unsolved and is still poorly understood, mainly because of the limited and often conflicting experimental data on the variation of superconducting properties of HTSC with the number of CuO_2 planes in the superconducting blocks [84], and attention has instead been mainly focused on the properties of a single CuO_2 plane. Very recently, S. Chakravarty et al. showed that the quantum tunnelling of Cooper pairs between the layers [85] simply and naturally explains the exper-

Figure 2.4: *Crystal structure of the second member of Hg-family, $HgBa_2CaCu_2O_{6+\delta}$ (Hg-1212), containing charge reservoirs (CR), superconducting layers (SC), and both large (major) and small (minor) alkaline-earth (AE) metal sites. This structure is also illustrated by a layer-by-layer drawing.*

imental results, when combined with the recently quantified charge imbalance of the layers [86] and the latest notion of a competing order [87, 88, 89, 90, 91, 92] nucleated by this charge imbalance that suppresses superconductivity. They calculated the bell-shaped curve and showed that, if materials can be engineered so as to minimize the charge imbalance as n increases, T_c can be raised further.
Figure 2.4 is the schematic structure of the second member of the $HgBa_2Ca_{n-1}Cu_n O_{2n+2+\delta}$ series, which has two CuO_2 layers per unit cell. It displays a tetragonal structure with the space group $P4/mmm$, where the c-axis is perpendicular to the CuO_2 planes. These planes are the main building block of all these compounds and are responsible for the superconducting properties. The lattice parameters are $a = 3.862$ Å and $c = 12.707$ Å [27]. In Fig. 2.4 all structural constituents are displayed and marked. The lattice parameters of $HgBa_2CaCu_2O_{6+\delta}$ are close to those of the rare-earth Hg-1212 compounds [68], but the a parameter of the superconducting phase is smaller. Such a decrease of the a parameter, which depends on the lengths of the in-layer Cu-O bonds, occurs because the hole concentra-

tion in the copper valence increases. The $HgBa_2CaCu_2O_{6+\delta}$ compound consists of double pyramidal copper layers interconnected by HgO_δ sticks and separated by Ca and by Ba atoms that are located above and below the pyramidal copper layers [49]. Its structures are composed of single mercury oxide layers in rock salt like blocks (BaO-HgO_δ-BaO) and perovskite type blocks of variable extent —CuO_2-Ca-CuO_2-Ca-CuO_2— [93]. The Cu cations are pyramidally coordinated, they are sited with oxygen atoms at the centers of the base, while the coordination of the other cations depends upon the value of oxygen content (δ). The Ca cations are surrounded by 8 oxygen atoms arranged in a tetragonal surrounding. The unique crystal chemistry of Hg^{2+} cations determines the structural properties of the Hg-based superconductors. The characteristic feature of this cation is a stable dumbbell coordination, which implies a formation of two strong covalent HgO bonds with the oxygen atoms from two neighboring (BaO) layers and only a weak interaction with oxygen atoms located in the (HgO_δ) layer at the middle of the Hg square mesh.

2.3 Phase relations in the Hg-Ba-Ca-Cu-O system

The synthesis of mercury-based high T_c superconductors in the form of pure, single phase samples is difficult due to high volatility of mercury, i.e., their very low stability at elevated temperatures where the phase formation occurs. Samples are obtained either in sealed quartz ampoules or under high external pressure. The high toxicity of Hg, mercury oxide decomposition to mercury and oxygen at a relatively low temperature, and the high vapor pressure of Hg force to prepare the material under confined vessels avoiding the loss of Hg vapors. For the synthesis in the ampoules, the important factor that influences the phase composition of the reaction product is the presence of a considerable amount of mercury in the gaseous phase. In order to avoid the mercury losses, the reaction must be carried out in sealed ampoules under a simultaneous control of mercury and oxygen partial pressure [94]. However, controlled conditions are difficult to achieve and the experiments tend to be highly irreproducible because of the variable partial pressures of mercury and oxygen (P_{Hg}, P_{O_2}) as well as total pressure being

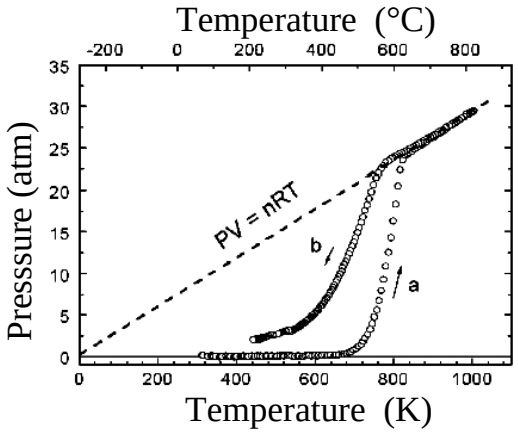

Figure 2.5: *Pressure against temperature diagram of the HgO decomposition (purity > 99%). The pressure was measured by means of a thermobaric analyzer or TBA [96].*

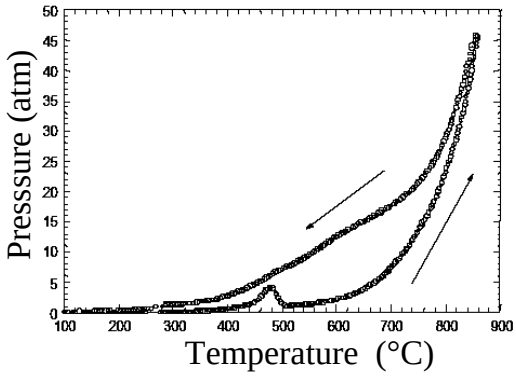

Figure 2.6: *Pressure versus temperature diagram of the synthesis of Hg, Re-1223 inside a quartz capsule during a temperature cycle (measured by TBA) [96].*

dependent on ampoule dimensions and applied temperature regime [95]. From the thermodynamic point of view the system Hg-Ba-Ca-Cu-O shares two components, mercury and oxygen, with the surrounding atmosphere. Consequently, their content in the condensed phase, as well as the respective phase equilibria can be controlled only by adjusting their activity, i.e., the composition of the surroundings. Indeed, some attempts have been made to control P_{O_2} by keeping an oxide redox couple (like Cu_2O/CuO, Mn_2O_3/Mn_3O_4, CoO/Co_3O_4) at given temperature in the same ampoule. The activity of mercury could be adjusted in a similar way, but it is obviously more difficult to find out the appropriate pair of Hg-compounds. The measurement of the pressure variation inside a sealed quartz tube due the gases involved in a solid-gas reaction is very important in learning about the details of a synthesis. Such measurements, during synthesis at high temperatures, are considered to be quite a difficult problem. Various indirect pressure measurement methods have been reported. A. Sin et al. studied the decomposition of HgO and the processing of Re-doped Hg-1223. They have developed a thermobaric analyzer (TBA) [96] which allows to measure in-situ the total internal gas pressure of the reaction chamber during the syntheses at high temperatures, hence opening the door to a real time control of thermodynamic

parameters and reaction kinetics. The concept of the TBA set-up is verified with HgO decomposition. The HgO decomposition was performed with a heating rate of 120 °C /h, keeping the sample for 1 h at the maximum temperature of 830 °C and then cooling down to room temperature with a rate of 120 °C/h. The results show the physical and chemical processes that occur inside the quartz ampoule. First, during the heating ramp (see Fig. 2.5 a), the beginning of the decomposition of HgO can be observed at about 500 °C. Then, when the HgO is completely decomposed at about 650 °C, the gas pressure follows the ideal gas law. In the cooling ramp (see Fig. 2.5 b), the total pressure follows a different path to that of the heating ramp. This is expected since the kinetics of a gas-solid reaction is slower than the corresponding solid-gas reaction because an Arrhenius-type law controls the recombination reaction of the gases in the cooling process. To illustrate the application of this device they described the synthesis of the ceramic superconductor (Hg,Re)-1223, which was performed inside sealed quartz tubes, using the TBA sensor in order to follow the pressure variation during the heating or cooling processes. Typical records of the measured P-T curves during the synthesis of a (Hg,Re)-1223 compound are displayed in Fig. 2.6, where the arrows indicate the direction of the thermal treatment (heating and cooling processes). The pressure is very low from room temperature up to 350 °C when it begins to increase markedly. At 470 °C the pressure increases to ≈ 5 bar. When the temperature reaches 650 °C the pressure increases more rapidly up to about 46 bar at 850 °C. During cooling the pressure reveals higher values than during heating. Another detail is related to the pressure kink that appears at intermediate temperatures around 470 °C, which depends on the oxygen content of the sample, and is controlled by a previous treatment of the precursor materials under an oxygen partial pressure at 930 °C. A detailed study on this is given by A. Sin et al. [96]. The oxygen excess at the precursor stage makes the kink pressure move to high temperatures and increase in intensity; this phenomenon results in a decrease of the kinetics of the formation of the superconductor, favouring $HgCaO_2$ formation.

The knowledge of all these parameters has allowed to optimize the processing and the superconducting characteristics of these materials. This has led to a widespread interest in the physical properties of the homologous Hg-based series which now may be prepared in a pure form.

2.4 $(Hg_{0.9}Re_{0.1})Ba_2CaCu_2O_{6+\delta}$ (HgRe-1212) thin films

In order to study the intrinsic physical properties and to develop superconducting electronic devices of the mercury family, many efforts have been devoted to the synthesis of high quality Hg-based cuprate thin films. Several groups have successfully prepared $HgBa_2CaCu_2O_{6+\delta}$ (Hg-1212) thin films [97, 98, 99, 100, 101, 102]. Some of them used the method of utilizing an excessive amount of Hg in the vacuum deposition system. However, the predominant method for preparing mercury-based high-T_c superconducting films is post-annealing precursor films in mercury atmosphere [103]. It is also reported that Ba-Ca-Cu-O precursors are very sensitive to moisture and CO_2 in air [104, 105]. Stabilization of the Ba-Ca-Cu-O precursors in air is possible by adding a small amount of rhenium [106, 107, 108]. In this work we report the growth of high quality $(Hg_{0.9}Re_{0.1})Ba_2CaCu_2O_y$ superconducting thin films.

Chapter 3

Methods and procedures

First of all and in order to minimize unhealthy effects from exposure to mercury, we have to know that mercury has been identified as a chemically hazardous compound for many years. Mercury (Hg) and mercury compounds, when ingested, inhaled, or absorbed by the skin, are highly toxic and can affect major organs as well as the central nervous system. In the environment, mercury is present in air, water, soil/sediments, plants, and animals; however, sediments are the primary sink for this metal. The aim of the present chapter is to find optimum conditions for the mercury superconductors preparation in the form of thin films. In the following chapter, we report the growth of high quality $(Hg_{0.9}Re_{0.1})Ba_2CaCu_2O_{6+\delta}$ superconducting thin films using the stable Re-doped $Ba_2CaCu_2O_y$ (Re-212) precursor by pulsed laser deposition (PLD) and post-annealing methods. All steps have been carried out under ordinary laboratory conditions without using special atmosphere during the preparation. Rhenium stabilized $Re_xBa_2Ca_{n-1}Cu_nO_y$ ($n = 2$) precursor thin films were deposited on (100) c-axis oriented and vicinal $SrTiO_3$ substrates by pulsed laser deposition, where the resulting material of $Re_{0.1}Ba_2CaCu_2O_{6+\delta}$ served as target for pulsed laser deposition onto (100) aligned $SrTiO_3$ substrates. After Hg-vapor annealing methods the films show sharp superconducting transitions at $T_c = 124$ K with $\Delta T_c \approx 2$ K. We have chosen $SrTiO_3$ because this substrate has a smaller lattice constant and the lattice mismatch is smaller (1.3 %) than for MgO (9.3 %) which seems to be more favorable for film growth. The growth of the mercury films on STO substrates is coherent, i.e., the in-plane lattice matches with that of the substrate.

3.1 Preparation of Hg,Re-containing HTSC thin films

The mercury cuprates $HgBa_2Ca_{n-1}Cu_nO_{2n+2+\delta}$ (Hg-12$(n-1)n$) have an exceptional position among the high-temperature superconductors due to their elevated critical temperatures. Nevertheless, their preparation is not fully understood. There are at least two factors that make the synthesis unusually difficult:

- The sensibility of barium containing precursors to humidity and carbon dioxide, which necessitates careful preparation and handling under on inert atmosphere.

- The volatility of mercury oxide, requiring the use of a closed system for the synthesis, e.g. sealed silica tubes.

During the course of search for a simple and safe route for the synthesis of high quality Hg-12$(n-1)n$ samples, it was found that [51, 97, 98, 99, 100, 101, 102, 109]

1. the undoped Hg-12$(n-1)n$ can only be synthesized at ambient pressure from a fresh precursor which has had minimum exposure to the surrounding air environment,

2. there is a competition between the formation of the impurity phase $CaHgO_2$ and superconducting phase Hg-12$(n-1)n$ at the synthesis temperature during the process,

3. traces of moisture and/or carbon dioxide significantly affect the formation of the impurity phase $CaHgO_2$,

4. the impurity phase $CaHgO_2$ has a bad effect on the synthesis and the superconductivity of the Hg-12$(n-1)n$ superconductor,

5. the formation of the superconducting compound Hg-12$(n-1)n$ depends critically on the precursor used and the synthesis conditions such as the Hg-vapour pressure and the partial vapour, the reaction temperature, the reaction time, and the reaction atmosphere, etc., and

6. the Hg-12$(n-1)n$ is only marginally stable at a temperature lower than the formation temperature.

The successful process consists of several steps, because the precursor material requires a larger annealing temperature ($\sim$ 800 °C) and longer time due to complicated diffusion paths. Synthesis of higher (n = 2, 3) members of the series Hg-12$(n-1)n$ occurs through the formation of the lower (n-1) member at the initial step of the reaction, and this process also requires a longer annealing time [110].
Several synthetic techniques have been proposed in order to obtain high-purity phases. There are

(i) the precursor method in which samples are prepared from a mixture of HgO and Ba-Ca-Cu-O precursor [111, 112]. Although it is relatively easy to obtain the phases using this technique, impurity phases (ex. $CaHgO_2$) are often detected [112].

(ii) the single-step firing method starting from a mixture of monoxides (HgO, BaO, CaO, and CuO) [113, 114, 115]. Using this technique, nearly single-phase samples were obtained when the sintering temperature and the time were optimized.

(iii) the two-pellet technique in which a Hg-Ba-Ca-Cu-O pellet and a Ba-Ca-Cu-O pellet are placed in a quartz tube [109, 116]. Also as in the second technique, nearly single-phase samples were obtained when the sintering temperature and the time were optimized.

(iv) the high pressure synthesis technique [32, 117] is an effective method to suppress the Hg volatilization.

In all these cases, the final products are strongly influenced by the starting materials (chemical species, homogeneity, purity, particle size, and others) and the sintering conditions (total sample weight, tube volume, heating process, and others). Although the phase diagrams between the partial pressure of oxygen or mercury and temperature for $HgBa_2CuO_y$ [94] and $HgBa_2CaCu_2O_y$ [118] have been reported, the phase formation and phase stability of Hg-12$(n-1)n$ are still not understood due to the complex reaction process.
In the present chapter of this work, the details of the optimization of synthetic and reproducibility conditions for high-quality samples are described, and the growth of high quality superconducting Hg,Re-containing thin films by pulsed

laser deposition (PLD) and post-annealing methods using the stable Re-doped $Ba_2CaCu_2O_y$ (Re-212) precursor are reported. The mass of the starting mixture and its oxygen stoichiometry, ampoule free volume, temperature and time of synthesis, cooling conditions have been varied to optimize the preparation of these films. All steps have been carried out under ordinary laboratory conditions without using special atmosphere during the preparation. Our study demonstrates that maintaining the phase equilibrium during the Hg-vapor annealing is important for the preparation of high-quality thin films.
The preparation of $(Hg_{0.9}Re_{0.1})Ba_2CaCu_2O_{6+\delta}$ thin films involves three main steps,

(1) the preparation of the precursor target,

(2) the ablation of the precursor by pulsed laser deposition on (100) oriented $SrTiO_3$ substrates, and

(3) the formation of $(Hg_{0.9}Re_{0.1})Ba_2CaCu_2O_{6+\delta}$ by gas/solid diffusion.

3.2 Preparation of the precursor thin films

Due to the high transition temperature, the preparation of the $Hg_{0.9}Re_{0.1}Ba_2Ca_{n-1}Cu_nO_{2n+2+\delta}$ thin films was set as the goal of the thesis and the composition of targets and precursor powders was coordinated with it. A characterisation of the films showed that in the structure and in the superconducting characteristics of the samples the $HgBa_2CaCu_2O_y$ phase dominates. After the preparation of a target from $Re_{0.1}Ba_2Ca_{n-1}Cu_nO_{2n+2+\delta}$, one could proceed with the deposition of mercury-free precursor films. This is the first step of the preparation. However the second reaction step, sintering the precursor films with mercury oxide and/or a mixture from mercury oxide and precursor powder in the evacuated quartz glass ampoule, is most important.

3.2.1 Rhenium substitution

Given the advantages of superconducting properties, Hg-based superconductors have potential for high temperature and high magnetic field applications. Unfortunately, because of the absence of a trivalent element in these compounds,

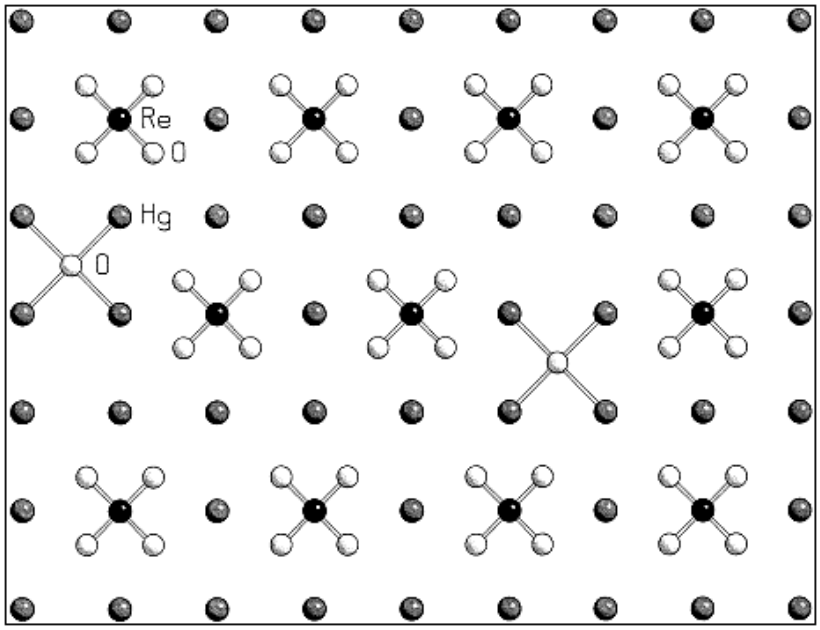

Figure 3.1: *Model of the (Hg,Re)O layer in a* $Hg_{1-x}Re_xBa_2Ca_{n-1}Cu_nO_{2n+2+\delta}$ *single crystal [123].*

an excess of oxygen vacancies will be present, which is likely to make the Hg-based cuprates metastable, and hence inherently difficult to synthesize. It was found that partial substitution of mercury by higher-valence cations, such as Bi, Pb, and transition elements as Re, significantly improves the formation and enhances the stability of the superconducting phases without affecting the T_c [119, 120, 121, 122]. In this thesis most attention was paid to the Re dopant, since Re is most commonly used to improve the $HgBa_2Ca_{n-1}Cu_nO_{2n+2+\delta}$ phase stability and flux pinning. Structural analysis has shown that Re is introduced at the Hg site and coordinated octahedrally by oxygen atoms [123], Figure 3.1. The Re substitution has brought great benefits for the synthesis and stability of $Hg_{1-x}Re_xBa_2Ca_{n-1}Cu_nO_{2n+2+\delta}$ phases. Specifically, Re doping

* reduces the sensitivity of precursors and superconducting phases against CO_2 to levels allowing less complicated preparation and handling [124], and

* promotes the formation and grain growth of Hg-12(n-1)n phases [125],

∗ with octahedrally fully coordinated oxygen atoms, gives rise to the stabilization of the Hg(Re)O layer, thus stabilizing the Hg-12(n-1)n phases [126].

3.2.2 Preparation of a target

The raw materials of the $Re_{0.1}Ba_2Ca_{n-1}Cu_nO_{2n+2+\delta}$ targets were the carbonates $BaCO_3$ and $CaCO_3$ as well as the oxides CuO and ReO_2 with their mole masses M. The small addition of ReO_2 served to stabilize the precursor compound in air. In the case of a target mass m_T (typically 10 g), one has for the weighed raw materials:

$$m(ReO_2) = 0.1\frac{M(ReO_2)}{M(Re_{0.1}Ba_2Ca_{n-1}Cu_nO_{2n+2+\delta})}\, m_T$$
$$m(BaCO_3) = 2\frac{M(BaCO_3)}{M(Re_{0.1}Ba_2Ca_{n-1}Cu_nO_{2n+2+\delta})}\, m_T$$
$$m(CaCO_3) = (n-1)\frac{M(CaCO_3)}{M(Re_{0.1}Ba_2Ca_{n-1}Cu_nO_{2n+2+\delta})}\, m_T$$
$$m(CuO) = n\frac{M(CuO)}{M(Re_{0.1}Ba_2Ca_{n-1}Cu_nO_{2n+2+\delta})}\, m_T$$

Here only the desired stoichiometry of the metals involved was considered. The correct oxygen content adjusted itself during late sintering according to the oxygen partial pressure. The starting powders were mixed and reground thoroughly. The grey-green mixture developing thereby was put in a covered alumina oxide crucible into the furnace. It was heated up several times for some hours in air, and regrounded between each heating and after the last heating. With escaping of CO_2 the desired black metallic oxide formed. A white coating was an indication of incomplete reaction. Subsequently, the target for the pulsed laser deposition was pressed. The inside diameter of the pressing cylinder was 23 mm, so that it fitted well into the target mounting plate. Before the installation into the PLD chamber the target had to be heated up again for hardening. One generally selected heating/cooling rate of 5 °C per minute, whereby the inside of the furnace cooled down due to its good isolation substantially more slowly on room temperature and one had not to fear cracking of the target.

In the present section, the preparation of the precursor targets and the precursor powders, which were needed for the mercury-oxide precursor mixture, is

described.

3.2.3 Preparation of the stable Re-212 doped precursor thin films

During the experimental work, precursor targets with the different sets of starting materials have been prepared to grow the Hg-HTS thin films on (100) single crystals $SrTiO_3$ substrates with PLD. Four different compositions have been used:

(A) ReO_2 (Alfa Aesar-company providing raw material , 99.9%), $BaCO_3$ (Alfa, 99.997%), CaO (Alfa, 99.95%), CuO (Cerac, 99.999%), and oxygen from air surrounding. The precursor target used for pulsed laser deposition was prepared by solid state reaction. The precursor material with the nominal composition $Re_{0.1}Ba_2CaCu_2O_{6+\delta}$ was prepared from a well ground stoichiometric mixture of ReO_2, $BaCO_3$ and CuO (by calcination at 870-915 °C for 72 h to minimize possible water vapor and/or carbonate contaminants), the materials were mixed and were carefully ground for half an hour in a ceramic mortar and heated in an open furnace. Three intermediate grinding processes were carried out to ensure the homogeneity of the composition. The calcinated mixtures were reground and compressed into 23 x 5 mm^2 disc shape using a force of 50 kN. The target for ablation was obtained by sintering the compacted disc in air at a rate of 5 °C/min to 915 °C and was maintained at this temperature for 72 h, then slowly cooled at a rate of 5 °C/min to room temperature. The slow cooling and heating were crucial to avoid the target failure. The typical XRD for the film prepared by using this target is shown in Fig. 4.7. The films show the presence of impurity phases.

(B) ReO_2 (Alfa, 99.9%), $BaCO_3$ (Alfa, 99.997%), CaO (Alfa, 99.95%), CuO (Cerac, 99.999%), and pure oxygen. The precursor target used for pulsed laser deposition was prepared under the same conditions with that of the first target but in flowing oxygen gas O_2. For the final heat treatment the precursor target was heated to between 900 °C and 950 °C for about 72 h. The higher temperature is better, but be sure of the accuracy of the temperature indicator before getting too close to 1000 °C. Temperatures above

1000 °C risk decomposition of the crystal structure and the possibility of the material sticking to the alumina crucible. From these targets we have prepared $(Hg_{0.9}Re_{0.1})Ba_2CaCu_2O_{6+\delta}$ (HgRe-1212) thin films with sharp superconducting transitions at T_c= 120 K with the transition width $\Delta T_c = 3$ K. The typical XRD for the film prepared by using this target confirmed the presence of texture as is illustrated in Fig. 4.8.

(C) ReO_2 (Alfa, 99.9%), commercially available multiphase $Ba_2CaCu_2O_x$ (Alfa, 99.9%), and pure oxygen. The precursor material with the nominal composition $Re_{0.1}Ba_2CaCu_2O_y$ was prepared from a well ground stoichiometric mixture of ReO_2 and commercially available multiphase $Ba_2CaCu_2O_x$, the materials were mixed and ground for half an hour in a ceramic mortar. $Ba_2CaCu_2O_x$ was used in order to avoid carbonate decomposition during the heat treatment. The mixed powder was pressed into pellets and sintered in an Al_2O_3 crucible at 880 °C for 48-72 h in an O_2 atmosphere to eliminate moisture and carbonates. The thickness of the pellets were $\approx$ 2 mm using a force of 10 kN. After sintering the precursor powder revealed dark grey color and usually was hard to remove from the crucible. These calcinated mixtures were reground, pressed into a $\phi 25 \times 5\,\mathrm{mm}^2$ disc using a force of 50 kN, and sintered at 880 °C for 72 h in an O_2 atmosphere. Three intermediate grinding processes were carried out to ensure the homogeneity of the composition. It is absolutely necessary that the cool-down take place very slowly and under adequate oxygen flow. The rate of cooling must not be more than 100 °C per hour. Take special care to insure that the the precursor material has access to plenty of oxygen, especially during the cool-down from 880 °C to 300 °C. Continuous oxygen flow must be maintained. If the atmosphere in the furnace is not oxygen-rich while the precursor material is still above about 400 °C, the material can lose vital oxygen from its crystal structure. After the furnace temperature reaches about 500 °C, the cooling rate can be increased. To avoid cracking of the disc the heat treatment was carried out with slow temperature variations. Heating the disc up to 920 °C in an O_2 atmosphere at a rate of 5 °C/min, holding this temperature for 72 h, then decreasing to room temperature at the same rate. The resulting material served as a target for pulsed laser deposition onto (100) aligned $SrTiO_3$ substrates. Immediately after cooling

the precursor target and precursor material were stored in the desiccator to avoid detrimental effects of moisture and CO_2. By using this target, fully textured $(Hg_{0.9}Re_{0.1})Ba_2CaCu_2O_{6+\delta}$ (HgRe-1212) thin films have been prepared, as is shown in Fig. 4.9.

(D) To grow high purity Hg-thin films without Re, the precursor target and precursor powder with the nominal composition $Ba_2CaCu_2O_y$ were prepared, rather than Re-212 target and powder. $Ba_2CaCu_2O_y$ target and powder were also prepared at the same sintering schedule and sintering condition with that of the third process. By using this target and powder, $HgBa_2CaCu_2O_{6+\delta}$ thin films with a sharp onset near 120 K are successfully synthesized. During the experimental work, a comparison of samples synthesized under identical conditions with and without Re showed similar phase purity. However, the films without Re were unstable and decomposed in the air within a few days, as is shown in Fig. 4.2. If the precursor target or the precursor material were used after one month from the preparation the critical temperature for the final films was not in the range of the Hg-films. Therefore precursor material and target should be sintered again with the given parameter before usage.

3.3 Ablation of the precursor films

3.3.1 Laser ablation chamber used in the experiments

Pulsed laser ablation for the deposition of thin films is a technology that has been explored in some detail [127]. High-temperature superconductor Hg,Re-containing thin films have been prepared by PLD which is a unique process providing stoichiometric transfer of target materials [128]. This process has a number of advantages relative to conventional deposition technologies [129, 130, 131]. In contrast to most other deposition processes, the energy at the target can be controlled independently of the process pressure and gas mixture. Reactive processes can easily be conducted. Pulsed laser deposition (PLD) has been used for the production of dielectric, ferroelectric, and piezoelectric films, semiconductor layers, superlattices, and most for the production of high-temperature superconducting (HTSC) thin films. Since PLD can take place under controlled oxygen atmo-

sphere, it is especially suited for the growth of thin-film high-T_c superconductors (HTSCs), whose properties are highly sensitive to their oxygen content. Another benefit of PLD is that it produces a highly forward-directed and confined plume of materials, which can be deposited with less contamination than other thin film processes, such as sol-gel, metal organic chemical vapor deposition (MOCVD), etc. Today, PLD is one of the fastest growing thin-film processes in multicomponent films.

The principal components of our laser-ablation system are a vacuum chamber and an excimer laser for producing high-power pulses. An overview of the complete system is illustrated in Fig. 3.2. The laser pulses are produced by a Lambda Physik LPX 300 excimer laser (EL). The most important parameters of the laser are:

* wavelength l = 248 nm
* maximum pulse energy $E_{max} \approx 1.2$ J
* pulse duration t = 25 ns
* repetition rate 10 Hz

In laser ablation, high-power laser pulses are used to ëvaporatematter from a target surface such that the stoichiometry of the material is preserved in the interaction. The photons of the laser beam interact with the electrons of the target material. The subsequent electron-phonon interaction leads to a sudden increase of the local temperature, surface or subsurface vaporization (depending on energy of the laser beam) and an explosive removal of material. As a result, a supersonic jet of atoms and particles (plume) is ejected to the target surface. The plume expands from the target with a strong forward-directed velocity distribution of the different particles. The ablated species condense on the substrate placed opposite to the target. The ablation process takes place in a vacuum chamber - either in vacuum or in the presence of some background gas. In the case of oxide films, oxygen is the most common background gas. The use of oxygen gas compensates for the oxygen deficiency when the oxide ceramics are laser deposited in vacuum. In addition, the plume size, i.e., the plume range L, can be controlled by adjusting the oxygen pressure. A typical plume consists of high-energy electrons, ions, and neutral species that are ejected from the target. The plume shape

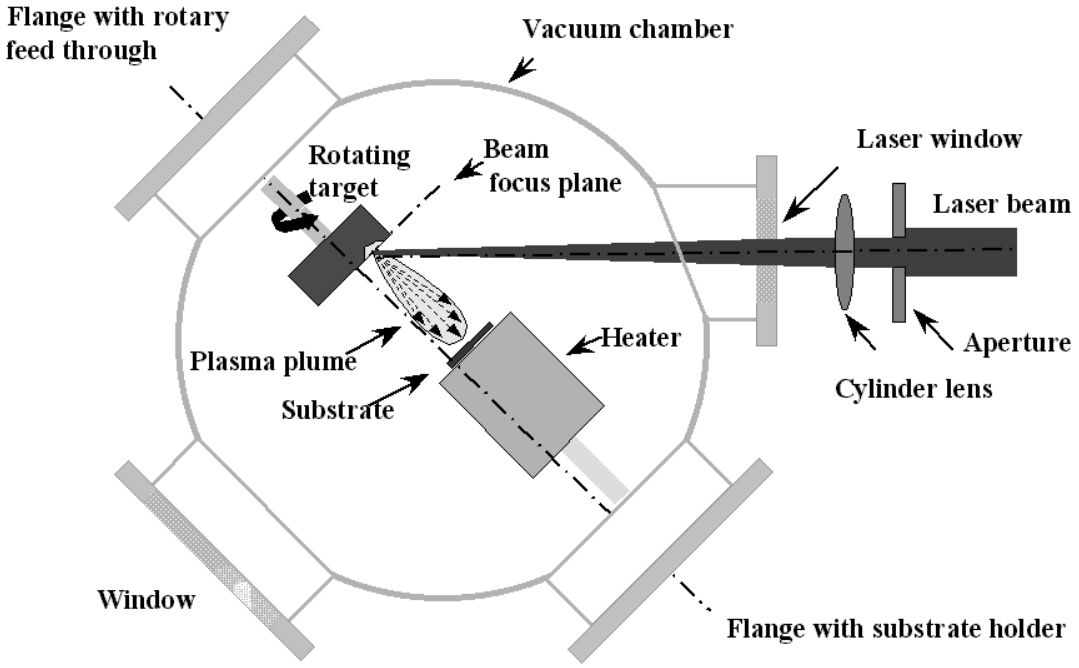

Figure 3.2: *The laser ablation chamber used in our experiments.*

is a scattered cone at lower oxygen pressure. A decreased, confined ellipsoidal plume shape at higher oxygen pressure is formed due to more collision. In the case of $(Hg_{0.9}Re_{0.1})Ba_2CaCu_2O_{6+\delta}$ (HgRe-1212) thin films, the oxygen pressure is $\approx$ 0.3 mbar.

3.3.2 Deposition of the stable Re-doped precursor thin films

Prior to the growth of the film, the growth chamber must be meticulously cleaned with acetone. Individual parts, such as the target and substrate holders, must be degreased with a sequential isopropanol and acetone treatment, which is done by placing them in a clean beaker placed in an ultrasonic cleaner for 10 minutes for each solution.

At the beginning of the film preparation one mounted a STO substrate with silver paste on the substrate mounting plate. After deposition of the first precursor film the silver paste had to be removed from the back-side of the substrate. Silver

paste arrearing on the substrate back-side could react when sintering the sample in the evacuated quartz tube with the film material and lead to undesired results. Therefore subsequent substrates were clamped. The clamping device consists of 1 mm thick high-grade steel disc, whose diameter is 2.7 cm. It is screwed on the original substrate mounting plate of the deposition chamber. On the disc two high-grade steel handles are situated in the distance of 8 mm, under which one can fix the substrate. The size of the disc makes it possible to shift the position of the substrate for some millimeters. This is in particular useful if one slightly varies the point of impact of the laser beam on the target. Unfortunately one could not place the high-grade steel disc into the radiation heater due to its dimensions. The substrate therefore was always in front of the heater, which, however, caused no serious problem, since the deposition of most precursor films was accomplished at room temperature. Only seven substrates were heated during the deposition. In these cases it had to be considered that the substrate temperature T was below the adjusted temperature of the heater due to thermal radiation into the deposition chamber. Therefore, the latter had to be selected accordingly higher. The deposition chamber, shown in Fig. 3.2, was evacuated with a rotary pump. At first, we kept the base pressure of 0.1 mbar using a rotary pump. Afterwards we started the turbo pump. When reaching 1×10^{-5} mbar the turbo pump was switched off. Now one ensured for the fact that oxygen flows through the chamber and produced 0.3 mbar. Since the deposition of most precursor films took place at room temperature, one abandoned the employment of the water cooling of deposition chamber and radiant heating. The target rotation was started, with which the preablation could begin. The target was preablated for 10 minutes each time before the actual deposition to remove the surface layer, remove any excess loose material from the target surface, and to ensure comparable deposition conditions, especially for the deposition rate. During the deposition of the first samples 2000 seconds with 5 Hz per second were preablated. Later the preablation was reduced to 900 or 600 seconds. This increased the life time of the target and had no effects on later film growth. The film area can be increased by scanning the laser spot across the target or the plume across the substrate, or by moving the substrate relative to the plume, or by increasing the target-substrate distance. One accomplished the ablation with 8 Hz. However, one increased the high voltage at the laser up to 5 kV with respect

to the preablation. For the determination of the energy density j, the incident area of the laser beam on the target of 0.2 cm^2, and, in addition, the losses of energy due to screening, lens and suprasil window had to be considered. Later one dismounted the sample and stored it in the desiccator. Without desiccator use, samples showed first a shining surface with a dark-brown coloring. After some hours in air they became green, which indicated a chemical reaction with surrounding air. The fact that the precursor films are amorphous was verified by Röntgen structure investigations. The following sections deal with the second reaction step, which affects the superconducting characteristics of the samples substantially stronger than the listed deposition parameters. The accurate value of substrate temperature or energy density was of less importance, at least as long as their values fell into an interval from 14 to 34 °C and 2.1 to 3.2 J/cm^2, respectively. A dependence of the superconducting characteristics on the thickness of the precursor films, which was arbitrarily increased and reduced, could likewise not be proven. The fact that not all precursor films have been sintered has different reasons: Some were needed for the taking of SEM pictures. Others exhibited strong inhomogeneities in the thickness or a damaged surface and were therefore not used for further preparation.
In an oxygen atmosphere ($\approx$ 0.3 mbar) precursor thin films with an optically smooth surface were obtained after deposition at a pulse frequency of 8 Hz for 1 h at room temperature with a laser flux of 650 mJ/pulse. To avoid moisture and CO_2 contamination, all precursor films and targets were stored in vacuum and transferred only in an evacuated exsiccator directly into a dry box for further processing.

3.4 The sealed quartz tube technique

Various encapsulation techniques have been successfully applied to the synthesis of superconductive copper oxide phases [132, 133], especially in the cases where long-period heat treatments are required and/or the desired product contains volatile element(s), e.g. the Hg-based compounds [49]. In the mechanism of growing Hg-based superconducting phase compounds, Hg-containing compounds such as HgO are highly volatile at temperatures above their melting point of 500 °C. The generation of Hg vapor during the sintering process at 750 °C causes

two problems. Firstly, Hg vapor is extremely toxic. It is highly dangerous to fabricate such superconductors in an open environment without proper safety procedures. Secondly, since the Hg-superconducting phase formation temperature of Hg-based superconductors is around 750 °C, HgO in the specimen being fabricated will be decomposed into oxygen and mercury vapor at 500 °C before reaching the superconducting phase formation temperature.

In order to prevent severe Hg loss during the fabrication process, there are two methods that are commonly employed to fabricate the Hg-based superconductors. They are the high-pressure synthesis and the sealed quartz tube technique. The use of high-pressure synthesis technique can lower the amount of mercury oxide loss. Therefore, scientists sinter the specimen under a high pressure of ≈ 2 GPa. The stability of $HgCaO_2$, which is formed at the first stage of the phase formation reaction, can be reduced. This reduction benefits the formation of Hg-based superconducting compounds because the formation of $HgCaO_2$ inhibits the Hg superconducting phase to grow. On the other hand, in the sealed quartz tube technique, the specimen is sintered inside a closed environment. The Hg vapor and the O_2 gas impose a very high vapor pressure on the closed environment of the quartz tube. The Hg vapor enters the specimen inside the sealed tube at the Hg-superconducting phase formation temperature of 750 °C and has the chance to react with other chemical constituents and form the Hg-superconducting phase. In general, both the high pressure and sealed quartz tube technique can produce Hg superconductors with very high critical temperatures. However, only the sealed quartz tube technique or the encapsulation process is likely to be suitable, simple, and quite useful for the fabrication of Hg-based superconductors. In this work, the films are prepared by using the encapsulation technique. It was difficult to choose a container material, since most metals will react with either O_2(g) (oxidation) or Hg(g) (amalgamation). Moreover, base metals cannot be used, since they lower the chemical potential in the system enough to reduce Cu^{+2} to Cu^{+} or Cu metal. Silica, amorphus SiO_2, was therefore chosen as container material because of its mechanical strength and thermal tolerance of quenching from high temperatures, up to about 1150 °C.

The sealed quartz tube technique for Hg-vapor annealing of thin precursor films together with a Hg-containing source and a Hg-free buffer was used. If the reaction takes place at 600 °C, the reaction time has to be long, and the silica may

then start to crystallise and become brittle enough to break. It is therefore advantageous to increase the temperature up to 850 °C or to 880 °C and shorten the annealing time.
Handling and sealing of the quartz tubes is non-trivial and will be described in the following.
Quartz tubes with an inner diameter of 8 mm and a wall thickness of 1 mm were cut into pieces of 20 cm length. Tube edges were polished and the tubes were cleaned with deionized water as well as with ethanol in an ultrasonic bath. After drying in air the tubes were rinsed with acetone and stored in a dry box at 110 °C. Quartz tubes sealing was done with a hydrogen torch. Oxygen gas flow is increased until the flame reaches a length of about 5 cm and is sharply pointed and of light white color. The center of the quartz tubes was heated in the upper third of the flame and rotated to achieve homogeneous heating. When melting starts the tube pieces were slowly drawn apart to produce one side sealed tube pieces. After sealing the tubes were stored in the dry box until use.

3.4.1 Sintering with mercury oxide

The mercury-free precursor film as well as the reaction powder is placed into a quartz tube, which was sealed on one side before. It has a length of approximately 20 cm. The used glass tubes had an outside diameter of 10 mm and a wall thickness of 1 mm. Compared to tubes with wall thickness 1.5 mm one could work on them easier. Now one reduced the diameter of the quartz tube in a place with the help of the hydrogen torch, which was approximately 8 to 10 cm away from the closed end. Over a rubber hose a rotary pump was connected to the open end. After the evacuation to approximately 1 mbar one heated up the tapered region. The glass coalesced and one received a closed tube, whose length varied between 8 and 10 cm. Now the samples could be pushed into the furnace tube. However, the test equipment had to be protected, in particular the furnace tube to meet for the case of an explosion of the quartz tube. One possibility consisted of putting a one side closed tube from alumina into the furnace and positioning the quartz ampule inside this alumina tube. It was 27 cm long with an outside diameter of 33 mm and a thickness of 3 mm. In this way all films were sintered, with which the reaction powder consisted of pure mercury oxide. The furnace was under an extractor hood, which had to be closed during the entire

sinter process. During tapering and melting the quartz tube, which was filled with mercury oxide, a suitable breathing mask and the eye protector had to be carried. It was from interest to determine the temperature distribution inside the furnace. A further reason for this was that: In the coldest place of the quartz tube mercury oxide condensed and starting from 500 °C also pure mercury condensed. The temperature in this place determines then the mercury gas pressure. This should not become unnecessarily high, in order to avoid a blow-out of the quartz tube. For the calculation of the pressure in the quartz tube the knowledge of the temperature distribution was compellingly necessary. In addition one puts a thermocouple into the alumina tube close to the sample.
When sintering with pure mercury oxide there are in principle two possibilities of controlling the mercury pressure and of avoiding an explosion of the quartz tube:

- It offers itself to use the temperature gradient of the furnace. A 8 cm long tube is positioned with one end, where the temperature amounts to 250 °C. The other end where the sample is placed is exposed to 700 °C. In this case mercury oxide condenses at the colder end. Pure mercury does not arise, since mercury oxide decomposes into its components starting from 500 °C. One can infer the resulting pressure from the vapor pressure diagram of mercury oxide:

  $$250\,^{\circ}\mathrm{C} \Rightarrow P \approx 3 \text{ bar}$$

  With a pressure of 3 bar inside the quartz tube an explosion is very improbable.

- When positioning the quartz tube with a length of 10 cm in the hottest range of the furnace with a temperature of 900 °C, a very small amount of mercury oxide with a few milligram may be used. Above 500 °C mercury oxide decomposes into pure mercury and oxygen in accordance with the reaction equation 3.1

  $$2HgO \longrightarrow 2Hg + O_2 \tag{3.1}$$

  If one assumes the forming of the gas consisting of mercury and oxygen, then the resulting pressure can be determined with the help of the ideal gas law,

  $$PV = nRT. \tag{3.2}$$

The parameters result from the dimensions of the quartz tube and the selected furnace temperature:

$$\begin{aligned} V =& \pi r^2 \ell = \pi (0.4 \text{ cm})^2 10 \text{ cm} \approx 5 \text{ cm}^3 \\ T \approx& 800\,^{\circ}\text{C} = 1073\text{K} \\ R =& 8.3144 \text{ J/(mole K)} \end{aligned}$$

The mole number is attributed to the constant mole mass and the used mass of the mercury oxide:

$$\begin{aligned} m_{HgO} &= n_{HgO} M_{HgO} \\ M_{HgO} &= 216.59\,\text{g}\,\text{mol}^{-1} \\ P = P_{Hg} + P_{O_2} &= \frac{3}{2}\,\frac{RT}{V}\,n = \frac{3}{2}\,\frac{RT}{V}\,\frac{m_{HgO}}{M_{HgO}} \\ \Rightarrow P &\approx 12.3 \times 10^6 \text{J/(g m}^3\text{)}\; m_{HgO} \\ m_{HgO} &= 8\text{mg} \Rightarrow P \approx 1\text{bar} \end{aligned}$$

As one can infer from the estimation, 8 mg mercury oxide lead to a pressure of approximately 1 bar. The quartz tube withstands it without any problem.

With the first few films one proceeded in accordance with the first possibility without good success. The formation of $(Hg_{0.9}Re_{0.1})Ba_2CaCu_2O_{6+\delta}$ thin films could not be obtained by direct reaction of the thin film precursor with HgO vapor in a sealed quartz tube due to the difficulty in controlling the Hg vapor pressure. The remaining samples were proceeded as described under the second possibility. The shining surface became mat during sintering. In addition, with a sintering time of 70 hours their color of dark-brown changed to grey. All samples, which were sintered with pure mercury oxide, were insulating, therefore there was no hope for superconductivity. Because of this, one used another procedure, which had already proven successful in the production of mercury superconductors [103]. About this procedure other things are reported: The precursor films were sintered from a mixture made of mercury oxide and precursor powder. The reaction powder corresponded to the material, which one wanted to produce as a film in its exact composition: $Hg_{0.9}Re_{0.1}Ba_2CaCu_2O_{6+\delta}$.

3.4.2 Formation of $(Hg_{0.9}Re_{0.1})Ba_2CaCu_2O_{6+\delta}$ thin films by sintering with mercury oxide precursor mixture (gas/solid diffusion)

Many synthesis procedures have been reported for mercury-based copper oxide superconductors, with varying success. The difficulty in isolating pure phases increases with the number of copper layers. The HgO solid precursor decomposes at low temperature (500 °C) into mercury and oxygen. So, the formation of the superconducting phases is due mainly to the reactions between the solid and vapour phases. The Hg released through the decomposition of HgO at $\approx$ 500 °C reacted with the CaO component readily to form $CaHgO_2$ at low temperatures (550-700 °C), and fast heating rates have been thought to inhibit the formation of $CaHgO_2$[105].

Now the precursor films were sintered with mercury HTSC powder. Use of mixtures of HgO and BaCaCuO precursor powder instead of pure HgO, was shown to control the Hg vapor pressure during the reaction [108]. Two different precursor mixtures have been used as described below. For both Re-Ba-Ca-Cu-O precursor could be intimately mixed with the required amount of yellow HgO to obtain the reaction mixture. Mercury vapors react with Re-Ba-Ca-Cu-O precursor by vapor phase transport during the high temperature reaction. The quality of precursor powder turned out to be one of the most crucial experimental parameter for the synthesis of $(Hg_{0.9}Re_{0.1})Ba_2CaCu_2O_{6+\delta}$ thin films. The procedure of filling, evacuating, and closing of the quartz tube is described before. Generally, the quartz tube had a length of 7.5 cm. The part of the tube containing the precursor film and the mercury HTSC mixture was pushed 21 cm into the furnace, being exposed to the hottest area. During the sintering process elementary mercury condensed at the colder end, as expected. One received the first superconducting film, as the quartz tube was inserted directly into the furnace pre-heated on 850 °C. 18 hours later, it was taken out and quenched into the air on room temperature. A two point measurement with an electrometer showed an electrical resistance of 400 Ω. Superconductivity was shown by susceptibility and the resistance measurements with the cooling of the sample in liquid nitrogen.

The procedure was based on the two-step process including preparation of Hg-free oxide precursors and their further mercurization at the final heat treatment

stage. During the second step of the preparation of $(Hg_{0.9}Re_{0.1})Ba_2CaCu_2O_{6+\delta}$ thin films (formation of HgRe-1212 by gas/solid diffusion), mercury films have been successfully prepared by two different methods:

-1. HgRe-212 precursor

After deposition of the precursor films, they were sealed into quartz tubes together with HgRe-212 precursor powder, which provide the Hg atmosphere. HgRe-212 was prepared by mixing HgO and the sintered precursor powder in an appropriate proportion according to the formula $(Hg_{0.9}Re_{0.1})Ba_2CaCu_2O_{6+\delta}$. The quartz tubes were sealed under vacuum (1 mbar), then the quartz tube was placed in a stainless-steel cylinder as a safety precaution. The temperature profile employed

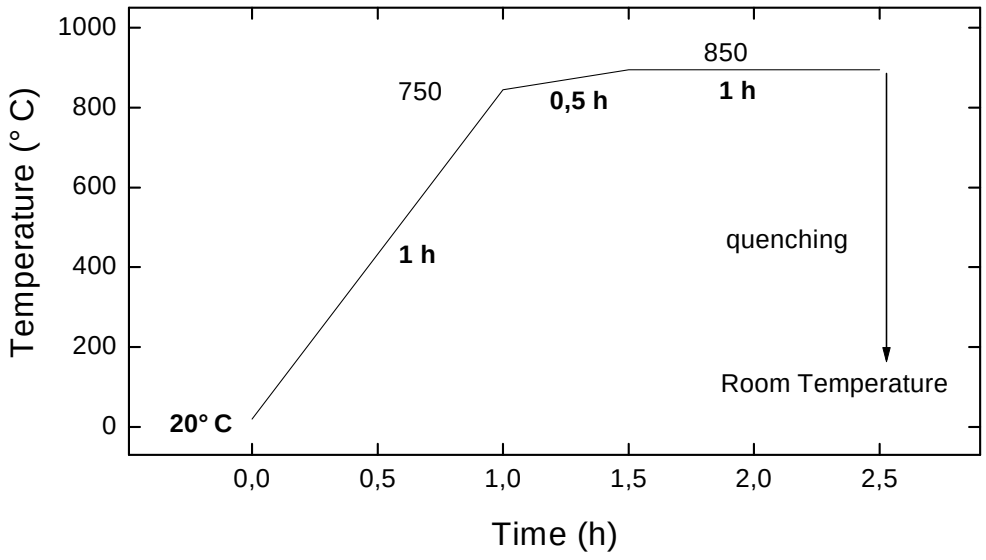

Figure 3.3: *Heat treatment schedule for $(Hg_{0.9}Re_{0.1})Ba_2CaCu_2O_{6+\delta}$ thin films.*

for Hg-annealing of the precursor films is shown in Fig. 3.3. The temperature profile reveals four distinct regions. First, the whole assembly was rapidly heated to 750 °C in 1 h (to overcome the problem $CaHgO_2$ formation), slowly heated up to 850 °C (100 °C in 30 min), and then kept at this temperature for 1 h. The long annealing time of 18 h used for the first superconducting film was not required.

Finally the tube was quenched to room temperature. This procedure leads to $(Hg_{0.9}Re_{0.1})Ba_2CaCu_2O_{6+\delta}$ thin films. If one reduced the mercury portion, the superconducting characteristics of the samples worsen. Half of the samples were not superconducting. Increasing of the mercury portion by 10 % led to the explosion of the quartz tube. The aluminium oxide tube did not give a sufficient protection. It broke into several parts. There was the danger of a still more violent explosion, the furnace tube would take damage. Therefore the Aluminium oxide tube was replaced by a one side closed high-grade steel tube. The steel tube was 12.3 cm long with an outside diameter of 25 mm and a wall thickness of 7 mm. One put and positioned the steel tube into the furnace with the quartz tube inside. Some of the films, which have been prepared by that procedure, are dominated by Hg-1212 containing a small amount of other phases as marked by asterisks (Fig. 4.8). As the final result, after several times by using this method, it appears that the major drawback of this method is the rather poor reproducibility of the films.

-2. HgRe-212 + Re212 precursor

The phase purity of $(Hg_{0.9}Re_{0.1})Ba_2CaCu_2O_{6+\delta}$ thin films depends on several synthesis parameters such as reaction temperature, and the partial pressures of mercury and oxygen during the synthesis. For a given mass of the reaction mixture, the mercury and oxygen partial pressures depend on the volume of the sealed reaction tube. Hence, it is necessary to keep the volume of the reaction tube fixed while synthesizing a series of samples with varying composition or temperature to optimize reaction conditions.

After the deposition the substrates with the precursor films were sealed into quartz tubes sandwiched by a HgRe-212 pellet on the film side and a Re-212 pellet on the substrate side. The HgRe-212 pellet provides the Hg-atmosphere to transform the precursor film into the HgRe-212 film. The ratio between Re-212 and HgRe-212 was approximately 1:3. The total quantity of the reaction powder of 0.641 g (consisting of 0.5 g $Re_{0.1}Ba_2CaCu_2O_{6+\delta}$ and 0.141 g HgO) was arbitrarily selected and was not of crucial importance for the production of superconducting films. The relationship of the partial pressure is also independent of the total quantity of the powder. The samples annealed in close proximity of the stoichiometric bulk pellet showed excellent superconducting characteristics

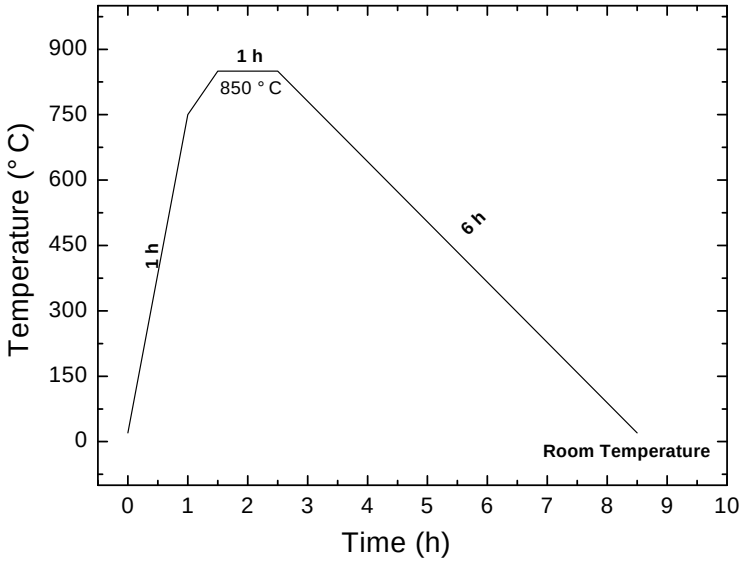

Figure 3.4: *Standard temperature profile employed for the formation of* $(Hg_{0.9}Re_{0.1})Ba_2CaCu_2O_{6+\delta}$ *thin films by gas/solid diffusion. This profile yielded best results.*

with high reproducibility while those placed as little as a centimeter away were not superconducting at all. In preparation for heat treatment, the quartz tubes (8 mm ID, 12 mm OD) were evacuated to 1 mbar and sealed off at a length of about 12 cm by a hydrogen torch.

In order to minimize the loss of mercury, a ßpace-fillingtechnique was developed. For $(Hg_{0.9}Re_{0.1})Ba_2CaCu_2O_{6+\delta}$ thin films, different methods were tried to reduce the empty space inside the quartz tube. A fused-quartz rod (7 mm OD, 50 mm length) was inserted in the quartz tube in order to reduce the free volume. The fused-quartz rod effectively reduced the open volume to a mass/volume ratio of approximatly 1 g/cm^3, this seemed to be important. Figure 3.4 depicts the standard temperature profile employed for Hg-annealing of the precursor films. The evacuated tubes were then fast heated to 750 °C in 1 h (to overcome the problem of $CaHgO_2$ formation), and then to 850 °C in 30 min and held at this temperature for 1 h. Finally the samples were cooled to room temperature in 6 hours. This standard temperature profile leads to high-quality $(Hg_{0.9}Re_{0.1})Ba_2CaCu_2O_{6+\delta}$ thin films, as shown in Fig. 4.1, Fig. 4.9, and Fig. 5.2.

The samples were stored in a dry box. They were exposed to air only during the XRD, SEM/EDX, and $\rho(T)$ measurements, which were performed under usual laboratory conditions.

It has to be pointed out that gloves, special mask, and cleaning of the pressing (tools) kit are very important as well as storing the Hg-containing waste in a proper container in order to prevent personal and environmental contamination.

Chapter 4

Electrical and structural characterization

This chapter outlines the characterization techniques utilized throughout this work with an emphasis on the application of these techniques to the characterization of superconducting $(Hg_{0.9}Re_{0.1})Ba_2CaCu_2O_{6+\delta}$ thin films. Samples were characterized by AC susceptibility measurements, X-ray diffraction, and scanning electron microscopy.

4.1 AC susceptibility measurements of Hg,Re-containing HTSC thin films

In addition to electrical resistivity, AC susceptibility χ is widely used as a non-destructive method for the determination and characterization of the intergrain component in high-T_c thin film superconductors. Experimentally, AC susceptibility, makes a step as a function of temperature, representing the transition from near-perfect screening to complete penetration of external AC magnetic field into the sample. Susceptibility measurements will give information about the magnetic nature of the samples, i.e., how susceptible the sample is to an outer field. The temperature dependence of the AC susceptibility of $(Hg_{0.9}Re_{0.1})Ba_2CaCu_2O_{6+\delta}$ thin films was measured in a field perpendicular to the film plane. The transitions of several $(Hg_{0.9}Re_{0.1})Ba_2CaCu_2O_{6+\delta}$ samples from the normal state to the superconducting state are measured with the magnetic susceptibility method. The

Figure 4.1: *The inductive component of the AC susceptibility for ten as-prepared* $(Hg_{0.9}Re_{0.1})Ba_2CaCu_2O_{6+\delta}$ *films.*

magnetic susceptibilities for ten successive as-prepared $(Hg_{0.9}Re_{0.1})Ba_2CaCu_2O_{6+\delta}$ thin films are shown in Fig. 4.1. High-quality $(Hg_{0.9}Re_{0.1})Ba_2CaCu_2O_{6+\delta}$ films (five samples-solid symbols) have been prepared using the method described in 3.4.2.(-2). Each has a sharp onset of the transition near 120 K. But in the other samples (five samples-open symbols) we used different parameters for the second step, we omitted the quartz rod and after annealing the samples were quenched to room temperature. The procedure according to 3.4.2.(-2) yielded far improved reproducibility.

Besides the high volatility and toxicity of Hg, the granular character of the thin film material and the severe air sensitivity of the cuprate precursor, the chemical and structural formation and stability of mercury phases, cause the main fabrication problems. Moreover, synthesized Hg-based cuprates are highly unstable under ambient conditions owing to their reaction with water vapour and CO_2. Several partial cation substitutions have been tried in order to further raise T_c and stabilize these compounds of difficult synthesis. Most of the investigated

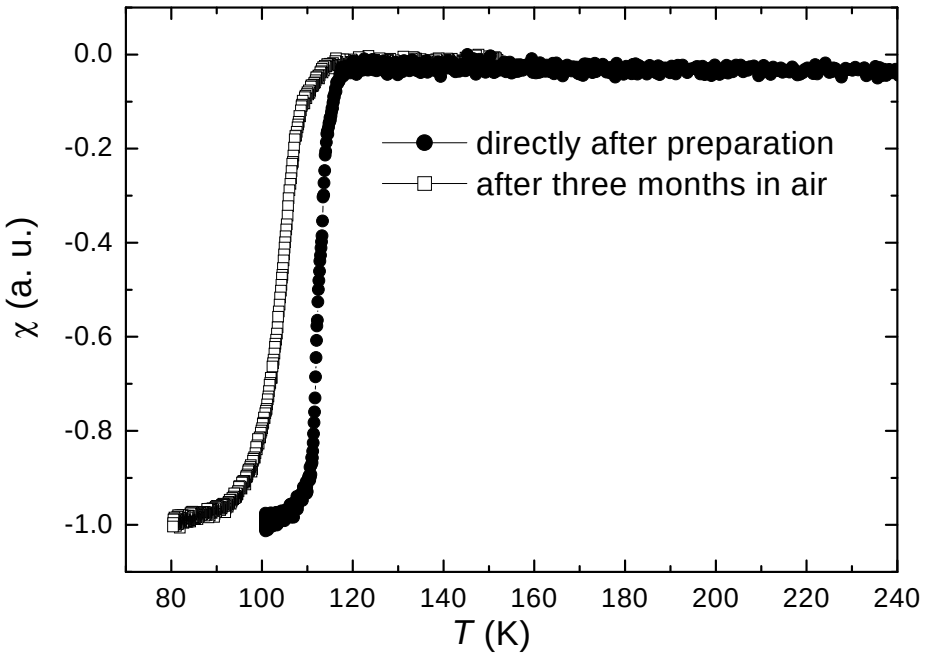

Figure 4.2: *AC susceptibility for as-prepared $HgBa_2CaCu_2O_{6+\delta}$ film directly after preparation (solid symbol) and after three months in air (open symbol).*

compositions are detrimental to T_c and do not result in a stabilization of the compounds. The remarkable exception is the partial substitution of Hg by Re, which has been demonstrated not to lower the maximal T_c and stabilize these phases. In the present work the partial substitution of Hg by Re doping of the precursor promotes the formation of Hg-1212 phases, and it improves their stability. The effect of Rhenium on the superconducting transition temperature T_c of the samples was examined by the temperature dependence of the AC susceptibility. The magnetic susceptibility for Hg-1212 thin films without Rhenium is shown in Fig. 4.2. The films without Rhenium were unstable and decomposed in the air within three months, as is shown in Fig. 4.2. The Re substitution makes it possible to work at normal pressures without a controlled atmosphere. We found that if the precursor target or the precursor material were used after one month from the preparation time the critical temperature is not in the range of the Hg-films and both, target and material, again were sintered with the parameter before usage. The sensitivity of the samples magnetic properties to humidity, and aging

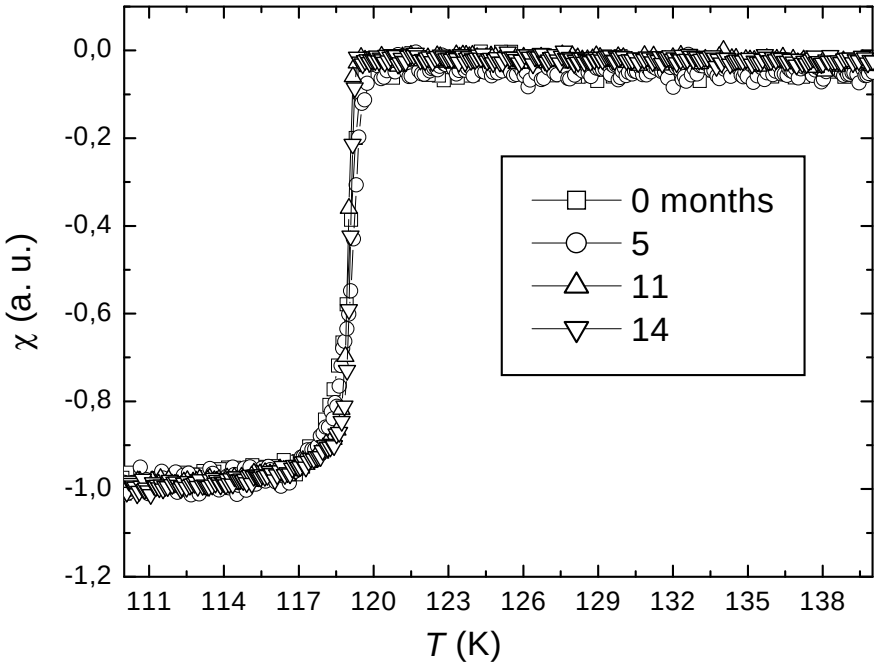

Figure 4.3: *AC susceptibility versus temperature dependence of investigated* $(Hg_{0.9}Re_{0.1})Ba_2CaCu_2O_{6+\delta}$ *thin film for four repeated measurements during 14 months.*

was tested by exposing Rhenium doping samples to ambient conditions over a 14 month period. It is documented in Fig. 4.3, where some of $\chi(T)$ dependences during 14 months for the best film are shown. No substantial differences in the behaviour of these curves were observed, within the accuracy of our measurements, and practically all curves lie on the same line. As we see, Rhenium doping of Hg-1212 superconductors greatly enhances their stability and phase formation without damping their intrinsic superconducting properties. Rhenium addition of the precursor decreases its air sensitivity and allows for much simpler precursor handling and processing techniques, where the treatment in a glove box is not necessary.

The annealing temperature of the second step had an important influence on the $(Hg_{0.9}Re_{0.1})Ba_2CaCu_2O_{6+\delta}$ sample's phase transition as seen in Fig. 4.4. In samples heat treated below 830 °C, HgRe-1201 and Ca_2CuO_3 are the dominate phases. In the annealing temperature range from 830 °C to 890 °C, the heat treatment led to the information of the HgRe-1212 phase. The transition tem-

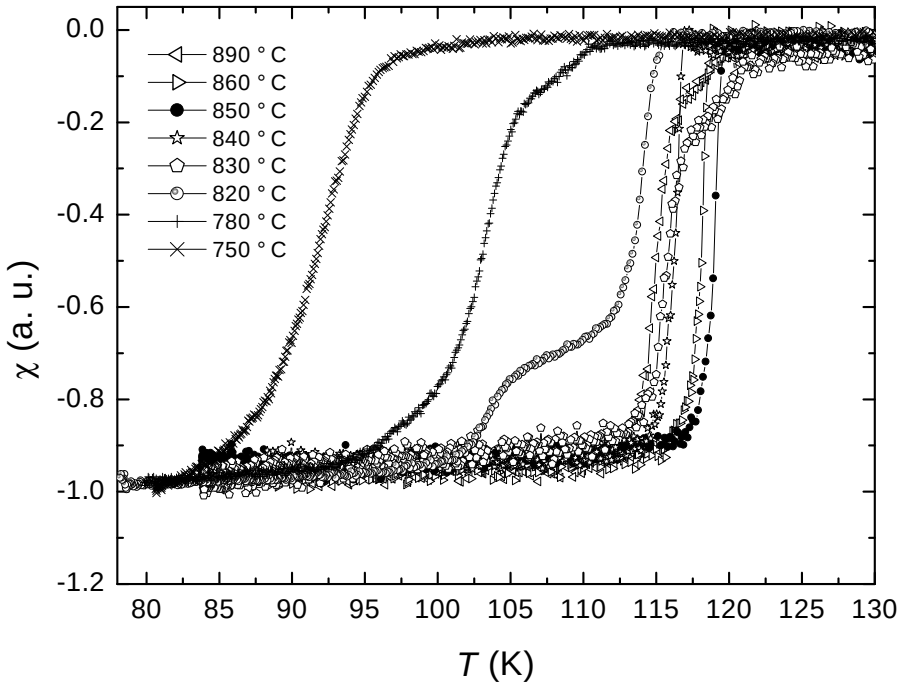

Figure 4.4: *AC susceptibility signal of* $(Hg_{0.9}Re_{0.1})Ba_2CaCu_2O_{6+\delta}$ *thin films annealed at different temperatures.*

perature varies with the annealing temperature. For samples annealed at 820 °C, two distinct superconducting transitions were detected at 116 K and around 105 K , where the former temperature indicates the HgRe-1212 phase. The knee at 105 K indicates the presence of weak links in the sample. For annealing temperatures of 830 °C and higher, the second transition at 105 K disappears. The phase pure $(Hg_{0.9}Re_{0.1})Ba_2CaCu_2O_{6+\delta}$ with a critical temperature of 120 K was formed at 850 °C, this is seen in the AC susceptibility signal shown in Fig. 4.4. The effects of heat treatment in oxygen on the superconductivity of $(Hg_{0.9}Re_{0.1})Ba_2$ $CaCu_2O_{6+\delta}$ thin films has been studied. Various workers have investigated the effect of heat treatment in oxygen on the critical parameters of mercury-based superconductors [134, 135, 136]. For instance, the systematic increase of T_c with the increasing oxygen-annealing temperature up to 340 °C has been seen [136]. In contrast to that, AC susceptibility measurement of the present Hg,Re-containing HTSC thin film before and after oxygen-annealing at 340 °C showed that the heat treatment in oxygen flow reduces the T_c significantly from 119 K to 115 K. This

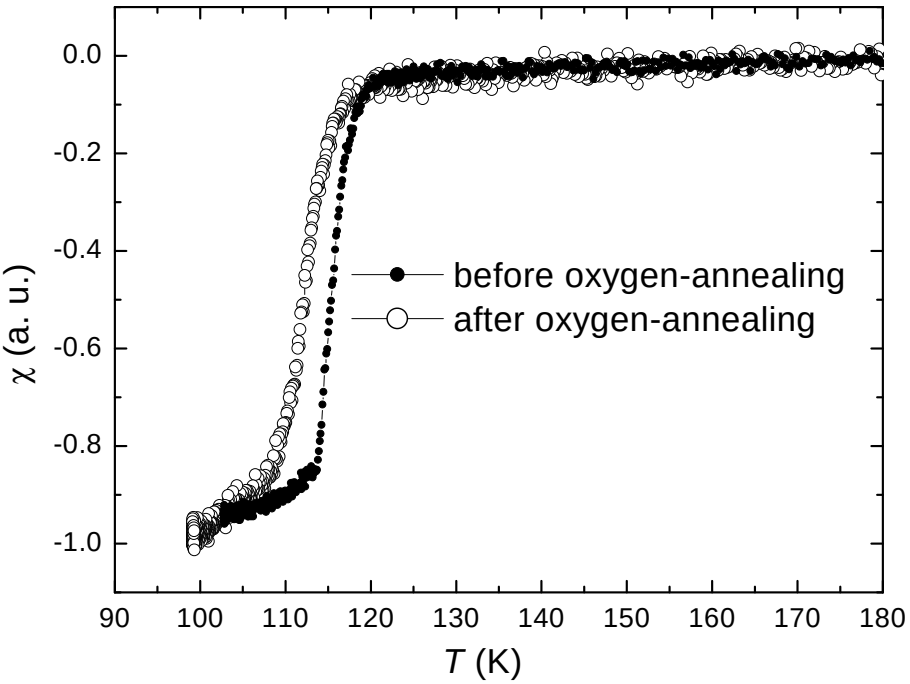

Figure 4.5: *Temperature dependence of AC susceptibility signal of the as-prepared* $(Hg_{0.9}Re_{0.1})Ba_2CaCu_2O_{6+\delta}$ *thin film and after oxygen-annealing at 340°C.*

is seen in the AC susceptibility signal shown in Fig. 4.5. The oxygen content seemed to be close to optimum already before annealing. The basic idea is that the superconductor synthesis occurs in a closed system and the stoichiometry of the oxygen in the superconductor sample, which is a very important parameter for the stabilization of the Hg-1212 phase is governed by the degree of the precursor oxidation. With this control the obtained superconductor samples do not need any further oxygenation post-treatment, as usually performed, since the degree of oxygenation of the final sample is pre-defined by the precursor material.

4.2 Structural characterization

A detailed structural characterization of the $(Hg_{0.9}Re_{0.1})Ba_2CaCu_2O_{6+\delta}$ thin films is important for an understanding of the superconducting properties due to their strong dependence on the composition. Consequently, X-ray diffraction (XRD), EDX, and scanning electron microscopy were applied to the films. The results of

the structural characterization are presented in this chapter.

4.2.1 X-ray diffraction

X-ray diffraction is a versatile, non-destructive technique used for crystal structure analysis and for identifying the crystalline phases of the materials. A rich variety of information can be extracted from XRD measurements. It is useful for determining texture, epitaxy, and lattice constants for epitaxial films. From the diffraction line parameters, position and shape of the line, one can obtain the unit cell parameters and microstructural parameters (grain size, microstrain, etc.) respectively. Rocking curves measure single Bragg peaks during sample tilt within the diffraction plane. They are useful for determining crystalline perfection. By using the flexibility of a four circle diffractometer one can obtain information about the orientation distribution of the crystallites (texture measurements).
In this work the phase composition of the samples was analyzed by a conventional Philips X-Pert MPD 2-circle X-ray diffractometer, which uses a collimated X-ray beam of (Cu K_α, wavelength $\lambda = 1.5418$ Å). X-ray diffraction (XRD) analysis ($\theta - 2\theta$ scans and rocking curves) was performed in order to check the orientation of the films.
The X-rays are diffracted (according to Bragg's law) by the crystal lattice of the material. The Bragg approach to diffraction is to regard crystals as built up in layers or planes, spaced a distance d apart, such that each acts as a semi-transparent mirror. The conditions for a sharp peak in the intensity of the scattered X-rays are that the X-rays should be specularly reflected and that the reflected rays from successive planes should interfere constructively. The derivation of Bragg's Law is shown in Fig. 4.6. For the reflected rays to interfere constructively, they must satisfy Bragg's Law:

$$2d \sin\theta = n\lambda \,, \tag{4.1}$$

where θ is the angle of incidence, the integer n is known as the order number of the reflection, and λ is a wavelength of an X-ray. For a given set of planes, several solutions of Bragg's Law are usually possible, for $n = 1$, 2, 3, etc. It is customary, however, to set n equal to 1 and for situations where, say, $n = 2$, the d-spacing is instead halved by doubling the number of planes in the set; hence n is kept equal to 1. Note that $2d \sin\theta = 2\lambda$ is equivalent to $2(d/2) \sin\theta = \lambda$. By

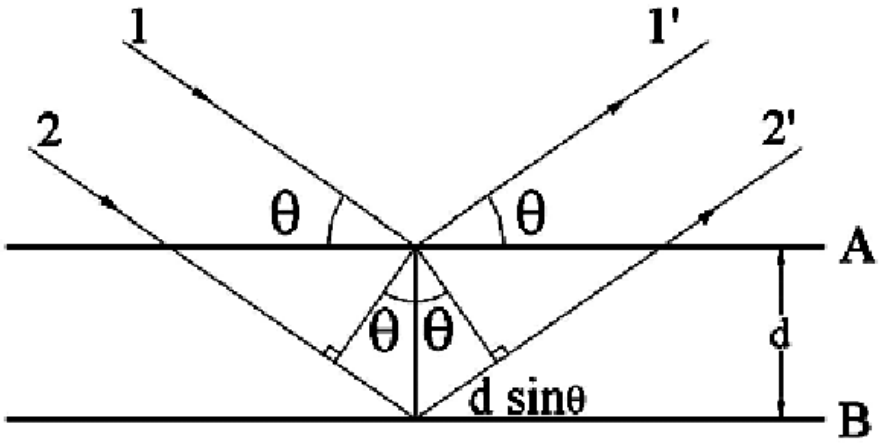

Figure 4.6: *Derivation of Bragg's Law for X-ray diffraction.*

varying the angle of incidence, a diffraction pattern emerges that is characteristic for the sample.

From the position of the peaks in the diffraction pattern phases, phase compositions were determined qualitatively with the help of a POWDER CELL program [137]. During the sample preparation, different precursor targets with the different sets of starting materials have been used to grow the Hg-HTSC thin films in this work. To show the role of precursor target type on the superconducting properties of Hg-1212 thin films, structural and crystallographic properties of the samples, which have been prepared from these targets, were investigated by X-ray diffraction analysis using a two-circle diffractometer.

After trying several times, the preparation of $(Hg_{0.9}Re_{0.1})Ba_2CaCu_2O_{6+\delta}$ thin films by using the target no 1 was successful. Samples prepared by this target exhibit $T_c \geq 116$ K. The XRD $\omega - 2\theta$ diffraction pattern of a superconducting $(Hg_{0.9}Re_{0.1})Ba_2CaCu_2O_{6+\delta}$ film on an $SrTiO_3$ substrate is shown in Fig. 4.7. As usual, the detector is oriented such that the angle between the incident beam axis and the detector is 2θ, where 2θ is the Bragg angle of planes in the epitaxial film. All major reflections in Fig. 4.7 are indexed as (00ℓ) peaks of the Hg-1212 phase, which indicates that the c-axis of the film is perpendicular to the surface. The strong (00ℓ) peaks of the HgRe- 1212 phase indicate the Hg-1212 phase to be dominant with a large degree of uniaxial alignment of the c-axis normal to the substrate. Some minor impurity peaks are also found in the pattern. The

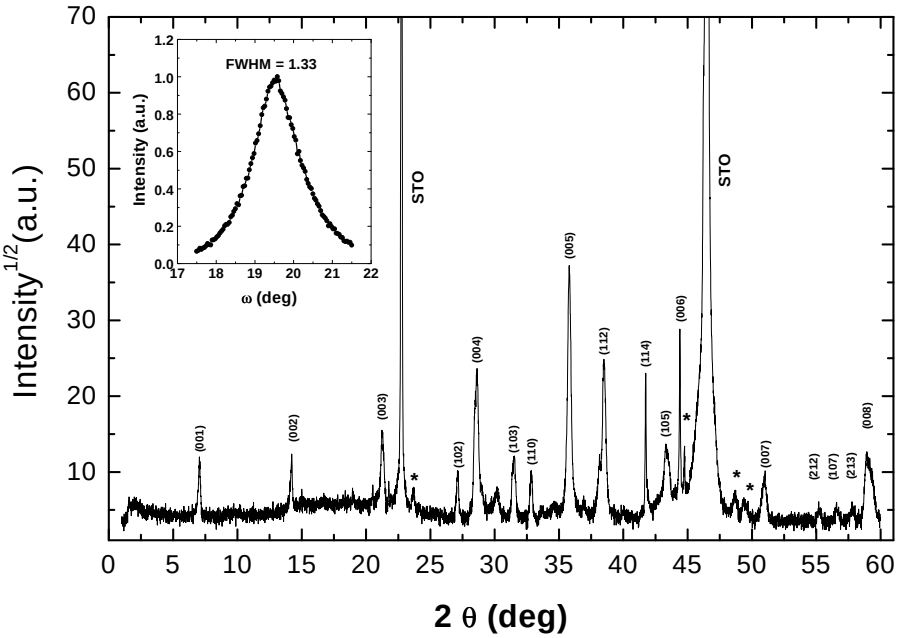

Figure 4.7: *XRD pattern (square root of intensity) for a* $(Hg_{0.9}Re_{0.1})Ba_2CaCu_2O_{6+\delta}$ *thin film. The HgRe-1212 phase is the dominant phase. The inset shows the rocking curve of the (005) peak. The impurity phases are marked by (*).*

experimental rocking curve is recorded in a ω-scan mode, that is, the film is rotated (rocked) through the Bragg angle, while the reflected beam is measured in a fixed counter with a slit. The ω-scan, or the rocking curve, gives the degree of preferred orientation in the film. In this work rocking curves were measured in order to determine the spread of the c-axis around the (001) axis. We know that the width of this rocking curve is a direct measure of the range of orientation of crystal. The peak width of this kind of rocking curve is due to a range of orientations of the lattice planes. The inset in Fig. 4.7 shows the XRD ω-scan of the (005) peak of the HgRe-1212 phase. The measured FWHM of this peak is $1.33\,^\circ$. For $(Hg_{0.9}Re_{0.1})Ba_2CaCu_2O_{6+\delta}$ thin films, the scan angle $\omega = \theta - \theta_{\mathrm{Bragg}}$ is measured relative to the Bragg angles $\theta_{\mathrm{Bragg}} = 23.26\,^\circ$ and $\theta_{\mathrm{Bragg}} = 17.89\,^\circ$ of the substrate and $(Hg_{0.9}Re_{0.1})Ba_2CaCu_2O_{6+\delta}$, respectively.

The X-ray diffraction (XRD) measurements which reveal the structure and the crystallographic orientation of the films $(Hg_{0.9}Re_{0.1})Ba_2CaCu_2O_{6+\delta}$ prepared from the second target are shown in Fig. 4.8. The X-ray-diffraction pattern shows

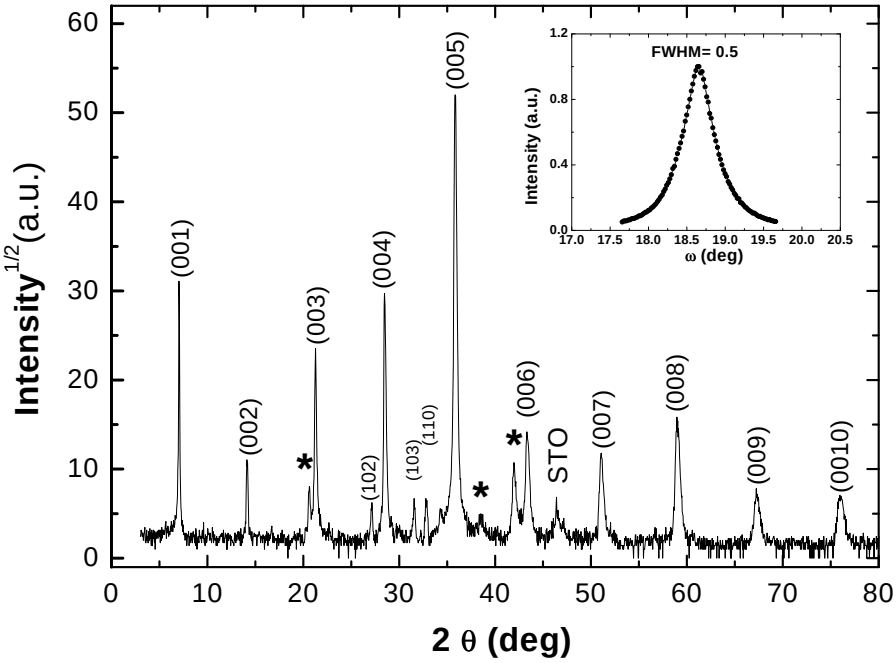

Figure 4.8: *XRD pattern (square root of intensity) for a* $(Hg_{0.9}Re_{0.1})Ba_2CaCu_2O_{6+\delta}$ *thin film prepared according to the procedure 3.4.2.(-1). The film is dominated by the Hg-1212 phase with a small portion of impurity phases. The inset shows the rocking curve of the (005) peak.*

mainly lines belonging to the c-axis-oriented Hg-1212 with minute traces of impurity phases. The strong peaks in Fig. 4.8 are identified as Hg-1212 (00ℓ), which indicates that the c-axisof the film is perpendicular to the surface. A value of $c = 12.52$ Å was thus obtained, which is slightly smaller than that of the bulk Hg-1212 material ($c = 12.7$ Å). The rocking curve (the inset of Fig. 4.8) shows a c-axis orientation of our films. The full width at half maximum (FWHM) of the rocking curve of the (005) peak is $0.5\,^\circ$, which shows the good orientation of the HgRe-1212 phase. This indicates a very high degree of orientation with the c-axis perpendicular to substrate.

The typical XRD $\omega - 2\theta$ patterns recorded for $(Hg_{0.9}Re_{0.1})Ba_2CaCu_2O_{6+\delta}$ films prepared from the third target are shown in Fig. 4.9. The X-ray-diffraction pattern collected within the range $3\,^\circ \leq 2\theta \leq 90\,^\circ$ using a conventional Philips X-Pert MPD 2-circle X-ray diffractometer shows all lines belonging to the c-axis-oriented

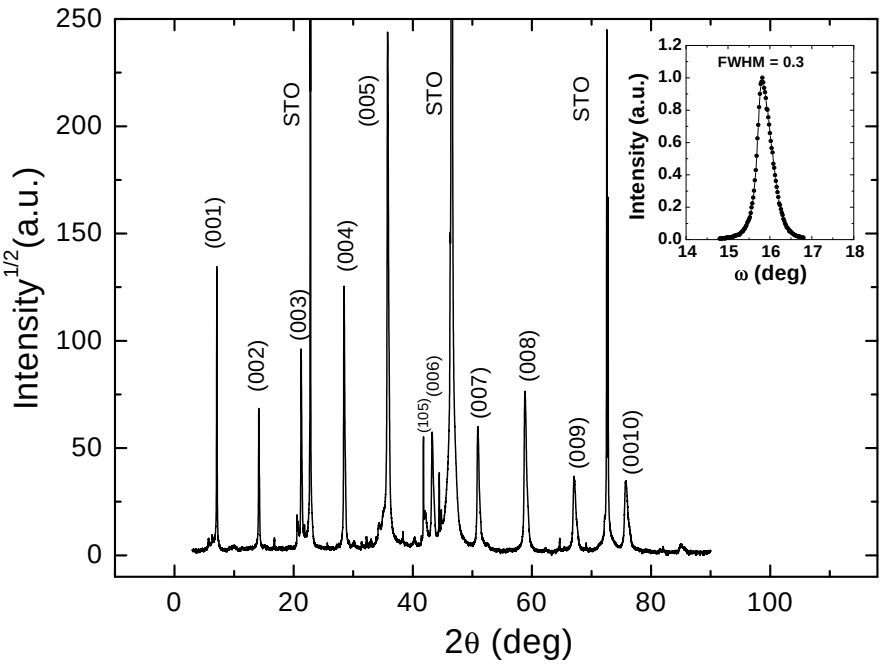

Figure 4.9: *XRD pattern (square root of intensity) for* $(Hg_{0.9}Re_{0.1})Ba_2CaCu_2O_{6+\delta}$ *thin film according to the procedure 3.4.2.(-2). The Hg-1212 phase is the dominant phase. The right inset shows the rocking curve of the (005) peak.*

Hg-1212. Thin film samples dominated by the Hg-1212 phase were produced in this modified process. As can be seen, mainly the reflections from planes perpendicular to the substrate are observed, i.e., all reflections (except of the substrate reflex) can be assigned to the (00ℓ) reflections of the film material, $h = k = 0$, $\ell \neq 0$. Only one weak reflection corresponding to (105) orientation is observed, indicating that the films were grown preferentially with the c-axis normal to the film plane. This indicates single-phase films and a growth direction of the films with the c-axis perpendicular to the substrate surface. In order to investigate the crystal quality of these $(Hg_{0.9}Re_{0.1})Ba_2CaCu_2O_{6+\delta}$ films, the rocking curves of the (005) peaks were explored by ω-scans. The rocking curve of the (005) reflection, had a full width at half-maximum (FWHM) of less than $0.3\,^\circ$. The rocking-curve width of the epitaxial $(Hg_{0.9}Re_{0.1})Ba_2CaCu_2O_{6+\delta}$ thin films, $\Delta\omega_{\mathrm{FWHM}} \leq 0.3\,^\circ$, is smaller than for in-situ grown vicinal $YBa_2Cu_3O_{7-\delta}$ [138] and vicinal and epitaxial $Bi_2Sr_2CaCu_2O_{8+\delta}$ [139] films. The typical rocking curves FWHM of the

$YBa_2Cu_3O_{7-\delta}$ (005) peak was around 0.458 ° for the vicinal films, and 0.148 ° for the c-axis films grown on well-oriented substrates [138] and for the vicinal $Bi_2Sr_2CaCu_2O_{8+\delta}$ films was around 1 ° [139] and 0.3 ° for epitaxial films [140]. This results demonstrate that $(Hg_{0.9}Re_{0.1})Ba_2CaCu_2O_{6+\delta}$ films prepared in this work on well-oriented substrates had the good crystalline quality and a high degree of c-axis orientation.

The experimental results, which are described before, clearly show that the film with the highest T_c corresponds to the best crystalline structure and the film with the lowest T_c corresponds to the most imperfect crystalline structure. It clearly shows that as the T_c value increases, the full width at half maximum (FWHM) of the rocking curves becomes narrower and narrower.

Texture analysis

Figure 4.9 shows a $\omega - 2\theta$ scan of the best HTSC $(Hg_{0.9}Re_{0.1})Ba_2CaCu_2O_{6+\delta}$ thin film that was deposited on (001) c-axis oriented $SrTiO_3$ substrate by pulsed laser deposition from the third target. Apart from the substrate peaks, mainly the peaks observed arise from the (00ℓ) planes of $(Hg_{0.9}Re_{0.1})Ba_2CaCu_2O_{6+\delta}$ thin film, indicating that a phase-pure $(Hg_{0.9}Re_{0.1})Ba_2CaCu_2O_{6+\delta}$ film with the c-axis normal to the film surface is obtained, i.e., that there was nearly no other orientation than (001) for the $(Hg_{0.9}Re_{0.1})Ba_2CaCu_2O_{6+\delta}$ thin films we studied. Now the texture, i.e., orientation distribution of crystallites in the sample using several diffractometer techniques shall be determined. Texture can range from completely ordered over partially ordered to completely random. A material is called textured if the grains are aligned in a preferred orientation along certain directions. One can view the textured state of a material as an intermediate state between a completely randomly oriented polycrystalline powder and a completely oriented single crystal. The phase identification and out-of-plane mosaic distribution was determined by XRD $\omega - 2\theta$ and ω-scans, while the in-plane epitaxial alignment between the film and substrate, i.e., the crystalline in-plane order of the samples was determined by Φ-scans to verify the in-plane alignment of their a-axes, where Φ is the in-plane azimuthal angle. All these XRD measurements were made using Cu Kα X-rays from a rotating anode and a high-resolution four-circle diffractometor with a focussing monochromator (OSMIC Max-Flux^{TM} Optic). The angles ω, 2θ, ϕ, and χ were according to the standard definition used in

Figure 4.10: *A schematic description of the angles used in this study; see also the text.*

XRD. They represent the angle of the incident beam, the angle between the incident and diffracted beams, the rotation angle, and the angle between the ϕ axis and the diffraction plane, respectively. The geometry of the XRD measurements is depicted in Fig. 4.10.

The crystalline surface of the substrate can work as a template for epitaxial film growth. Epitaxial means that the film has a crystallographic orientation relationship to the substrate. The ϕ-scan and the q-scan are measured to provide quantitative data for crystalline perfection, texture, and epitaxy. The reflections of the $\{104\}$ planes of the $(Hg_{0.9}Re_{0.1})Ba_2CaCu_2O_{6+\delta}$ film are shown in Fig. 4.11. Since the $(Hg_{0.9}Re_{0.1})Ba_2CaCu_2O_{6+\delta}$ film has tetragonal structure, four peaks should appear for a ϕ-scan pattern in a range of $360\,^\circ$ with every $90\,^\circ$ interval. As can be seen in Fig. 4.11 the $(Hg_{0.9}Re_{0.1})Ba_2CaCu_2O_{6+\delta}$ film has a well-defined fourfold symmetry and the intensities of the peaks are almost same, which demonstrates that the crystal has the best structural quality. An in-plane epitaxial relationship corresponding to $(Hg_{0.9}Re_{0.1})Ba_2CaCu_2O_{6+\delta}$ [104] $\parallel$ STO [101] exists.

The four peaks at $90\,^\circ$ intervals in the ϕ-scan of the $(Hg_{0.9}Re_{0.1})Ba_2CaCu_2O_{6+\delta}$ film make evident the existence of an in-plane order of the film. Additionally, the crystalline in-plane order was verified by 4-circle X-ray q-scans of the $\{hk4\}$

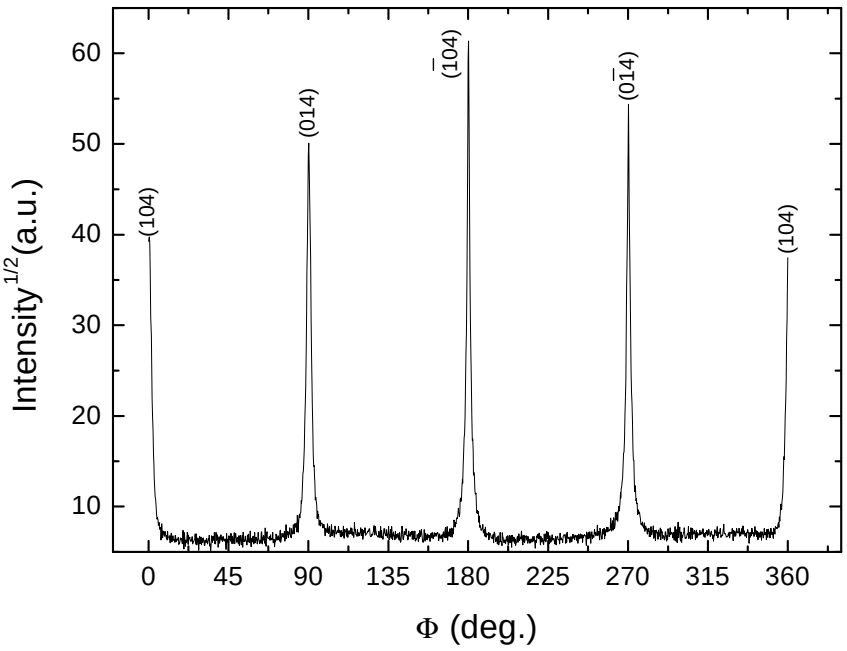

Figure 4.11: *X-ray (square root of intensity) ϕ-scan of the* {104} *reflection peaks for a fully textured ($Hg_{0.9}Re_{0.1}$)$Ba_2CaCu_2O_{6+\delta}$ thin film. The four peaks at 90° intervals in the ϕ -scan of the ($Hg_{0.9}Re_{0.1}$)$Ba_2CaCu_2O_{6+\delta}$ film make evident the existence of an in-plane order of the film.*

planes. Figure 4.12 shows an intensity mapping of the $\{hk4\}$ plane of the reciprocal space of the selected sample. The central intensity spot is the (004) reflection. The surrounding spots are the (104), (114), (014), and symmetry equivalent reflections. The distribution of intensity around the (004) reflection of a thin $(Hg_{0.9}Re_{0.1})Ba_2CaCu_2O_{6+\delta}$ film on STO substrate, showing good in-plane orientation. The same was found to be the case for the films that were prepared by using the second and the third target. These observations confirmed the high crystalline quality and good epitaxy of the $(Hg_{0.9}Re_{0.1})Ba_2CaCu_2O_{6+\delta}$ thin films. In conclusion, the in-plane alignment was measured by a ϕ-scan of the {104} peak of $(Hg_{0.9}Re_{0.1})Ba_2CaCu_2O_{6+\delta}$, as shown in Fig. 4.11. The four strong equally separated peaks, with a FWHM value of 0.3 °, indicate the excellent in-plane alignment of the Hg-1212 phase.

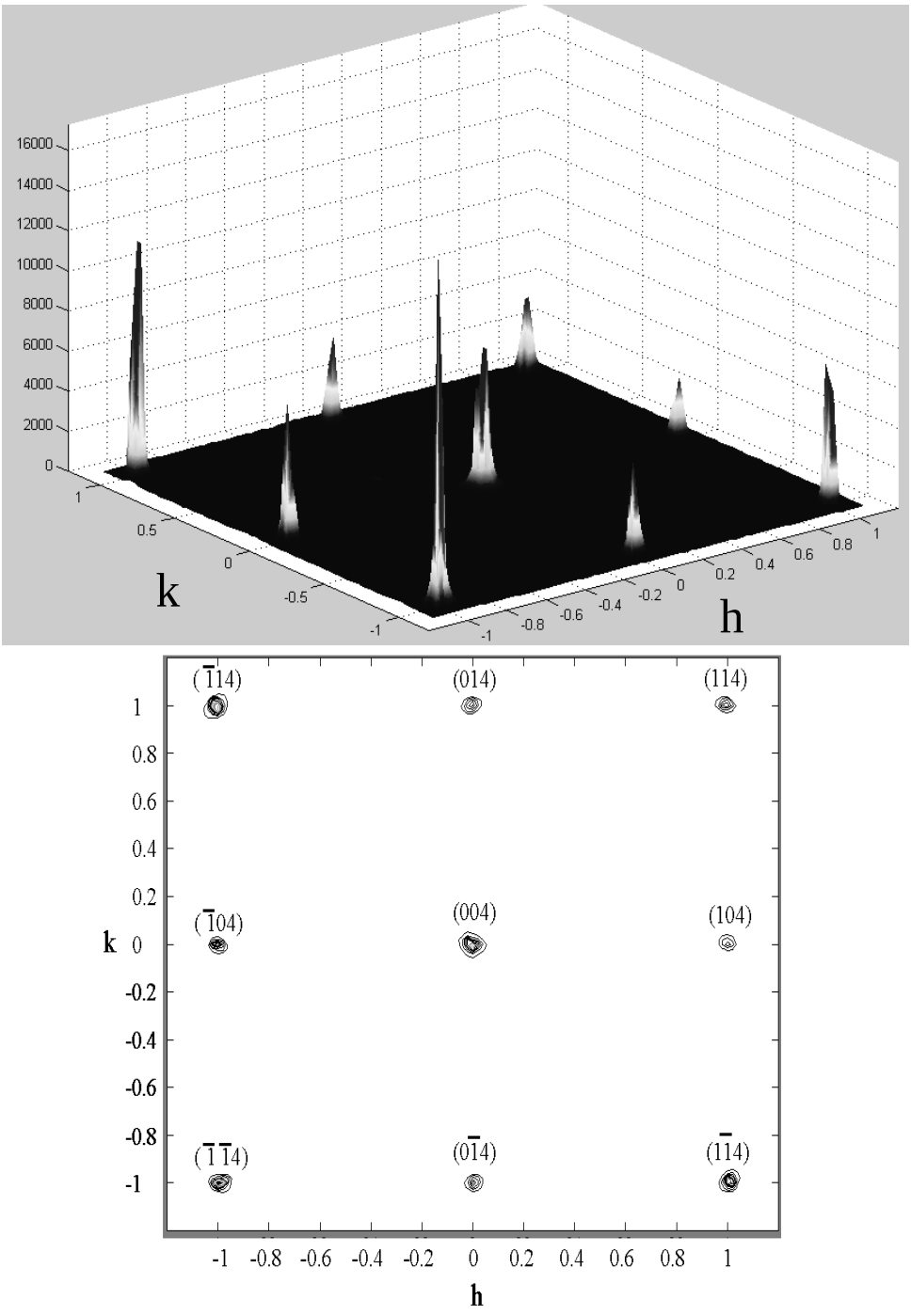

Figure 4.12: *A three and two-dimensional reciprocal-space map of an intensity mapping of the $\{hk4\}$ plane of the reciprocal space for a fully textured $(Hg_{0.9}Re_{0.1})Ba_2CaCu_2O_{6+\delta}$ thin film. The central intensity spot is the (004) reflection. The surrounding spots are the (104), (114), (014), and symmetry equivalent reflections.*

4.2.2 Scanning electron microscopy

Surface morphology of the films and chemical composition were studied using scanning electron microscopy (SEM) and energy dispersive X-ray microanalysis (EDX). In SEM a finely focused electron beam scans the samples along closely spaced lines. As a result of the interaction between the electron beam and the specimen secondary plus backscattered electrons and X-rays are produced. Using special detectors, a variety of signals can be generated giving specific information about the irradiated volume. The maximum lateral resolution can be obtained by using secondary electrons. These electrons have a low energy (1-50 eV) and escape and contribute to the signal. Under these conditions, the resolution is practically given by the electron beam size at the surface of the sample (5-10 nm). Figure 4.13-a shows typical scanning electron microscope (SEM) picture for the surface of the mercury-free precursor film with the nominal composition $Re_{0.1}Ba_2CaCu_2O_{6+\delta}$ exposed to air. No prominent surface structure is seen on the surface of the mercury-free precursor film. In contrast, corrugation of the surface is observed in Figs 4.13-b and 4.13-c for the mercury-free precursor surface of the latter film after annealing in mercury-vapor atmosphere. Figures 4.13-b and 4.13-c showed the rough surface of the $(Hg_{0.9}Re_{0.1})Ba_2CaCu_2O_{6+\delta}$ thin film. In the figures, it is found that the film contains certain clusters of small square-shaped grains which are distributed everywhere in the surface of the $(Hg_{0.9}Re_{0.1})Ba_2CaCu_2O_{6+\delta}$ thin film. The surfaces of the film showed a coarse-grained morphology with holes and some distorted plate-like grains. Two distinct morphologies of the film were recognized in the backscattered electron images: needle-like crystals in Fig. 4.13-b and a woolly object on the film surface in Fig. 4.13-c.

EDX of the thin films was carried out at 12 keV using the M-line of Hg, the L-line of Ba, and the K-lines of Ca and Cu. EDX showed the composition of the mercury-free precursor film to be $Re_{0.1}Ba_{2.2}Ca_{1.12}Cu_{2.1}O_x$ and for the latter film after annealing in mercury-vapor atmosphere $Hg_{0.9}Re_{0.1}Ba_{2.3}Ca_{1.3}Cu_{2.7}O_x$.

Figure 4.13: *Scanning electron microscope (SEM) images of the mercury-free precursor Re-212 (a) and the* $(Hg_{0.9}Re_{0.1})Ba_2CaCu_2O_{6+\delta}$ *(b and c) thin films, (b) and (c) surface of the latter film after annealing in mercury-vapor atmosphere.*

Chapter 5

Vortex dynamics and vortex phase transitions

5.1 Phase transitions measurements

The resistance measurements $\rho(T, B)$, of the $(Hg_{0.9}Re_{0.1})Ba_2CaCu_2O_{6+\delta}$ films were performed by a conventional four-probe method in a ^{4}He system, with a variable temperature insert (VTI) cryostat (Oxford Instruments) equipped with a 15 Tesla superconducting solenoid. The temperature T was measured with a carbon-glass thermometer with an accuracy in the range of 5 mK. The cryostat is made up of coaxial cylindrical chambers; the outer chamber is filled with liquid nitrogen that is very well separated from exterior by a thin layer of vacuum. Another vacuum layer separates the liquid nitrogen from the inner layer; which contains liquid ^{4}He at 4.2 K. The probe sits inside the VTI which is sealed from the liquid helium except for a needle valve, which allows the user to control the amount of ^{4}He flow through the VTI. By pumping the ^{4}He to about 150 mbar by using membrane pump and decreasing the pressure in the VTI it is possible to bring the temperature down to 1.2 K. The use of a direct current as a source is problematic as it introduces thermal effects in the sample or in the wires connecting the sample to the measurement system. Such thermoelectric phenomena as the Seebeck effect or the Thomsen effect can produce voltages of the order of a μV. Therefore, we used both current directions for our resistance measurements to average out thermoelectric effects. The critical temperature T_c

Figure 5.1: *Definitions of the critical temperature for two different measurement techniques.*

was determined from the midpoints of the $\rho(T, B)\mid_{B=const}$ curves.

5.1.1 Transition temperature

Before proceeding to the discussion of magnetic and transport properties of $(Hg_{0.9}Re_{0.1})Ba_2CaCu_2O_{6+\delta}$ superconducting thin films, it is helpful to say a few words about the transition temperature. There are various ways of defining the position of the superconducting transition temperature T_c and sharpness or width of the transition, and the literature is far from consistent on this point. The onset T_c is normally taken as the temperature where the first deviation from the a normal state can be seen, i.e., where the resistivity starts to drop significantly or a part of the sample first becomes diamagnetic. The usual interpretation of T_c, however, is that the resistivity vanishes or that a specially defined point in susceptibility measurements is reached, where the extensions of the normal-state plot and the steepest part of the slope intersect, as indicated in Fig. 5.3. Authors use terms like the onset, 5 %, 10 %, midpoint, 90 %, 95 %, and zero resistance points, and Fig. 5.2 shows some of these on the experimental resistance curve for $(Hg_{0.9}Re_{0.1})Ba_2CaCu_2O_{6+\delta}$ thin film. The T_c values that are determined in the present work of the $(Hg_{0.9}Re_{0.1})Ba_2CaCu_2O_{6+\delta}$ thin films are ordinarily midpoint values at which $R(T)$ has decreased by 50 % below the normal state resistivity. The point at which the first derivative of the resistance curve, shown in the lower inset of Fig. 5.2, reaches its maximum value could be selected as defining T_c, since

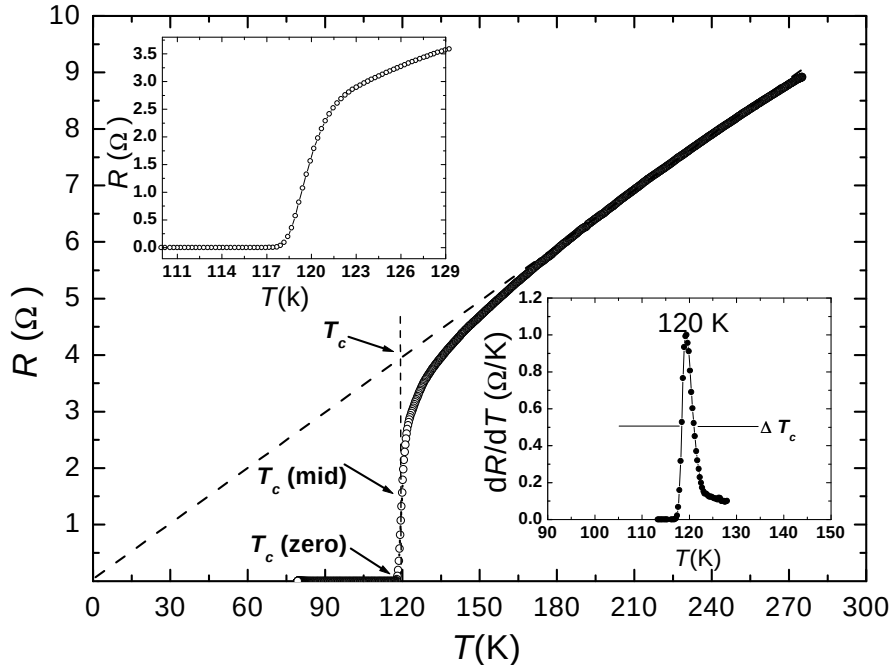

Figure 5.2: *Sharp drop to zero resistance of a* $(Hg_{0.9}Re_{0.1})Ba_2CaCu_2O_{6+\delta}$ *epitaxial thin film. The* T_c *(mid point), and* T_c *(zero) are indicated on the resistance curve. The upper inset is magnified at the temperature region of 110-125 K for the sake of clarification. The lower inset illustrates the determination of* T_c *as the maximum of the temperature derivative of the resistivity.*

it is the inflection point of the original curve. The width ΔT between the half-amplitude points of the first derivative curve is a good quantitative measure of the width of the transition. At high temperatures (160 K$< T <$ 270 K), the resistivity shows a linear dependence with temperature. This behavior is described by

$$R_{xx} = R_0 + \frac{dR_{xx}}{dT}T, \tag{5.1}$$

where $\frac{dR_{xx}}{dT} = 0.032$ (Ω /K) and R_0 in this sample $= 0$. Above and closer to the superconducting transition temperature T_c, the longitudinal resistivity exhibits a pronounced rounding, which is attributed to strong effects of thermal fluctuations [28]. In high temperatures, T $>$ 160 K, it is observed that the longitudinal resistivity R_{xx} has an approximately linear temperature dependence contrary to

non-doped Hg-samples, as reported by other authors [28].

5.1.2 Zero resistance

The AC susceptibility measurement, as an experimental technique, is very useful in studying the magnetic properties of materials, especially of the magnetic phase transitions where the response of magnetic moments in low field is of great importance. Its applications have rapidly increased with the spreading of investigations of high temperature superconductors because a number of parameters can be obtained from AC susceptibility measurements within the critical state model of type II superconductors [141]. Resistivity, on the other hand, is easier to measure, and can be a better guide for applications. Although the theoretical transition from the normal to the superconducting state is very sharp, experimentally it sometimes occurs gradually and sometimes abruptly. Generally, the T_c value determined from the resistivity drop to zero occurs at a somewhat higher temperature than its susceptibility counterpart. Figure 5.3 shows the sharp drop in resistance of $(Hg_{0.9}Re_{0.1})Ba_2CaCu_2O_{6+\delta}$ thin films that occurs at $T_c \approx 124$ K. No annealing in argon or oxygen was necessary to enhance T_c, which suggests that as prepared samples had close to optimal hole concentrations. We can see in the upper inset of Fig. 5.3 that there is an analogous drop in susceptibility at $T_c \approx$ 120 K. This happens because any tiny part of the material going superconductive loses its resistance, and $R = 0$ when one or more continuing superconducting paths are in place between the measuring electrodes. In contrast, AC susceptibility measurements depend on macroscopic current loops to shield the B field from an appreciable fraction of the sample material, and this happens when full superconducting current paths become available. Therefore, filamentary paths can produce sharp drops in resistivity at temperatures higher than the temperatures at which there are pronounced drops in diamagnetism, which also require extensive regions of superconductivity.

5.1.3 Thermal activation

Magnetic flux can penetrate a type-II superconductor in the form of Abrikosov vortices (also called flux lines, flux tubes, or fluxons) each carrying a quantum of magnetic flux $\phi_0 = h/2e$. These tiny vortices of supercurrent tend to arrange

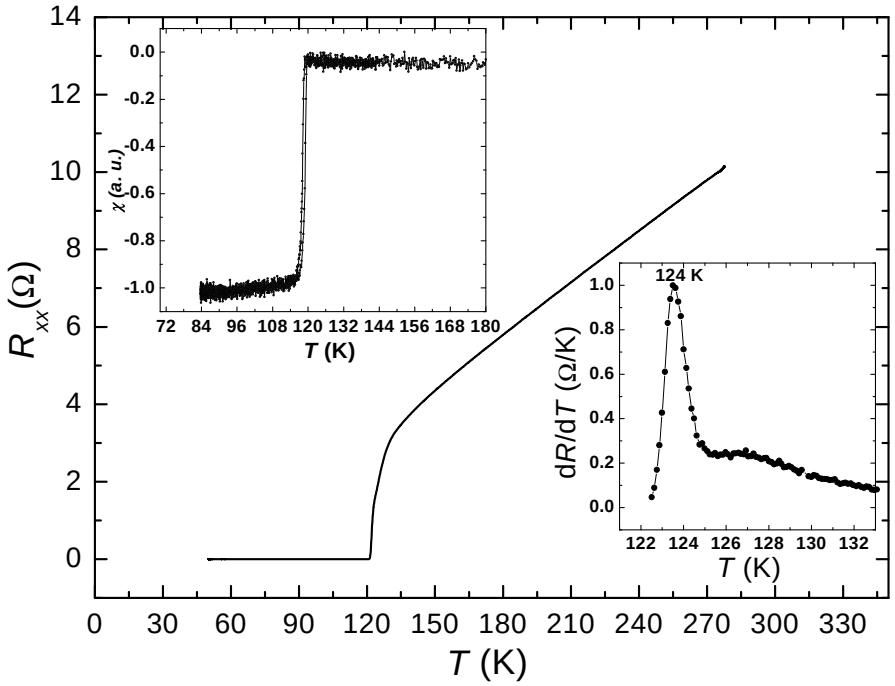

Figure 5.3: *Temperature dependence of the electrical resistance and the ac susceptibility for a* $(Hg_{0.9}Re_{0.1})Ba_2CaCu_2O_{6+\delta}$ *thin film measured in zero field. The upper inset is a relation between the inductive component of the ac susceptibility and temperature. The lower inset shows the relation between the temperature derivative of the resistive transition and the temperature.*

themselves in a triangular flux-lie lattice (FLL). The FLL interacts with pinning in a collective manner, described by the pinning strength and concentration, the presence of thermal fluctuations, and the elastic properties of the lattice. In the high-T_c superconductors, more exotic effects are found when thermal fluctuations become large. When the temperature is increased, the role of thermal fluctuations becomes increasingly important. It is shown [142, 143] that vortices will be able to move or creep due to thermal activation of the vortices, even when the driving current alone would not suffice to depin the system. The flux creep can usually be expressed in terms of an activation energy for flux motion, $U(J)$. In conventional type-II superconductors the creep is experimentally observed as a decay of the persistent current in a hollow cylinder containing trapped flux [144]. Due to the flux gradient in such a setup, there will be a driving force trying to push vortices

out through the cylinder wall.
The vortex motion will be unhindered as long as the screening current density is higher than the depinning J_c, and therefore the trapped flux will rapidly decay until $J = J_c$. But as soon as $J \leq J_c$ the pinning becomes effective and no further decay should occur.
In the basic flux-creep model vortex bundles are assumed to be thermally excited over barriers separating one place of strong pinning from another. The rate of successful jumps then is proportional to a Boltzmann factor $\exp\{-U/k_BT\}$, where U is given by the pinning energy U_0 of a typical bundle of volume V_c, but modified by the driving force JBV_c times the jumping distance δ. For a jump along the driving force, the effective activation energy then is

$$U = U_0 - JBV_c\delta = U_0(1 - J/J_c), \tag{5.2}$$

where J_c is the critical current density in absence of flux creep, defined to give a disappearing U at $J \to J_c$. Assuming that δ stays the same for all jumping directions, the electrical field becomes proportional to the difference in rate of jumps along and opposite to the Lorentz force [145] so that the electrical field E is given by

$$E \propto \exp\{-U_0/k_BT\} \sinh\left(\frac{U_0}{k_BT}\frac{J}{J_c}\right). \tag{5.3}$$

This is a strongly nonlinear response, $E \propto \exp(J/J_c)$ for $J/J_c > (U_0/k_BT)^{-1}$, and corresponds to a logarithmic decay of screening current with time, in general agreement with experiments on low-T_c materials [146]. For $U_0/k_BT \gg 1$ and $J \simeq J_c$, jumps in the forward direction are dominating. Equation (5.3) can then be simplified to $E \propto \exp\{-U(J)/k_BT\}$, with $U(J)$ given by Eq. (5.2). The proportionality factor of Eq. (5.3) is usually extract from experiments and it can be both field and temperature dependent, but does not depend on J in the simple description of Eq. (5.2).

5.1.4 Thermally assisted flux flow

In a type-II superconductor in the mixed state the flux lines are fixed at pinning centers, i.e., for example at defects or impurities. The main mechanism of the flux creep, yielding the resistive transition broadening in a magnetic field, is the

thermal activation of the flux-line motion over the energy barrier, U, of the pinning center [147]. Even at low currents $J \ll J_c$, some type-II superconductors in a magnetic field show a linear (ohmic) resistance well below T_c. This is especially the case for high-T_c materials. In the presence of a magnetic field the resistive transition shows a remarkable broadening, that is generally discussed within the framework of thermally activated flux-flow (TAFF) [148], superconducting fluctuations [149], and the vortex-glass transition [150]. The energy dissipation resulting from flux motion induces a sample resistivity proportional to the magnitude of flux in motion. Thus, in an applied magnetic field, as the temperature is lowered through T_c, the transition to zero resistivity is widened. With a small driving current, the Lorentz force on the flux is small and flux motion is dominated by thermally activated depinning. Therefore the resistive transition is also dominated by thermal activation. As the increase in flux pinning reduces the thermal activation and thus effects the behaviour of the resistive transition by acting to reduce the magnetic broadening. The action of the flux pinning centers in reducing the motion of the flux lines lowers the energy dissipated in the superconductor and hence the resistivity of the sample.

The electrical resistivity $\rho(T)$ in the presence of a magnetic field parallel and perpendicular to the c-axis of the $(Hg_{0.9}Re_{0.1})Ba_2CaCu_2O_{6+\delta}$ film plane for one of the investigated films is shown in Fig. 5.4 and Fig. 5.5, respectively. The transition width is about 1 K in zero and low magnetic fields but increases by increasing fields. On increasing B, the resistive transitions of the $(Hg_{0.9}Re_{0.1})Ba_2CaCu_2O_{6+\delta}$ films are broadened, i.e., in a large interval of temperatures T below T_c, the electrical resistivity $\rho(T, B)$ does not vanish, the broadening being the largest at the resistive onset. Because of the anisotropy, the response of the material is not only dependent on the magnitude of the magnetic field, but also on the orientation of it. The anisotropy of the magnetic field induced broadening of the resistive transition is related to the anisotropic layered crystalline structure composed of superconducting CuO_2 planes separated by non-superconducting layers. The transition temperature decreases strongly upon applying a magnetic field parallel to the c-axis. For magnetic fields perpendicular to the c-axis, i.e., parallel to the CuO_2 planes, the broadening is much smaller. The anisotropy is stronger than that of $YBa_2Cu_3O_{7-\delta}$ (YBCO) but less pronounced than in Bi-2212 and Tl-2212. The reduced broadening when the field is aligned perpendicular to the c-axis is

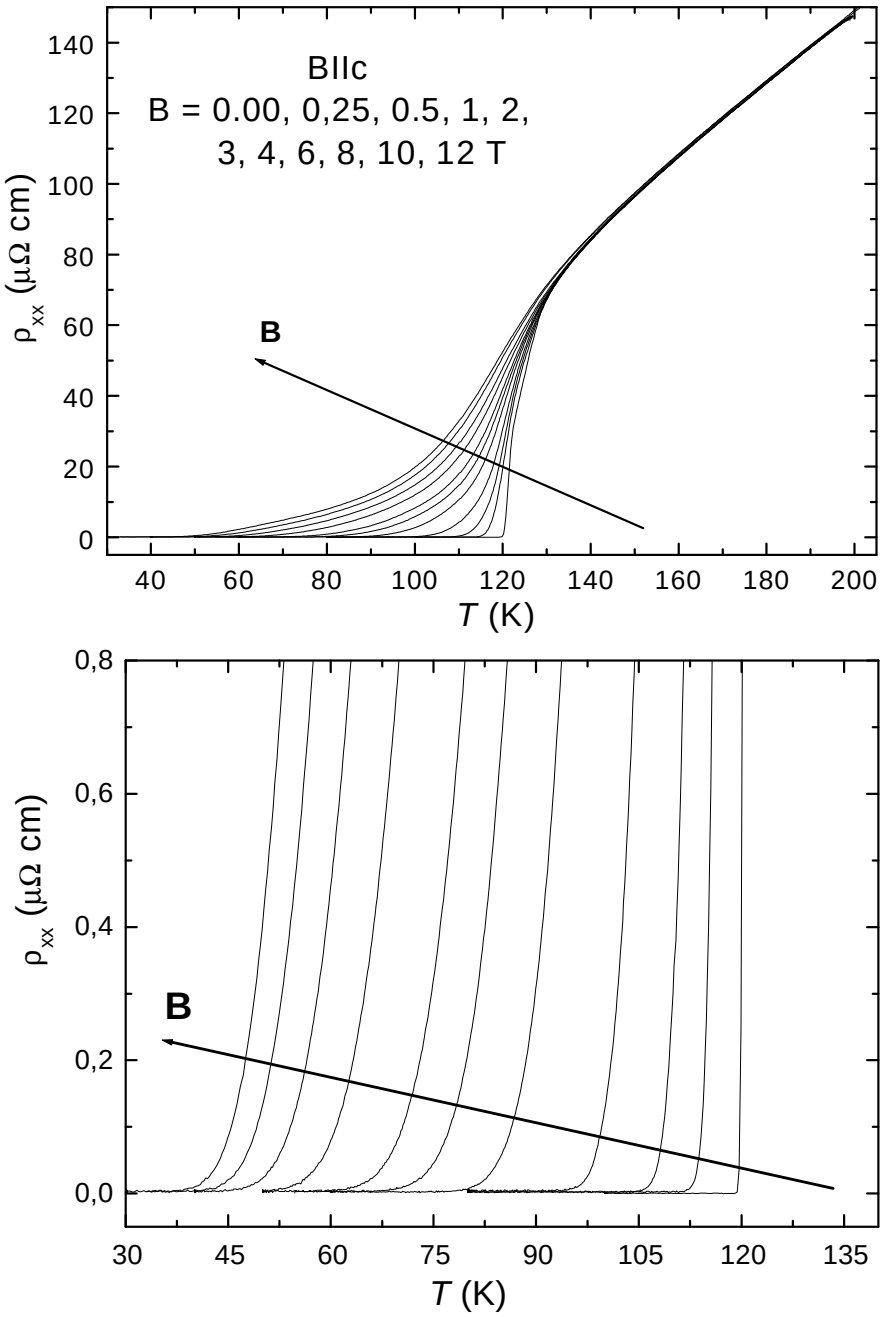

Figure 5.4: *Temperature dependence of the electrical resistivity for a $(Hg_{0.9}Re_{0.1})Ba_2CaCu_2O_{6+\delta}$ film as a function of the magnetic field up to 12 T, oriented parallel to the c-axis. The lower part of the figure is a magnification by more than a factor 100 to emphasize the exponential behavior.*

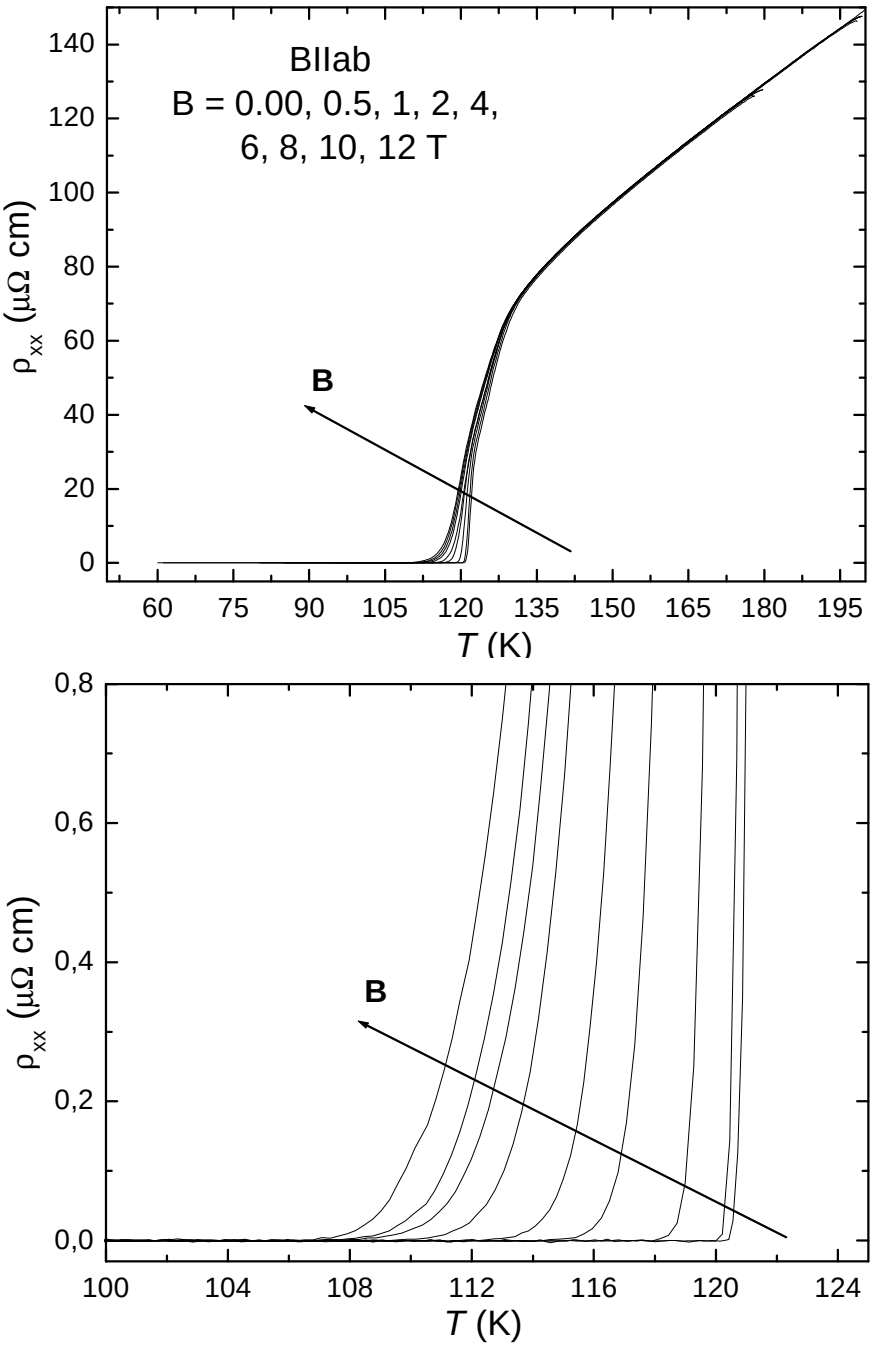

Figure 5.5: *Temperature dependence of the electrical resistivity for a* $(Hg_{0.9}Re_{0.1})Ba_2CaCu_2O_{6+\delta}$ *film as a function of the magnetic field up to 12 T, oriented perpendicular to the c-axis. The lower part of the figure is a magnification by more than a factor 100 to emphasize the exponential behavior.*

due to the intrinsic pinning provided by the non-superconducting layers in the structure.

5.2 Scaling behavior of the activation energy

The critical parameter of the thermally activated flux motion in the mixed state is the activation energy. Therefore we have studied the scaling behavior of the activation energy of high quality epitaxial *c*-axis oriented $(Hg_{0.9}Re_{0.1})Ba_2CaCu_2O_{6+\delta}$ superconducting thin films as a function of temperature and magnetic fields up to 12 T (parallel and perpendicular to the *c*-axis). The main idea is to measure the resistive transitions in a magnetic field parallel to the c-axis. For low-T_c superconductors, one observes a shift of the transition temperature related to the upper critical field and a slight broadening of the transition. In contrast, high-T_c superconductors show a strong broadening of the transition with a long thermally activated tail [45, 151]. This behavior is ascribed to flux flow and thermally activated flux flow [45]. From these resistive transitions one can extract the activation energy U for flux motion as a function of temperature and magnetic field. This activation energy corresponds to the process with the smallest energy that allows for flux motion. The activation energy has been determined from resistive measurements. Measurements of the magnetoresistivity versus the temperature were performed with dc magnetic fields up to 12 T parallel and perpendicular to the *c-axis*. The current direction was in the plane of the film and perpendicular to the magnetic field in both measurements. The schematic configurations for the current direction and the magnetic field are illustrated in Fig. 5.6.

5.2.1 Temperature dependence of the activation energy

At higher temperatures it is found that the effective critical current density drops rapidly with temperature from the high values of J_c observed at low temperature. The decrease with temperature is much more pronounced in $Bi_2Sr_2CaCu_2O_y$ [152] than in $YBa_2Cu_3O_{7-\delta}$ [153]. This evidently is an effect of thermal activation. There is some characteristic activation energy U required to push a pancake vortex a certain distance a out of its pinning site. As the temperature T increases, the rate of its escape, which is proportional to $\exp(-U/k_BT)$, increases to the

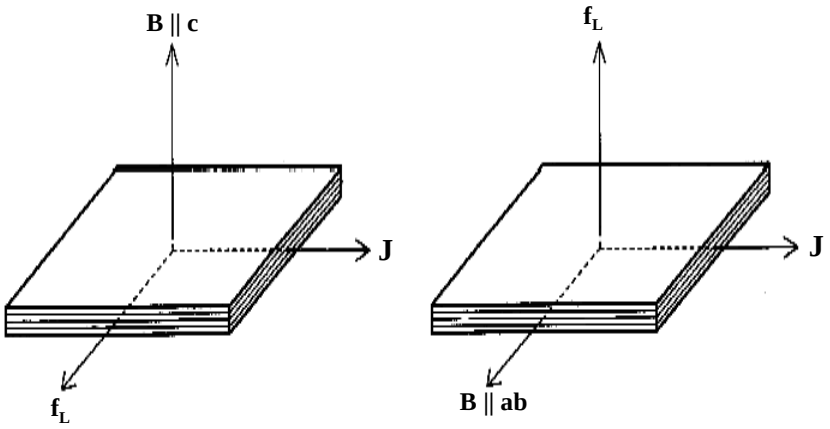

Figure 5.6: *Schematic configuration expressing the relation among J, B, and f_L for B perpendicular to the layer plane or $B||c$ (left) and parallel to the layer plane or $B||ab$ (right) and J is always in the layer plane.*

point that a typical vortex is no longer pinned on the time scale of the experiment. Usually, the broadening of the lower parts of the resistive transition, $\rho(T) < 10^{-2}$ ρ_n (where ρ_n is the resistivity in the normal state just above the transition), in a magnetic field for layered superconductors is interpreted in terms of a dissipation of energy caused by the motion of vortices [45]. This interpretation is based on the fact that for the low-resistance region, the resistance is caused by the creep of vortices. The activation energies U are obtained from a measurement of the resistivity ρ as a function of temperature and magnetic field using standard four point measurements. The TAFF concept is closely related to flux creep, and is found in the limit where the argument of the $\sinh(x)$ factor in Eq. (5.3) is small, i.e., where $\sinh(x) \sim x$. This gives an Ohmic resistivity. If the resistivity ρ has a thermally activated behavior, $\rho(T)$ can be expressed very generally as

$$\rho(T) \;=\; \rho_0 \;\exp\{-U(B,T,J)/k_BT\} \tag{5.4}$$

where ρ_0 is a coefficient associated to the normal resistance just above the transition, k_B is the Boltzmann constant and $U(B,T,J)$ being the activation energy which might depend on temperature, magnetic field, and current. In high-T_c materials, many factors such as short coherence lengths and high temperatures act together to decrease the magnitude of the exponent in Eq. (5.4). This gives rise to pronounced TAFF behavior and relatively high values of $\exp\{-U(B,T,J)/k_BT\}$.

In the limit of small driving currents $J \ll J_c$ the resistance is the result of a thermally activated process, U is current independent in the liquid, which has been explained as being due to the dominant contribution of plastic deformations [154]. The activation energy can be obtained from the slope of the linear parts of an Arrhenius plot (according to Eq. (5.4)) and ρ_0 is a field-independent pre-exponential factor. Let us first focus on the resistivity at low levels, $\rho/\rho_n < 0.1$. At such levels, thermally assisted flux flow is prevailing. The TAFF is characterized by an activation energy U_0 which is field and slightly temperature dependent. In order to determine the activation energy U of the present $(Hg_{0.9}Re_{0.1})Ba_2CaCu_2O_{6+\delta}$ thin film for different magnetic fields, the resistivity was represented in a set of Arrhenius plots as shown in Fig. 5.7. In this representation the slope of the line tangent in the low-resistance regime of the transitions is an approximation for the value of the activation energy U_0 at zero temperature. Two different dissipative regimes are clearly seen at $\rho \simeq 0.1$. Thermally assisted flux flow is found at low resistivities, while flux flow prevails at higher temperatures. The straight-line behavior over three orders of magnitude of the resistance indicates that the resistive behavior of the $(Hg_{0.9}Re_{0.1})Ba_2CaCu_2O_{6+\delta}$ film is caused by the TAFF-process as described by the Arrhenius law given in Eq. (5.4). The best fit of the experimental data $\rho(T)\mid_{B=const}$ by Eq. (5.4) yields values of the activation energy, ranging from $U/k_B = 5.75 \times 10^3\,\mathrm{K}$ to $U/k_B = 50.65 \times 10^3\,\mathrm{K}$ in a low magnetic field and from $0.69 \times 10^3\,\mathrm{K}$ to $12.43 \times 10^3\,\mathrm{K}$ in the high field region for magnetic field parallel and perpendicular to the c-axis, respectively.

A linear temperature dependence of Arrhenius plots implies that the activation energy is either constant or linearly temperature dependent. Since Eq.(5.4) with the activation energy is used to describe our experiments, the values of the activation energy should be deduced only from the limited temperature intervals below T_c, in which the data of the Arrhenius plot of $\rho(T)$ yield straight lines. Also, the activation energy can be obtained by inverting expression Eq. (5.4). This gives

$$U(T) = -k_B T \ln\left(\frac{\rho(T,B)}{\rho_0}\right) \tag{5.5}$$

The activation energy as a function of temperature $U(T)$ in the presence of a constant magnetic field parallel and perpendicular to the c-axis of a $(Hg_{0.9}Re_{0.1})Ba_2CaCu_2O_{6+\delta}$ epitaxial thin film is shown in Figs. 5.8-a and 5.8-b, respectively. For evaluation of Eq. (5.5) ρ_0 has been taken as the normal-state resistivity at $T=$

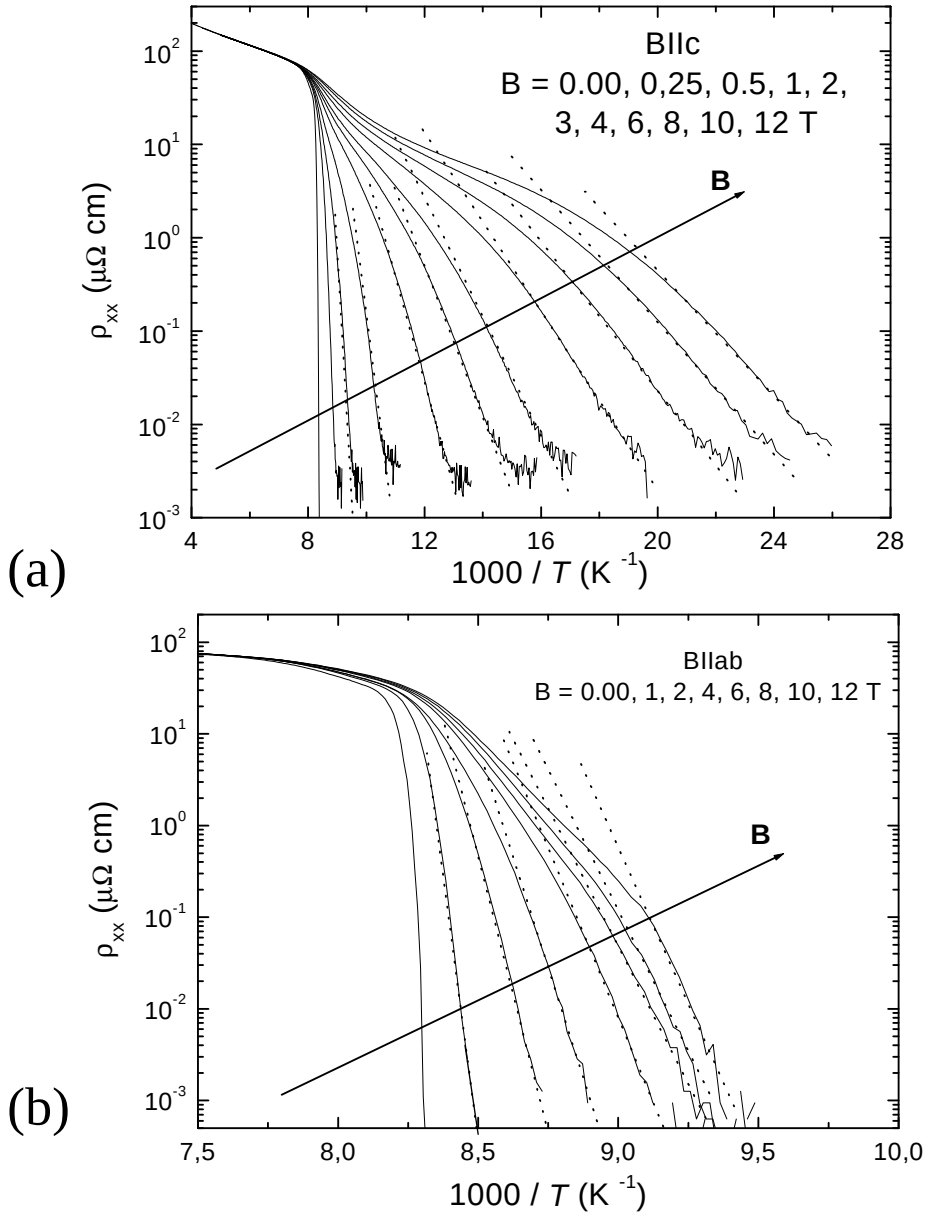

Figure 5.7: *Arrhenius plots of the resistive transitions in magnetic fields parallel (a) and perpendicular (b) to the c-axis. The dotted lines are linear fits for the low resistivity part of the transition.*

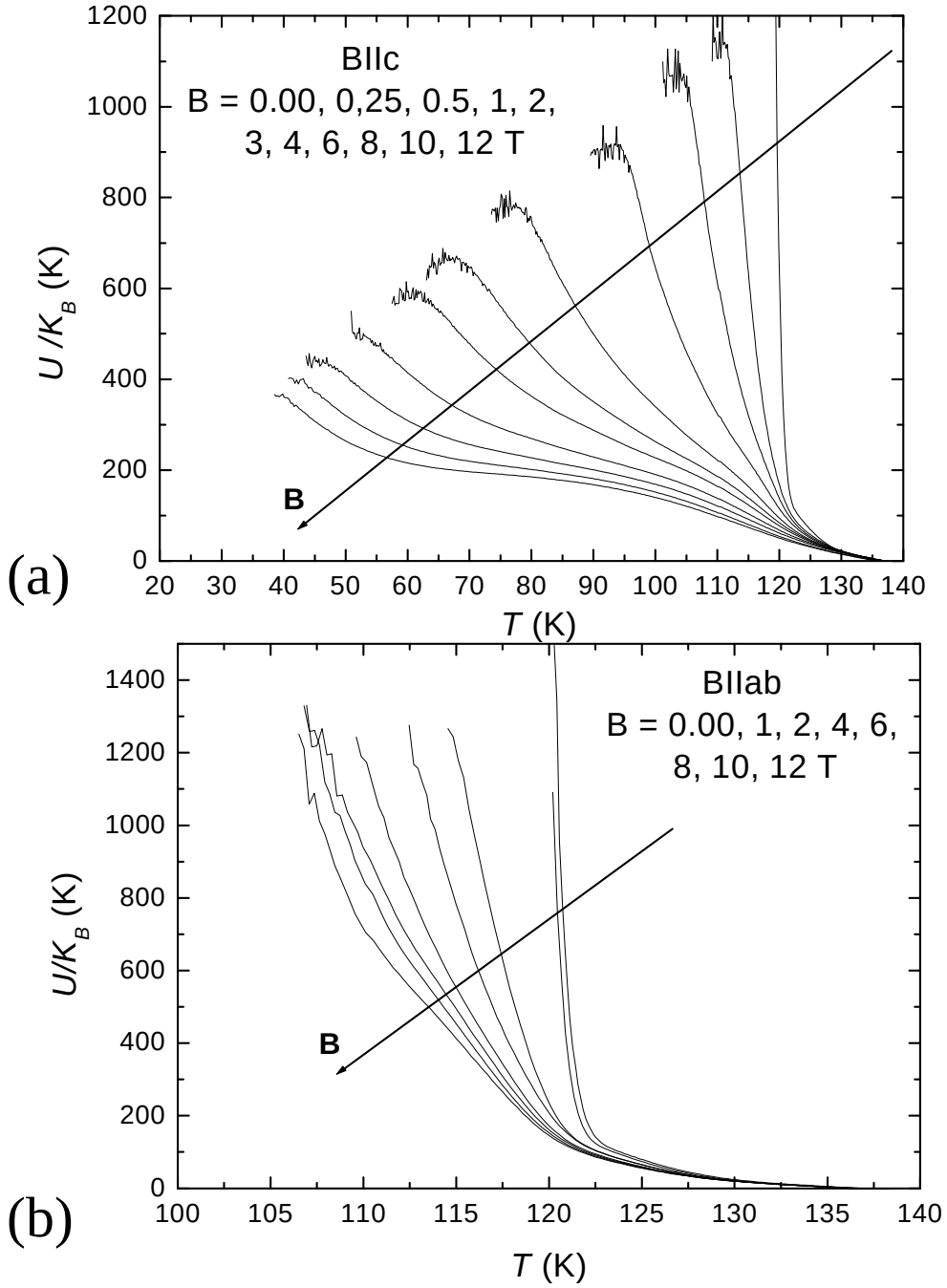

Figure 5.8: *Temperature dependence of the activation energy $U(T)$ determined from Eq. (5.5) for a HgRe1212 film as a function of the magnetic field up to 12 T parallel (a) and perpendicular (b) to the c-axis.*

135 K in zero field, i.e., just above the superconducting transition. This choice is physically reasonable and it enforces $U(T)$ to go to zero at $T \approx T_c$.

5.2.2 Magnetic field dependence of the activation energy

Investigations of high-T_c superconductors and artificial multilayers showed that the activation energy exhibits different power-law dependences on a magnetic field, $U(B) \propto \mathrm{B}^{-\alpha}$ with the exponent $\alpha \leq 1$ [45, 147, 155]. The result of the estimation of $U(B)$ from the slope of the low resistivity part of the Arrhenius plots is shown in Fig. 5.9.

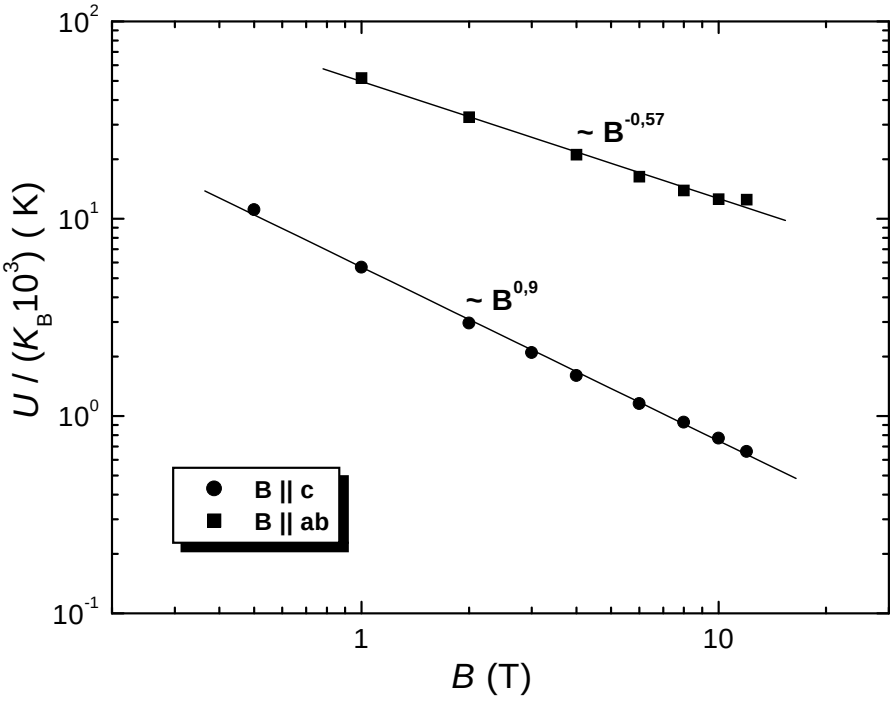

Figure 5.9: *Magnetic field dependence of the activation energy $U(B)$ determined from Eq. (5.5) for a $(Hg_{0.9}Re_{0.1})Ba_2CaCu_2O_{6+\delta}$ film shown in double logarithmic scale as a function of the magnetic field up to 12 T parallel and perpendicular to the c-axis.*

The activation energy is plotted as a function of the applied magnetic field on a double logarithmic scale in Fig. 5.9 for $B \parallel c$ and $B \perp c$ or $\parallel ab$. We find that the field dependence of the activation energy follows a power law $U(B) \propto 1/B^{\alpha}$ with $\alpha = 0.57$ for $B \perp c$, which could be ascribed to the plastic deformation of a flux

line solid creating the double kinks [154]. A similar result of the $1/\sqrt{B}$ dependence of $U(B)$ has been observed in highly c-axis-oriented Tl-2212 thin films [156] for $B \perp c$, in Bi-2223 thin films [157] for $B \parallel c$, and it has been demonstrated in detail in Bi-2212 thin films in $B \parallel c$ orientation [158]. Geshkenbein *et al.* [154] proposed thermally activated motion of vortices by plastic deformations as physical origin of the $1/\sqrt{B}$ dependence of $U(B)$. For $B \parallel c$ the value of α is 0.91. This value is close to the B^{-1} dependence observed in epitaxial YBCO thin films [159, 160] and crystals [161] in the same orientation. These results of the field dependence of $U(B)$ suggest that the mechanism of flux creep is similar in our $(Hg_{0.9}Re_{0.1})Ba_2CaCu_2O_{6+\delta}$ films and in YBCO. The B^{-1} dependence of $U(B)$ has been explained by the model of thermally activated vortex lattice shear proposed by Tinkham [148].

Figure 5.10-top shows the activation energy $U(B)$ as a function of the magnetic field parallel to the c-axis which is determined from the Arrhenius plots. For comparison, published data for HgO/Re-Ba-Ca-Cu-O multilayer precursor films [162], $YBa_2Cu_3O_{7-\delta}$ (Y-123), $(Tl,Bi)Sr_2Ca_2Cu_3O_x$ (Tl-1223) [163, 164], $Tl_2Ba_2Ca_2Cu_3O_x$ (Tl-2223) [165], $HgBa_2CaCu_2O_y$ (Hg-1212) [164], and $Bi_2Sr_2CaCu_2O_y$ (Bi-2212) [166] are also included in Fig. 5.10-top. It is known that the magnitude and the slope of U correlate with the pinning strength or the anisotropy of cuprate superconductors. $YBa_2Cu_3O_{7-\delta}$ with the smallest anisotropy exhibits the largest magnitude of U and a rather steep slope close to unity, while $Bi_2Sr_2CaCu_2O_y$ with the double-layer charge reservoir and the largest anisotropy shows the smallest U and a slope less than 0.5. The $U(B)$ line for the present $(Hg_{0.9}Re_{0.1})Ba_2CaCu_2O_{6+\delta}$ film is located near that for $HgBa_2CaCu_2O_y$ thin films [164] and $(Hg_{0.9}Re_{0.1})Ba_2Ca_2Cu_3O_y$ thin films [162], and between those for $YBa_2Cu_3O_{7-\delta}$ and $Bi_2Sr_2CaCu_2O_y$. The slope is much steeper than those for $(Tl,Bi)Sr_2Ca_2Cu_3O_y$ and $Bi_2Sr_2CaCu_2O_y$ and close to unity. These results seem consistent with our result of $(Hg_{0.9}Re_{0.1})Ba_2CaCu_2O_{6+\delta}$ thin films [167] and with the previous results [168] indicating that the mercury cuprates have a moderate anisotropy factor. The magnitude of U for a magnetic field parallel to the ab-axis or perpendicular to the c-axis indicated in the bottom of Fig. 5.10 is also comparable to those reported for undoped $HgBa_2CaCu_2O_y$, and doped $HgBa_2Ca_2Cu_3O_y$, while the magnitude of U is much higher than for $(Tl,Bi)Sr_2Ca_2Cu_3O_y$ thin films.

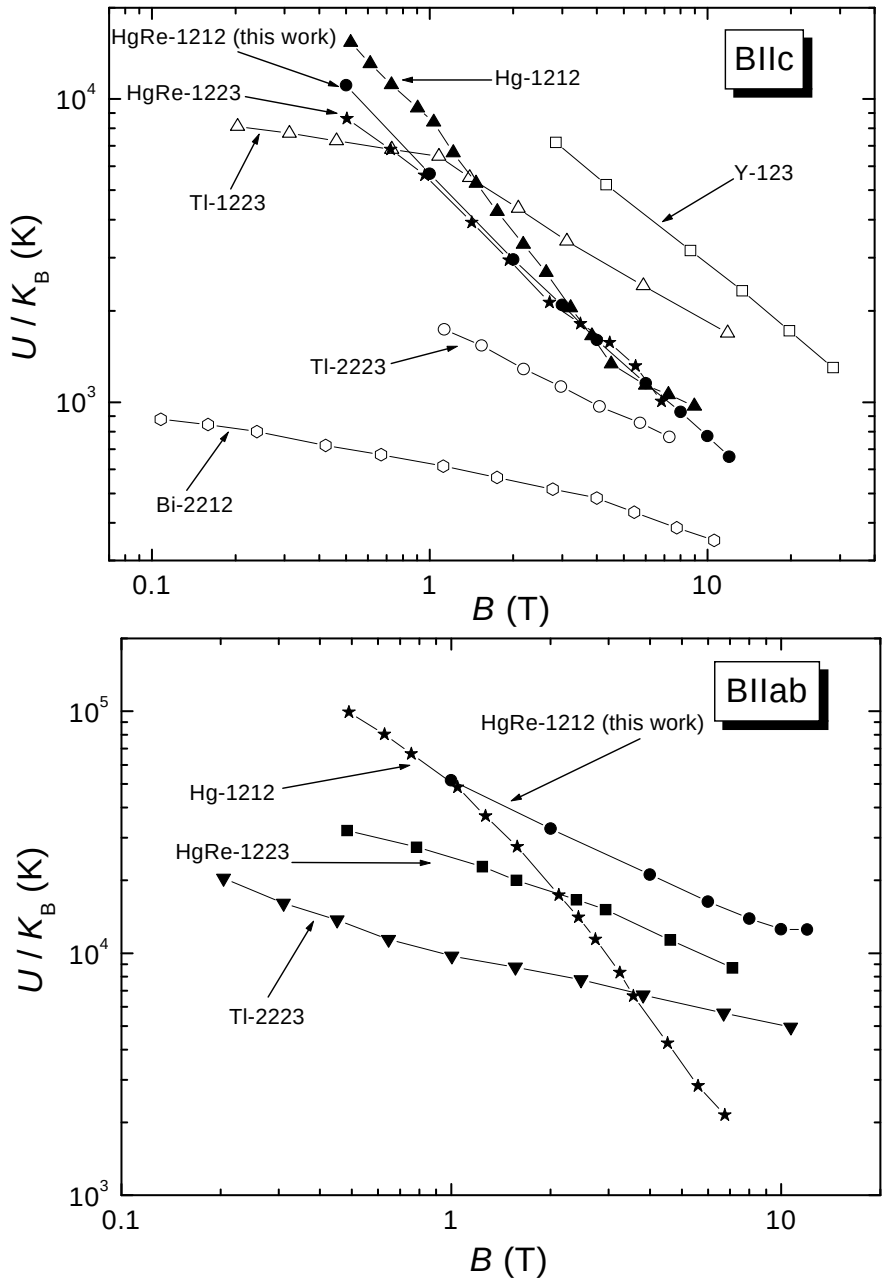

Figure 5.10: *Activation energy $U(B)$ for the present $(Hg_{0.9}Re_{0.1})Ba_2CaCu_2O_{6+\delta}$ thin films determined from the Arrhenius plots of the resistivity tails as a function of magnetic field parallel (top) and perpendicular (bottom) to the c-axis. The U values for other high T_c cuprate thin films are shown, for details of references see text.*

Chapter 6

Anisotropy of flux flow resistivity in $(Hg_{0.9}Re_{0.1})Ba_2CaCu_2O_{6+\delta}$ thin films

A common feature of high T_c-superconductors is the pronounced anisotropy of their physical properties due to their layered crystal structure. Superconductivity is basically confined to or governed by CuO_2 layers which are separated by metallic or insulating charge reservoirs. This leads to a significant anisotropy of the conductive properties and a reduction of the line energy of vortices. An alternating stacking of the CuO_2 layer and the blocking layer is a key concept both in crystal structure and in the occurrence of the superconductivity. This is also the origin of the intrinsic pinning for vortices parallel to the layers in high-T_c superconductors. The electrodynamic behaviour of the high-temperature cuprate superconductors is strongly affected by the anisotropy of these layered materials. Their transport, magnetic and pinning properties are determined by the properties of vortices, which for the most anisotropic materials can be regarded as stacks of two-dimensional (2D) pancake vortices with cores localized in the CuO_2 layers, bilayers or trilayers, connected by Josephson vortices with cores localized in the nonsuperconducting charge-reservoir layers. The transport properties for currents flowing parallel to the layers are dominated by 2D pancake vortex motion, while those for currents flowing perpendicular to the layers are dominated by Josephson vortex motion [169]. In the case of extremely strong anisotropy, a description of the vortices in terms of 2D pancake vortices with negligible interlayer coupling

should be valid. High-T_c oxide superconductors exhibit uniaxial anisotropy and their magnetic behavior can be described by two penetration depths, $\lambda_{ab} < \lambda_c$ for currents in the crystalline ab-plane or along the c-axis, respectively, and by two coherence lengths $\xi_{ab} > \xi_c$. On the fundamental side, the anisotropy gives rise to interesting physics and new phenomena. However, with respect to developing the high-temperature superconductors for applications, this anisotropy is the source of some difficult problems. In the absence of defects in the material (i.e. when there are no pinning centers present), most of the thermodynamic properties can be understood theoretically in terms of the anisotropic Ginzburg-Landau theory, which treats the superconductor as a continuum but with different properties along the three principal axes, characterized by dimensionless effective masses m_a, m_b, and m_c [169]. For the superconducting properties this anisotropy can be expressed in terms of an effective mass ratio for pair motion in the CuO_2 planes (ab) and along the c-axis. Its relation to the respective coherence lengths, penetration depths, and critical fields in the ab-plane and along the c-axis is given by:

$$\gamma = \sqrt{\frac{m_c}{m_{ab}}} = \frac{\xi_{ab}}{\xi_c} = \frac{\lambda_c}{\lambda_{ab}} = \frac{B_{c2}^{\perp c}}{B_{c2}^{\parallel c}} \,. \tag{6.1}$$

The degree of anisotropy varies enormously for the different types of high temperature superconductors (HTSCs). The value of γ is about 5 for $YBa_2Cu_3O_7$ and above 100 for the quasi-two dimensional $Bi_2Sr_2CaCu_2O_8$ compound. We will concentrate on $(Hg_{0.9}Re_{0.1})Ba_2CaCu_2O_{6+\delta}$ thin films as an example of HTSCs. In mercury-based $HgBa_2Ca_{n-1}Cu_nO_{2n+2+\delta}$ cuprates different values of the anisotropy of $HgBa_2CaCu_2O_{6+\delta}$ have been reported. Estimations of γ ($\gamma \simeq 4$ [170], $\gamma \simeq 5$ [171], and $\gamma \simeq 7.7$ [172]) were obtained from reversible magnetization measurements in grain-aligned $HgBa_2CaCu_2O_{6+\delta}$ samples. In grain-aligned $HgBa_2Ca_2Cu_3O_{8+\delta}$ samples with a different degree of alignment anisotropy values of $\gamma \simeq 2$ [173], $\gamma \simeq 4.4$ [170] and $\gamma \simeq 8$ [174] have been extracted from the ratio of physical quantities related to the effective mass, as measured parallel and perpendicular to the CuO_2 layers. Higher values of $\gamma \simeq 16$ were derived from vortex fluctuation analysis of the magnetization of randomly oriented polycrystalline $HgBa_2Ca_2Cu_3O_{8+\delta}$ samples [175]. From dc-magnetization measurements on early $HgBa_2CuO_{4+\delta}$ and $HgBa_2Ca_2Cu_3O_{8+\delta}$ superconducting single crystals, for fields applied both perpendicular and parallel to the CuO_2 layers, it is reported that

$\gamma \simeq 30$ for $HgBa_2CuO_{4+\delta}$ and $\gamma \simeq 50$ for $HgBa_2Ca_2Cu_3O_{8+\delta}$ [176]. Also angle-resolved torque measurements were used to extract a value of the anisotropy ratio $\gamma = 52$ for $HgBa_2Ca_3Cu_4O_{10}$ [177]. The higher values derived in the latter publications do not result from strong differences in the measured anisotropic properties but rather from the scaling ansatz used to extract the effective mass ratio [176].

To determine the scaling properties of the anisotropic magnetoresistance below T_c numerous data on the angular dependence of the magnetoresistance $R(B, \theta)$ are reported in the literature [178, 179, 180, 181, 182, 183, 184, 185] and reveal the strong dependence of $R(B, \theta)$ on the field direction with respect to the crystallographic axes. The present chapter presents the experimental results of anisotropy of flux flow resistivity in $(Hg_{0.9}Re_{0.1})Ba_2CaCu_2O_{6+\delta}$ thin films (which have been published in 2004 [167]). In order to estimate the anisotropy of $(Hg_{0.9}Re_{0.1})Ba_2CaCu_2O_{6+\delta}$ films the angular dependence of the depinning field for thermally activated flux motion $B_{dp}(\theta)$ was measured, with θ being the angle between c-axis and external field.

The measurements of the depinning field $B_{dp}(T, \theta)$ were carried out using a $R(T, B_{dp}) = 0.1R_n$ criterion. The temperature and the current value were fixed while the angle was varied and the magnetic field was changed until the voltage corresponding to the applied criterion was detected. In order to change the orientation of the film in relation to an applied field the film was mounted onto a rotatable copper block driven by a wormgear (Fig. 6.1). Using this experimental setup an angular resolution of 0.1° can be achieved. The rotatable copper block also includes a heater and Pt and CGR resistive thermometers to ensure good thermal contact between film and thermometers. The films were mounted to the copper block with the direction of the applied current parallel to the axis of block rotation so that current and applied field were always perpendicular.

The typical angular dependence of the depinning field as obtained from our measurements at temperature T= 105 K is shown in Fig. 6.2. The observed angular dependence can be interpreted by a flux flow analysis. In the region of our applied criterion $R(T, B_{dp}) = 0.1R_n$, the V-I characteristics show ohmic (i.e. linear) behavior, i.e. the dissipation process is dominated by thermally activated flux-motion. In the framework of the Bardeen-Stephen model the dissipation in the flux flow region is proportional to the ratio between the applied field and the

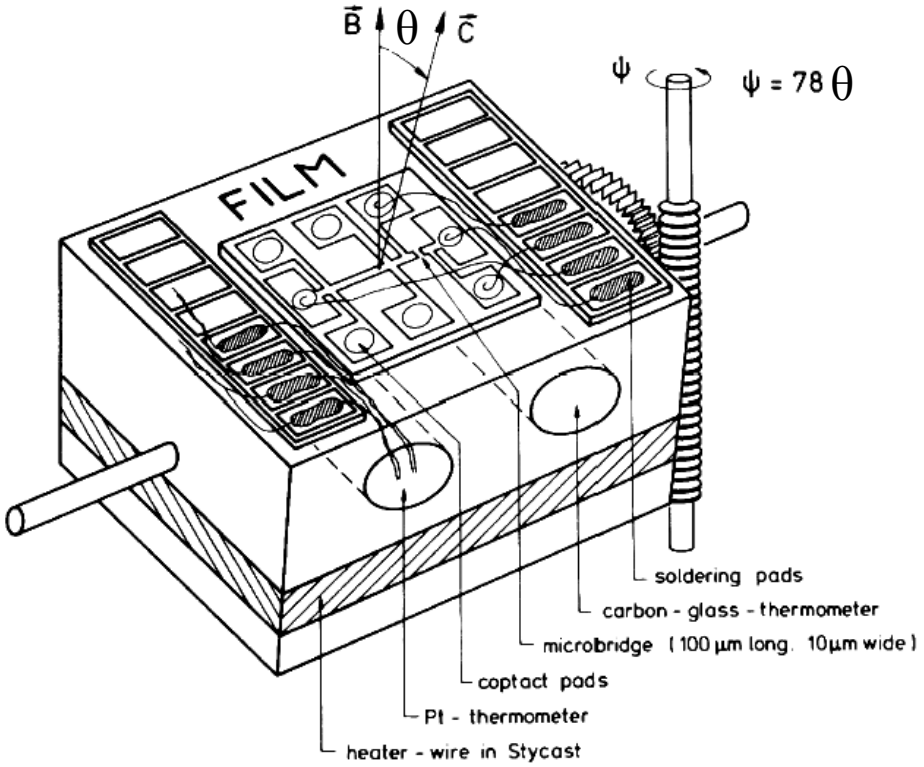

Figure 6.1: *Experimental setup to change the orientations of the film relative to the applied field.*

upper critical field [186]. Assuming that this proportionality holds the measurements of the depinning field for parallel and perpendicular orientation will reflect the anisotropy of the critical fields.

The anisotropic Ginzburg-Landau theory is an extension of the theory to an anisotropic crystal structure, introducing an effective electron mass tensor [187]. The mass tensor is diagonal in crystal based coordinates ($\mathbf{e}_a$,$\mathbf{e}_b$,$\mathbf{e}_c$). The reciprocal form used in the Ginzburg-Landau equations is

$$\widehat{\mathbf{m}}^{-1} = \begin{pmatrix} m_a^{-1} & 0 & 0 \\ 0 & m_b^{-1} & 0 \\ 0 & 0 & m_c^{-1} \end{pmatrix}. \tag{6.2}$$

If we want to calculate more easily in the laboratory based coordinates ($\mathbf{e}_x$,$\mathbf{e}_y$,$\mathbf{e}_z$) with the magnetic field B in z-direction, we have to rotate the mass tensor to fit

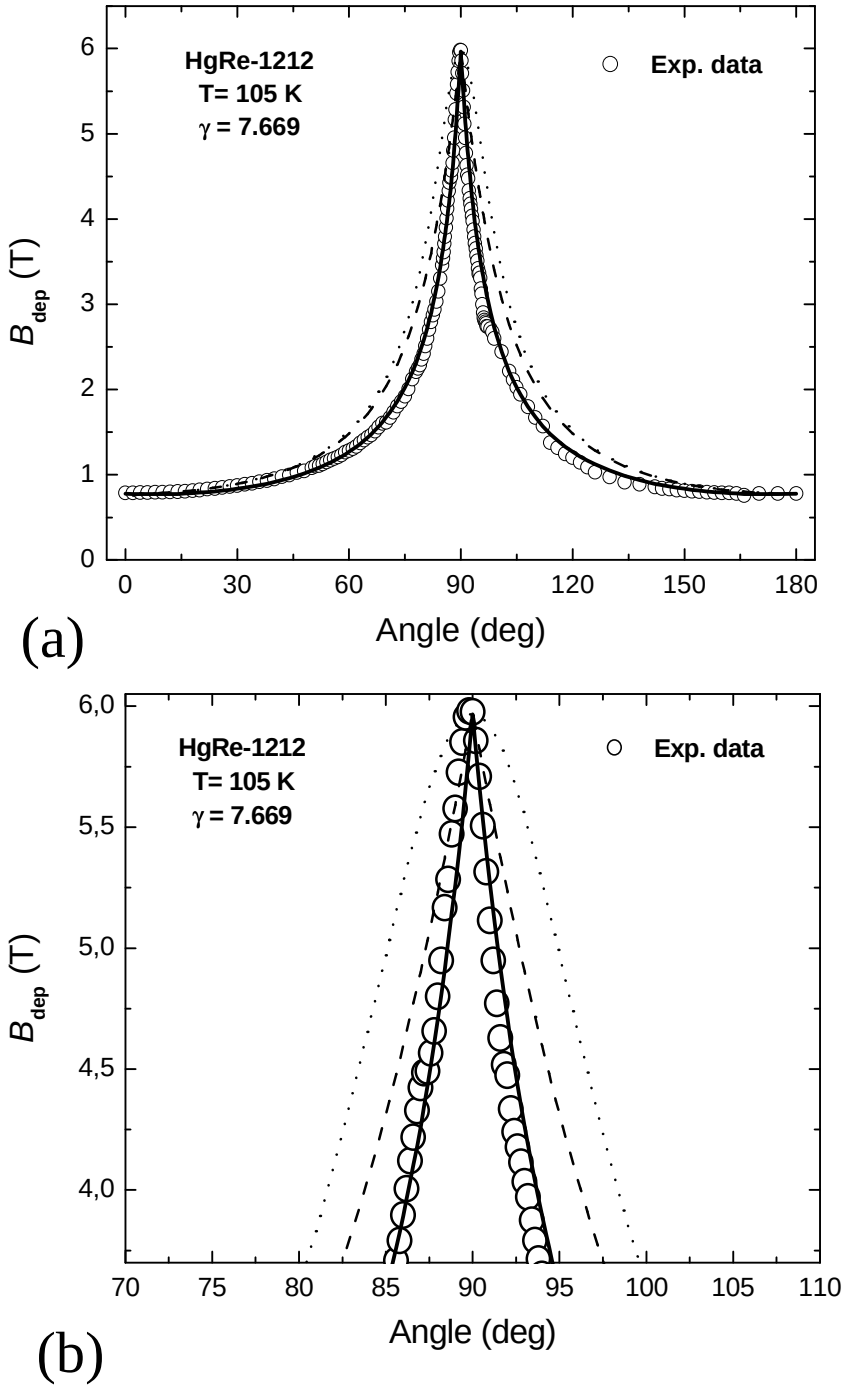

Figure 6.2: *Typical angular dependence of the depinning field B_{dp} obtained from flux flow resistivity measurements at the temperature T= 105 K. The bottom shows the region close to B parallel to the planes (90°) in an expanded scale. The solid line is a fit according to the decomposition assumption (6.21), the dashed line is a fit according to the 2D model of Tinkham (6.17), and the doted line is a fit using the anisotropic effective mass model (6.8).*

the preferred coordinates. This is done by two successive rotations first around the x-axis with

$$\widehat{\mathbf{T}}_x = \begin{pmatrix} \cos\varphi & \sin\varphi & 0 \\ -\sin\varphi & \cos\varphi & 0 \\ 0 & 0 & 1 \end{pmatrix} \tag{6.3}$$

and second around the z-axis with a similar structured tensor

$$\widehat{\mathbf{T}}_z = \begin{pmatrix} \cos\theta & \sin\theta & 0 \\ -\sin\theta & \cos\theta & 0 \\ 0 & 0 & 1 \end{pmatrix} \tag{6.4}$$

so that the mass tensor writes as $\widehat{\mathbf{m}}^{-1}|_{xyz} = (\widehat{\mathbf{T}}_z\widehat{\mathbf{T}}_x)^{-1}\widehat{\mathbf{m}}^{-1}|_{abc}(\widehat{\mathbf{T}}_z\widehat{\mathbf{T}}_x)$, following the tensor transformation rules. $(Hg_{0.9}Re_{0.1})Ba_2CaCu_2O_{6+\delta}$ is supposed to be isotropic in two of the three axes because of the small differences in the a- and b-plane. This leads to $m_{ab} \equiv m_a = m_b \neq m_c$ and therefore φ can be chosen to be zero. The mass tensor now gets in detail

$$\widehat{\mathbf{m}}^{-1} = \begin{pmatrix} m_{ab}^{-1} & 0 & 0 \\ 0 & m_{ab}^{-1}\cos^2\theta + m_c^{-1}\sin^2\theta & m_{ab}^{-1}\sin\theta\cos\theta - m_c^{-1}\sin\theta\cos\theta \\ 0 & -m_{ab}^{-1}\sin\theta\cos\theta + m_c^{-1}\sin\theta\cos\theta & m_{ab}^{-1}\sin^2\theta + m_c^{-1}\cos^2\theta \end{pmatrix}. \tag{6.5}$$

Inserting this expression for the mass in the GL equations and choosing the vector potential $\mathbf{A} = -B_{0y}\mathbf{e}_x$ they turn to

$$-\frac{1}{4}\left(m_{ab}^{-1}\cos^2\theta + m_c^{-1}\sin^2\theta\right)\hbar^2\partial_y^2\Psi + \frac{e^2}{m_{ab}}B_0^2y^2\Psi = |\alpha|\Psi \tag{6.6}$$

where the derivatives of Ψ in the directions x and z are zero and terms above linear power were neglected because B is near to B_{c2}. The nontrivial solution for the upper critical field B_{c2} is given as

$$B_{c2}(\theta) = \frac{\varphi_0}{2\pi\xi_{ab}^2}\frac{B_{c2}^{\|c}}{\sqrt{\cos^2\theta + \gamma^{-2}\sin^2\theta}} \quad . \tag{6.7}$$

For the special case of $B \,||\, \mathbf{e}_c$, i.e., $\mathbf{e}_c = \mathbf{e}_z$, then $B_{c2} = B_{c2}^{||c} = \varphi_0/2\pi\xi_{ab}^2$ with the substitution $\xi_{ab}^2 = \hbar/\sqrt{2m_{ab}|\alpha|}$. The angular dependence of the critical field $B_{c2}(\theta)$ according to the anisotropic Ginzburg-Landau theory is given by:

$$B_{c2}(\theta) = \frac{B_{c2}^{\|c}}{\sqrt{\cos^2\theta + \gamma^{-2}\sin^2\theta}} \tag{6.8}$$

This equation also follows from the scaling ansatz used by Blatter for the description of anisotropic 3-dimensional systems [188]. The consequences for anisotropic behaviour of 3D systems are an angular dependence of the critical field. In addition to that a direction dependency of the London penetration depth occurs. Under the condition of different effective masses of the charge carriers an external field which is oriented by an angle θ relative to the ab-plane can be rescaled to the influence of a scaling field on an isotropic superconductor. The requirement for the anisotropic Ginzburg-Landau theory is that the magnetic field is homogeneous for the relevant length scales. This requires that the superconductor is either strong of type II ($\kappa = \frac{\lambda(T)}{\xi(T)} \gg 1$) or that a strong magnetic field is applied (inter vortices distance $a \leq \lambda$). Both conditions are fulfilled in the above experiment, the validity of the Ginzburg-Landau theory is not necessary for their model. In a homogenous anisotropic system the angular dependence of the depinning field $B_{dp}(\theta)$ thus also should follow Eq. (6.8), this curve is drawn as a dotted line in Fig. 6.2. However, large deviations occur for $\theta = 90^o$. Near $\theta = 90^o$ we observe a cusp like structure and not a smooth curve, as the curve of the scaling behavior shows a rounding, whereas the experiment exhibits a peak in this orientation of the magnetic field. Such a cusp like behavior is also expected for thin films, where a peak is characteristic for the anisotropic behavior of thin films even if the material itself is isotropic. If the thickness of the film is smaller than the penetration depth of the magnetic field then screening currents for the component of the magnetic field parallel to the surface of the film cannot be fully created. Therefore, the kinetic energy of the superconducting screening currents is smaller in this orientation of the field and superconductivity is possible for higher magnetic fields. Thus, an angular dependence of the upper critical field occurs even for isotropic systems.

In 1964 Tinkham [145] produced a simple physical argument for the angle dependence of B_{c2} in thin films. Let the film plane be the ab-plane and the magnetic field makes an angle θ with the normal to the film. If then the thickness of the film is small enough, the currents induced by the component of the magnetic field parallel ab are given by

$$\mathbf{J} \propto \nabla \times \mathbf{B} \simeq \frac{1}{\lambda} B|_{ab} e^{-\frac{d}{\lambda}} \simeq \frac{1}{\lambda} B|_{ab} \tag{6.9}$$

where the last step assumes $d \ll \lambda$. In this case one gets

$$J \propto B_0 \sin\theta \cdot \tag{6.10}$$

The kinetic energy corresponding to this contribution is

$$\mathrm{E}_1 \propto J^2 \Rightarrow \mathrm{E}_1 = \mathrm{A}_1 \cdot B_0^2 \sin^2\theta \tag{6.11}$$

The magnetic field B parallel to $\mathbf{e}_z$ forms flux lines that on average occupy the area $\pi R^2 \propto \frac{\varphi_0}{B_{\|c}}$. The corresponding current is

$$J \propto \frac{e\varphi_0}{R\lambda^2} \propto \sqrt{B_{\|c}} \cdot \tag{6.12}$$

This yields the following contribution to the kinetic energy:

$$\mathrm{E}_2 = \mathrm{A}_2 \cdot B_0 \cos\theta \cdot \tag{6.13}$$

As the components of the current are orthogonal, one can simply add the corresponding energies. At the upper critical field this sum should be the same for all directions θ (this fixes the transition). One obtains

$$\mathrm{E} = \mathrm{const} = \mathrm{A}_1 \cdot B_{c2}^2(\theta) \sin^2\theta + \mathrm{A}_2 \cdot B_{c2}(\theta) \cos\theta \cdot \tag{6.14}$$

Both constants in (6.14) can be expressed via the corresponding critical fields: If B $\|$ e$_c$, i.e., θ=0, then from Eq. (6.14) follows

$$\mathrm{A}_2 = \frac{\mathrm{const}}{B_{c2\|c}} \cdot \tag{6.15}$$

If, however, B $\perp$ e$_c$, i.e., $\theta = \frac{\pi}{2}$, then from Eq. (6.14) follows

$$\mathrm{A}_1 = \frac{\mathrm{const}}{B_{c2\perp c}^2} \cdot \tag{6.16}$$

In this case the anisotropy of the upper critical field is determined by the solution of the implicit equation:

$$\left(\frac{B_{c2}(\theta)}{B_{c2}^{\perp c}}\right)^2 \sin^2\theta + \left(\frac{B_{c2}(\theta)}{B_{c2}^{\|c}}\right) |\cos\theta| = 1 \tag{6.17}$$

which is derived for the critical field of 2D superconducting thin films in the classical text of Tinkham [145]. Both $B_{c2}^{\perp c}$ and $B_{c2}^{\|c}$ are fit parameters. In Fig. 6.2

the dashed line is a fit according to the 2D model of Tinkham (6.17). Although this two dimensional behavior yields a cusp it cannot describe the full angular dependence as the experimental peak structure is significantly sharper. There is a peak at $\theta = 90^o$, but significant deviations appear at the edges. Additionally, Eq. (6.17) only holds if the coherence length $\xi(T)$ exceeds $2d$, where d is the film thickness. This constraint applies for HTSC-films of more than 1000 Å thickness extremely close to the critical temperature only. Therefore, the application of this formula generally is not justified to explain the measured data. Recently Mineev has generalized the anisotropic Ginzburg-Landau ansatz to the thin film case [189]. His solution provides a smooth crossover between the two cases discussed before and is therefore also not able to explain the measured data in this work.

In the models above, systems were supposed with a homogeneous interior structure despite their anisotropy. In other words, the above formulas, ignore the layered structure of the high temperature superconductors (HTSCs). A flux tube crosses the sample in these models always as a straight line. The anisotropy simply causes that the direction of the flux tube does not need to be identical with the direction of the external magnetic field [190] and that the cross-section through the core of a flux tube results not in a circle but in an ellipse [191]. Tachiki and Takahashi, however, demanded that a flux tube interacts directly with the layer structure of the HTSCs. The flux tube minimizes the loss of the condensation energy by using the spatial modulation of the order parameter across the c-axis direction, which occurs due to the short coherence length in this direction [192]. The flux tube pentrates the superconductor thus not as a straight line but tries to arrange its core between the CuO_2 double-layer. This results therefore in the step structure of the flux line shown in Fig. 6.3. The authors used this step structure to explain the angular dependence of the critical current density of $YBa_2Cu_3O_{7-\delta}$ [193]. The flux density component $B_\parallel$, where $B_\parallel = B \sin\theta$, easily penetrates between the layers. In the simplest model describing the flux flow resistivity in the mixed state of a type-II superconductor, each vortex is assigned a normal core with its radius given by the coherence length ξ and its electric resistivity equal to the normal-state resistivity ρ_n near T_c. Since the volume fraction occupied by the normal cores of the vortex structure is about B/B_{c2}, from this picture we expect for the flux flow resistivity the relation

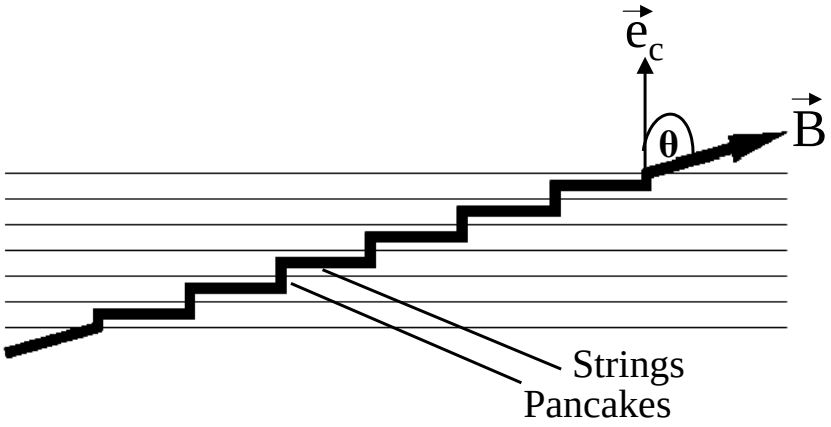

Figure 6.3: *Schematic representation of the step structure of a flux line. The horizontal lines represent the CuO_2 double-layers.*

$$\rho(T,B) = \frac{B}{B_{c2}}\rho_n(T). \tag{6.18}$$

ρ_n denotes the normal resistivity, which in this case is equal to the core resistivity.

If one assumes that for a magnetic field direction not parallel to the *ab*-plane the flux lines penetrate the superconductor in a step-like fashion and essentially decompose into two flux line lattices parallel and perpendicular to the superconducting planes the resistance induced by the magnetic field in the superconducting state was interpreted as continuous flow of flux tubes by Stephen and Bardeen. For $T \ll T_c$ the result of Eq. (6.18) of this flux flow-resistance in the Stephen-Bardeen model shows the dependence on the strength of the magnetic field [186] as follows:

$$\rho(T,B) = \frac{B}{B_{c2}} f(T/T_c)\rho_n(T) \tag{6.19}$$

If one assumes that the flux tube exhibits a step structure and that Eq. (6.19) is valid for the components of the magnetic field parallel ($\cos\theta$) and perpendicular ($\sin\theta$) to the *c*-axis, one gets for the flux flow resistance

$$\rho(T,B,\theta) = \left(\frac{B_{dp}|\cos\theta|}{B_{c2}^{\|c}} + \frac{B_{dp}|\sin\theta|}{B_{c2}^{\perp c}} \right) f(T/T_c)\rho_n(T) \tag{6.20}$$

where $f(T/T_c)$ is a function which absorbs all the temperature dependencies [194]. As in the experiment temperature and flux flow resistance are kept constant, one gets for the angular dependence of the depinning field in this model simply

$$B_{dp}(\theta) = \frac{B_{dp}^{\|c}}{|\cos\theta| + \gamma^{-1}|\sin\theta|}. \tag{6.21}$$

A perfect description of the data is obtained with $\gamma = 7.7$ at 105 K. This model is shown as a solid line in Fig. 6.2 and yields an excellent agreement with the data. However, the minimum of Eq. (6.21) is located at $\theta \neq 0^o$. This unphysical behavior or this disagreement is resolved by the fact that the decomposition of the flux line lattice, the independent treatment of the segments of the flux lines parallel and perpendicular to the layer structure, obviously is not valid in the full angular range. The reason for that is that one has to consider not only the core region of the flux line, where the order parameter disappears. The penetration length λ, on which the screening currents around a vortex center decay, is much larger than the coherence length ξ. Because of that the distribution of currents around a vortex cannot be determined by the same small length scale of the step structure. For small angles θ one can thus expect a straight flux line [195]. However, it becomes clear from the good agreement of Eq. (6.21) with the experimental data that the step structure of flux lines should be explicitly taken into account in the theoretical model. For angles below $\theta \approx 45^o$ the anisotropic Ginzburg-Landau theory is better suited. The cusp like structure at $\theta = 90^o$, however, is best reproduced by the decomposition assumption and yields an anisotropy value of $\gamma = 7.7$ at 105 K. The bottom of Fig. 6.2 shows the data close to 90° in an expanded scale. The small angular spread of the c-axis orientation and the angular resolution ($\Delta\theta \approx 0.1\,^\circ$) have a negligible influence on the determination of the anisotropy value. As in the magnetization measurements on grain aligned samples [170, 171, 172] we find a comparably low value of the anisotropy. Higher values of the intrinsic anisotropy are found if vortex-fluctuations are accounted for [175, 176, 177]. Of course, our analysis also neglects vortex fluctuations and assumes that the density of the pancake vortices is only given by the normal component of the applied magnetic field. On the other hand this way of determining the anisotropy yields an effective anisotropy of the material relevant for estimations of the useful range in the T-B-θ phase space of the material.

Chapter 7

Irreversibility line and critical current density

Magnetization measurements have played a crucial role in the development and understanding of the superconducting state [196, 197, 198, 199, 200]. From the viewpoint of technological implications, the magnetic properties of high-T_c superconductors are very important. Information on the field and temperature dependence of both the critical current density J_c and the flux-pinning force F_p can be obtained from magnetic hysteresis loops measured at different temperatures [43, 143, 196, 197, 198, 199, 200, 201, 202]. Moreover, the irreversibility line (IL) $B_{irr}(T)$, which is an important phenomenological feature of the high-temperature superconductors (HTSCs), can be obtained. This line divides the B-T phase diagram into two parts; above the IL, the magnetization of the HTSC sample is fully reversible and the vortices are free to move, whereas below the IL hysteretic magnetization occurs and the magnetic flux is pinned [201]. The standard interpretation of the IL is the onset of bulk pinning. At low temperature the vortices are pinned and hence a finite critical current is observed, whereas above the IL the vortices are unpinned.

For practical applications, a high critical current density J_c in a magnetic field and a high irreversibility field B_{irr} are required. In most high-T_c superconductors, however, J_c in a magnetic field decreases rapidly with increasing temperature due to dimensional crossover in vortex structure from three-dimensional (3D) to quasi two-dimensional (2D) [203, 204]. Therfore many efforts have been made to increase J_c and it is indispensable for that purpose to find out J_c-determining

factors by comparing various high-T_c superconductors. The present chapter consists of two parts of results, namely for the irreversibility line and for the critical current density in the $(Hg_{0.9}Re_{0.1})Ba_2CaCu_2O_{6+\delta}$ thin films. Magnetoresistivity and magnetization measurements for the $(Hg_{0.9}Re_{0.1})Ba_2CaCu_2O_{6+\delta}$ HTSC thin films have been carried out to evaluate their $J_c(B,T)$ and $B_{irr}(T)$. The result on the irreversibility line is compared with published data for other high T_c cuprates such as Y-123, Hg-12(n-1)n, Tl-12(n-1), Bi-12(n-1)n, etc.

7.1 Irreversibility line of $(Hg_{0.9}Re_{0.1})Ba_2CaCu_2O_{6+\delta}$ HTSC thin films

The phase boundary in the magnetic-field strength and temperature ($B-T$) plane, i.e., the irreversibility line, which separates the irreversible region from the reversible region in the $B-T$ phase space, as shown in Fig. 7.1, has been intensively studied. Numerous experiments on high- and low-T_c, superconductors have revealed the presence of irreversibility lines. From the point of view of applications, the $B_{irr}(T)$ marks the boundary between finite and zero J_c and is an important parameter to assess the in-field performance of high temperature superconductors. It has been found that, in general, when the temperature is close to T_c, i.e., in the low $B_{irr}(T)$ region, the irreversibility lines for HTSCs approximately follows a power-law relationship [205, 206, 207],

$$B_{irr}(T) = A\left(1-\frac{T}{T_c}\right)^n, \tag{7.1}$$

where A is a proportionality constant. The obtained values for the exponent n are dependent on the transition mechanisms from irreversible to reversible magnetization and vary from 1.3 to 5.5 [173, 208, 209, 210, 211]. The exponent n is 2.5 for Hg-Ba-Ca-Cu-O, 1.5 for Y-Ba-Cu-O, 5.5 for both Bi-Sr-Ca-Cu-O and Tl-Ba-Ca-Cu-O families. Many theoretical models [173, 208, 209, 210, 211, 212, 213, 214] have been proposed to explain the $B_{irr}(T)$ in HTSCs and to explain different n values of this power-law relationship. They include a flux-line (vortex) lattice melting model that requires $n=2$ and a vortex-glass transition model that calls for $n=3/2$. Other models, e.g., thermal depinning or vortex creep, give other n values. Experimental data seem to suggest that the nature of $B_{irr}(T)$ depends

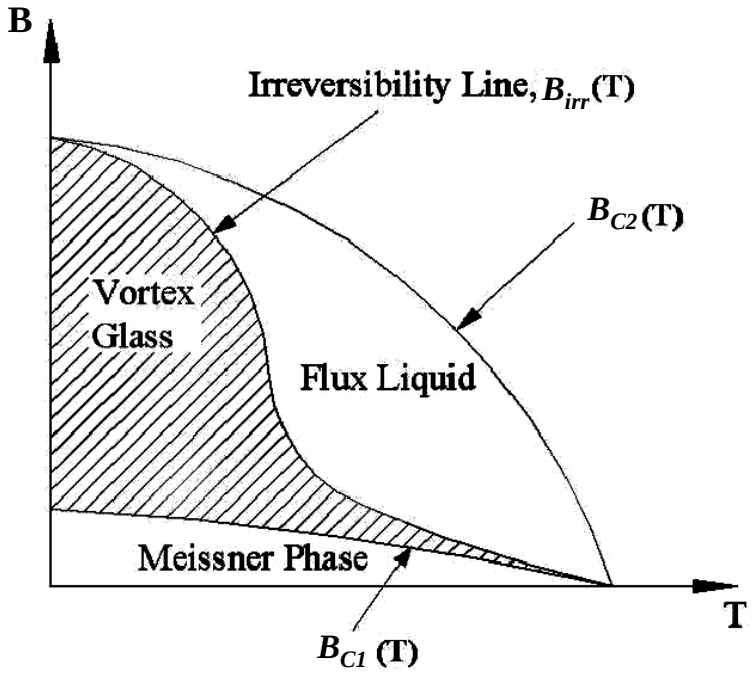

Figure 7.1: *Simplified phase diagram for HTSCs showing the vortex glass and flux liquid separated by the irreversibility line, $B_{irr}(T)$ [40].*

on the anisotropy of the superconductors. The functional dependence of $B_{irr}(T)$ near T_c is rather different between the two extremes of strongly coupled layered $YBa_2Cu_3O_{7-\delta}$ and loosely coupled layered $Bi_2Sr_2CaCu_2O_{8+\delta}$. $HgBa_2CaCu_2O_y$, with moderate CuO_2-block separation, lies between these extremes and serves as an excellent subject for further study of the nature of the irreversibility field $B_{irr}(T)$.

The irreversibility line can be measured by several methods. In this investigation, resistivity measurements versus temperature were applied in dc magnetic fields up to 12 T parallel to the *c*-axis. The temperature dependence of the resistivity is shown in Fig. 7.2 in the presence of different values of the magnetic field. In zero magnetic field the transition is sharp, whereas in the presence of the magnetic field the resistive transition shows a remarkable broadening, which has been discussed in chapter 5. The resistive transition behavior in a magnetic field can be used to determine the temperature dependence of the irreversibility line $B_{irr}(T)$ in the parallel orientation. The irreversibility line $B_{irr}(T) = \mu_0 H_{irr}(T)$

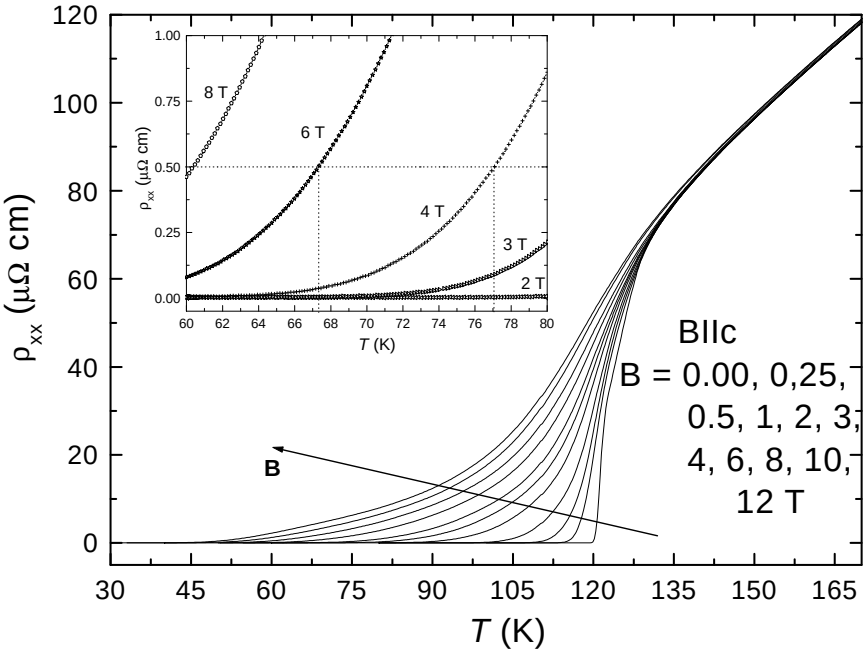

Figure 7.2: *Temperature dependence of the electrical resistivity for a* $(Hg_{0.9}Re_{0.1})Ba_2CaCu_2O_{6+\delta}$ *film in various magnetic fields up to 12 T oriented parallel to the c-axis. In the inset the resistivity axis is magnified for the determination of the irreversible temperature* $T_{irr}(B)$.

for the magnetic field parallel to the c-axis of $(Hg_{0.9}Re_{0.1})Ba_2CaCu_2O_{6+\delta}$ obtained from our measurement is plotted in Fig. 7.3. The upper-limit criterion for the determination of the irreversible temperature $T_{irr}(B)$ was 0.5 $\mu\Omega$cm (see in the inset of Fig. 7.2). This usually serves as the definition of the irreversibility line, and provides a contour line in the $B(T)$ plane. This line divides the B-T phase diagram in two regions of irreversible (low B, T) and reversible magnetic behavior. Above this line loss free current transport is not possible due to flux motion. In this region of the B-T phase diagram the superconducting material is not useful for technical applications. Clearly, the position of the irreversibility line in the $B(T)$ plane depends on the chosen criteria. For a proper, systematic comparison of the irreversibility line for different high T_c materials, the same electrical resistivity criterion and the same current density for the measurement need to be applied.

In order to compare the present results with those of other high-T_c cuprates

, published data for HgO/Re-Ba-Ca-Cu-O multilayer precursor films [162, 215], [$YBa_2Cu_3O_{7-\delta}$ (Y-123), (Tl,Bi)$Sr_2Ca_2Cu_3O_x$ (Tl-1223)] [163, 164], $Tl_2Ba_2Ca_2Cu_3O_x$ (Tl-2223) [165], and $Bi_2Sr_2CaCu_2O_x$ (Bi-2212) [166] are also included in Fig. 7.3. The irreversibility line for the $(Hg_{0.9}Re_{0.1})Ba_2CaCu_2O_{6+\delta}$ films is observed to be at higher magnetic fields than that for Bi-2212 and Tl-2223, but at lower fields than that of Y-123 and Tl-1223 thin films at the same reduced temperatures. Although mercury free precursors were used in the preparation method for this thesis the irreversibility line is indeed nearly identical to that of HgO/precursor multilayers [162, 215]. It should be noted that, because of its high T_c value, the irreversibility field B_{irr} at about 77 K for the $(Hg_{0.9}Re_{0.1})Ba_2CaCu_2O_{6+\delta}$ is as high as 4 T, as seen in the top of Fig. 7.3. This value is slightly higher than those for HgRe-1212 (HgO/Re-Ba-Ca-Cu-O multilayer precursor films) [162] and Tl-1223 [164], and substantially higher than those for Tl-2223 [165] and (Bi-2212) [166], demonstrating the large potential of the $(Hg_{0.9}Re_{0.1})Ba_2CaCu_2O_{6+\delta}$ for use in high fields especially at temperatures above 77 K. The irreversibility line for the present Re-doped Hg-1212 thin films also seem to be substantially higher than the values (< 2 T at 77 K) reported for undoped ceramics [216] and even c-axis thin films prepared by sputtering and a two-step process [217]. However, it is still not clear whether the higher $B_{irr}(T)$ comes from the Re-doping itself or the improvement in the film morphology. For the Re-doped mercury based cuprate ceramics, it was reported that the substitution of Re for the mercury-site enhances the conductivity of the charge reservoir block and decreases the anisotropy factor [218], leading to the increase in $B_{irr}(T)$. It should be also noted that the crystallinity of the present $(Hg_{0.9}Re_{0.1})Ba_2CaCu_2O_{6+\delta}$ thin films is as good as those of HgO/Re-Ba-Ca-Cu-O multilayer precursor films [162, 215]. The FWHM value of X-ray rocking curves for the present $(Hg_{0.9}Re_{0.1})Ba_2CaCu_2O_{6+\delta}$ films is typically 0.32° which is much smaller than the value ($\approx 1.0^\circ$) for the HgO/Re-Ba-Ca-Cu-O multilayer precursor films [162, 215]. This means that a larger B_{irr} value has been obtained by improving the crystallinity of the films.

Flux dynamics depends strongly on anisotropy which, in turn, depends on the coupling between CuO_2 layers in the HTSCs. A correlation between the strength of B_{irr} and the spacing between two CuO_2, pyramid sheets sandwiching a unit of charge reservoir block between them (d_i) in the crystals was pointed out for a variety of high-T_c superconductors [204]. It has been pointed out that it is the

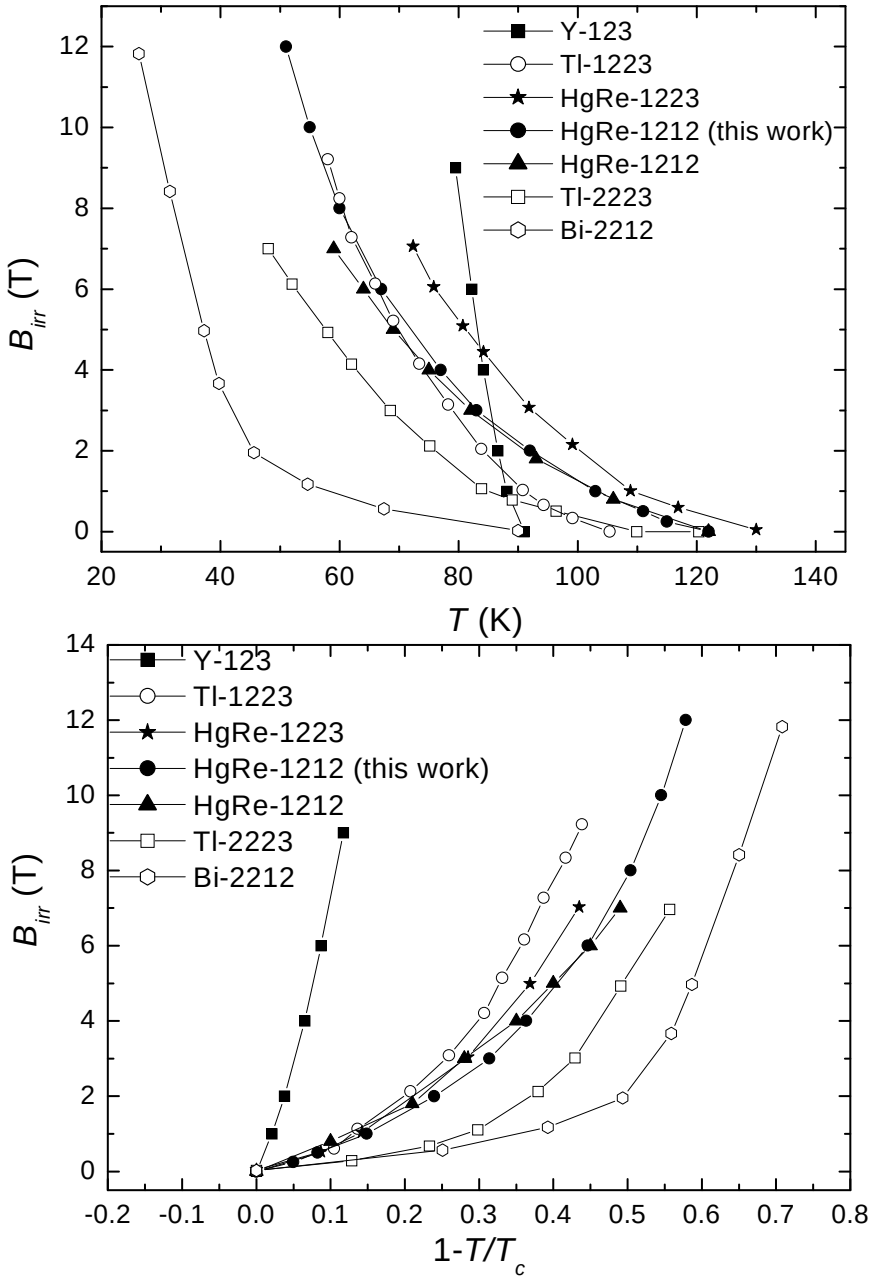

Figure 7.3: *The irreversibility field B_{irr} as a function of the temperature (top) and as a function of the reduced temperature (1-T/T_c) (bottom) respectively with the magnetic field oriented parallel to the c-axis for the $(Hg_{0.9}Re_{0.1})Ba_2CaCu_2O_{6+\delta}$ film from the present measurement and published data for other high T_c cuprates [162, 163, 164, 165, 166, 215]. All lines are guides for the eye.*

insulator spacing (d_i) between the adjacent CuO_2 bi- or tri-layer in the structure, rather than the repeat distance of the closely coupled CuO_2 layers (s), that determines the amount of the resistive broadening, and therefore the position of the irreversibility line. Thus the irreversibility line for the single layer Tl-1223 and Hg-1212 are higher than those for the two-layer Bi-2212 and Tl-2212/Tl-2223 cuprates. The values for d_i in Y-123, Tl-1223, Hg-1223, and Bi-2213 crystals have been reported to be 8.3 Å [219], 8.7 Å [219], 9.5 Å [49, 220], and 11.8 Å [219], respectively. Actually, in the bottom of Fig. 7.3, the B_{irr} vs 1- T/T_c curves are located in the order: Y-123 > Tl-1223 > HgRe-1212 (this work) > Tl-2223 > Bi-2212. The $(Hg_{0.9}Re_{0.1})Ba_2CaCu_2O_{6+\delta}$ phase is likely to be more advantageous in practical applications than Bi-compounds, if the high value of T_c is taken into account.

Figure 7.4 shows the $B_{irr}(T)$ line of the superconducting $(Hg_{0.9}Re_{0.1})Ba_2CaCu_2O_{6+\delta}$ film with fields up to 12 T. The irreversibility field was redrawn in Fig. 7.4 as a function of (1-T/T_c) in a double logarithmic plot. The irreversibility lines for $(Hg_{0.9}Re_{0.1})Ba_2CaCu_2O_{6+\delta}$ shows a power-law dependence over the entire range of data but with a different exponent n, which depends strongly on the coupling between the CuO_2 blocks. The irreversibility line $B_{irr}(T)$ for the $(Hg_{0.9}Re_{0.1})Ba_2CaCu_2O_{6+\delta}$ film can be well fitted to the simple power law equation : $B_{irr}(T) = A(1 - T/T_c)^n$, with $n = 1.8$ for 1-$T/T_c < 0.3$ and with $n = 2.6$ for 1-$T/T_c > 0.3$. Here A is the irreversibility line B_{irr} at $T = 0$ K. It could be considered that T_{irr} is the irreversibility temperature at zero-applied field, $T_{irr}(B = 0)$, which approaches the zero-field superconducting critical temperature, $T_c(B = 0)$. Experimental data are used to determine A and n. The best fitting results are obtained as follows: in the low field ($B_{irr} \leq 2$ T, i.e. 1-$T/T_c < 0.3$) region, one gets $n = 1.8$ and $B_{irr}(0)$= 8.4 T and, in the high field ($B_{irr} \geq 3$ T, i.e. 1-$T/T_c > 0.3$) region $n = 2.6$ and $B_{irr}(0)$= 43.7 T. The distance between two CuO_2 blocks can be used to characterize the coupling strength. It is 9.51 Å for Hg-1212 which lies between those of Y-123 (8.245 Å) and Bi/Tl-2212 (11.8 Å). This indicates that the coupling strength of Hg-1212 is between those of Y-123 and Bi/Tl-2212. Our observation supports that there is a correlation between n and anisotropy and/or coupling where the irreversibility line of superconducting $(Hg_{0.9}Re_{0.1})Ba_2CaCu_2O_{6+\delta}$ thin films lie between those of Y-and Bi/Tl-based high temperature superconductors. We can surmise that $B_{irr} - T$ depends strongly on

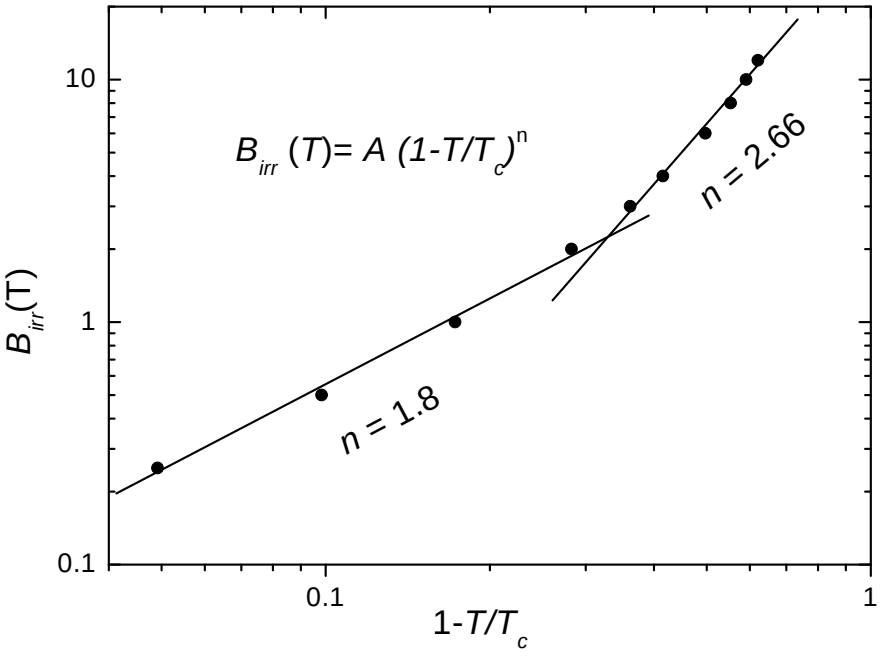

Figure 7.4: *The irreversibility line $B_{irr}(T)$ as a function of the reduced temperature (1 -T/T_c) in a log-log plot with the magnetic field oriented parallel to the c-axis for the $(Hg_{0.9}Re_{0.1})Ba_2CaCu_2O_{6+\delta}$ film. The two lines are the fitting curves to power-law equations: $B_{irr}(T) = A(1 - T/T_c)^n$, with n = 1.8 for 1-T/T_c < 0.3 and with n = 2.6 for 1-T/T_c > 0.3.*

anisotropy which, in turn, depends on the coupling between CuO_2 layers in the HTSCs.

7.2 Critical current density

The critical current density J_c is one of the key parameters of high-T_c superconductors. In particular, knowing the dependence of J_c on the magnetic field is a key concern for the study of the current-carrying states of the superconductors. The $J_c(H)$ dependence was measured from two general types of experiments: electrical and magnetic. In electrical transport measurements, the reliability and repeatability of the measured values of the critical current are reduced because of the difficulties in making contacts in the sample and in choosing a voltage criterion for defining J_c. The other general method for obtaining J_c is from magnetization

measurements, typically isothermal magnetization loops $M(H_a)$, where H_a is the applied field. In contrast to the transport critical current density measurements, magnetization measurements do not require electrical contacts to the specimen. The J_c is obtained from the width ΔM of the $M(H_a)$ hysteresis loop using

$$J_c(H) = \Delta M(H)/d \tag{7.2}$$

where d is a characteristic scale length of the sample.
The J_c is based on the Bean critical state model [42, 43], which is by far the most widely used of the critical state models that have been proposed for describing the field and current distribution in a superconductor. The model assumes:

* the critical current density is independent of the field, i.e., the current density in the superconductor is either J_c or 0 everywhere,

* the internal magnetic field is given by the Maxwell equation

$$\triangle \times B = \mu_0 J_c(B), \tag{7.3}$$

* the lower-critical field H_{c1} is very small and can be ignored.

The concept of the critical state plays a central role in understanding the irreversible magnetization in hard type II superconductors. In the critical state, a superconductor responds to a change in the applied field via shielding currents that flow at the level of the critical current density J_c. If the applied field increases above H_{c1}, the flux lines penetrate into the superconductor. The lines adjust themselves so that the driving force arising from the flux density gradient is equal to the maximum pinning force. The field penetration profile in the superconductor is determined, in conjunction with proper boundary conditions, by the Maxwell equation (Eq. 7.3). In the Bean critical state model, $J_c(B)$ is assumed to be constant and has the value $\pm J_c$ in the magnetized region. To further simplify this equation, consider a magnetic field applied in the z direction to a slab which is thin in the x direction and extends to infinity in the y and z directions. Equation (7.3) then reduces to

$$\frac{dB}{dx} = \mu_0 J_c. \tag{7.4}$$

Thus, in a superconductor in the critical state, the magnetic field gradient is directly proportional to the critical current density.
The intragrain critical current density J_c is usually deduced from the Bean's model for slab shaped superconductors. To estimate J_c from hysteresis loops using Bean's model, it is assumed the material is homogeneous and fully penetrated by the magnetic field; thus $J = J_c$ throughout the sample. The magnetic moment of the sample can be calculated in terms of J_c from the sum of currents loops within the sample. For spherical shaped samples, the Bean model equation for J_c is:

$$J_c = 30\frac{\triangle M}{R}, \tag{7.5}$$

where J_c is given in A/cm^2, R is the circulation radius of the current in cm, and $\triangle M$ is the width of the hysteresis loop in emu. Using the Bean model equation (7.5), J_c can be calculated from the hysteresis loop by measuring the difference between the magnetization $\triangle M(= M \uparrow -M \downarrow)$ in increasing and decreasing fields.
A SQUID magnetometer can be used to measure the magnetic hysteresis and therefore estimates the magnetization critical current density (J_c) of the $(Hg_{0.9}Re_{0.1})$ $Ba_2CaCu_2O_{6+\delta}$ fully textured HTSC thin films at different fields.

7.2.1 Magnetization measurements by SQUID

Quantum Design's Magnetic Property Measurements System (MPMS), which utilizes a SQUID magnetometer based on the Josephson junction, is the most common and sensitive instrument used to measure small changes in the magnetic properties of samples. The SQUID is only one part of the SQUID magnetometer. A typical SQUID magnetometer consists of five other major components: a cryostat, a superconducting magnet to generate high magnetic fields, a superconducting pick-up (or detection) coil, which couples inductively to the sample, sufficient magnetic shielding surrounding the SQUID, and a heatable sample space. Although the magnetometer uses a SQUID to determine the magnetic response of samples, it does not directly detect the magnetic field from the sample. Instead, the sample moves through a system of superconducting pick-up coils that are connected to the SQUID by superconducting wires, allowing the current from the detection coils to inductively couple with the SQUID sensor. When correctly

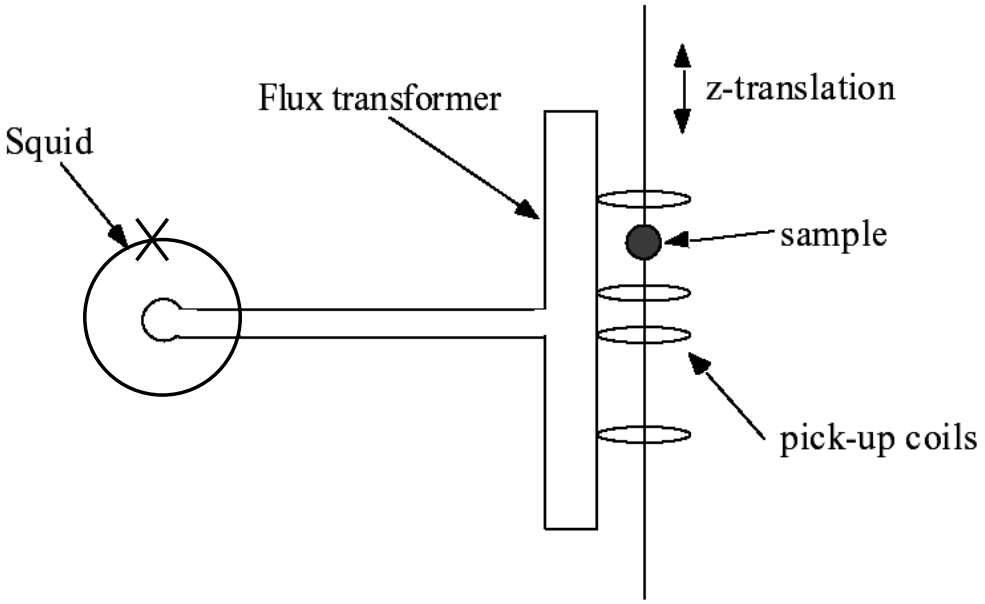

Figure 7.5: *MPMS SQUID pick-up coils arrangement.*

configured, the SQUID electronics produces an output voltage which is proportional to the current flowing in the SQUID input coil; thus it essentially functions as a sensitive current-to-voltage converter.

A commercial rf- superconducting quantum interference device (rf-SQUID) magnetometers was used for the dc magnetization measurements, which allows measurements in the temperature range 1.6 K to 400 K in magnetic fields between -6 T and +6 T. This magnetometer necessitates the movement of the sample through a pick up coil system (second order gradiometer) for the measurements. The SQUID response to this movement is fitted using the ideal response for a point dipole of constant magnetic moment and the sample's magnetic moment at the temperature of the measurement is calculated. This magnetometer will be denoted as MSM (Moving Sample Magnetometer). A measurement is performed by moving a sample through the superconducting pick-up coils, which are located outside of the sample chamber. Sample is moved with a linear stepper motor through coils which are linked to the input coil of a SQUID through a superconducting flux transformer, as shown in Fig. 7.5. As a sample is moved through the pick-up coils, measurements of the voltage variations from the SQUID detector

provide a highly accurate measurement of the sample's magnetic moment.
On SQUID measurements we should take into account the following notes:

- Moment coming from the holder adds to the sample moment (best to subtract holder response point by point before fitting). Therefore mass and susceptibility of sample holder should be minimized as much as possible (drinking straw, geletine capsules).

- Field may not be sufficiently uniform over scan length (shorter scan lengths decrease accuracy but improve field uniformity).

- Beware of possible remenant magnet fields (zero field may be really several 10's of gauss depending on history of superconducting solenoid).

7.2.2 Magnetization loops and critical current density of the $(Hg_{0.9}Re_{0.1})Ba_2CaCu_2O_{6+\delta}$ thin films

When a superconducting material is magnetized in one direction, it will not relax back to zero magnetization when the imposed magnetizing field is removed. It must be driven back to zero by a field in the opposite direction. If an alternating magnetic field is applied to the material, its magnetization will trace out a loop called a hysteresis loop. The lack of retraceability of the magnetization curve is the property called hysteresis and it is related to the existence of a remanent magnetic moment in the material. The magnetic hysteresis loop in superconductors is a significant characteristic reflecting the flux pinning properties, e.g. the critical current density J_c. For this reason, its measurement is one of the useful methods to investigate the flux line dynamics. Magnetization measurements are very effective for estimating J_c properties for HTSC materials as well as for the investigation of the presence of weak links or the magnetic force pining. Also magnetization is frequently reported as an easier method to obtain J_c compared to the ordinary four-probe method.
To determine the critical current density J_c of the $(Hg_{0.9}Re_{0.1})Ba_2CaCu_2O_{6+\delta}$ thin films, magnetization measurements were performed in a ^{4}He moving sample magnetometer (MSM). The instrumental sensitivity of the SQUID magnetometer is specified with 10^{-8} emu (1 emu = 1 erg/G) in Gaussian units or 10^{-11} J/T

(= Am^2) in SI units. Although this device uses a SQUID to determine the magnetic response of samples, it does not detect directly the magnetization of the sample. We studied magnetization loops to indirectly evaluate the J_c behavior. The corresponding $M - H$ loops were measured at different temperatures with a magnetic field applied normal to the film.

Hysteresis loops of the $(Hg_{0.9}Re_{0.1})Ba_2CaCu_2O_{6+\delta}$ thin film as a function of the applied field are shown in Fig. 7.6 for several temperatures between 5 K and 100 K. The loops are similar to those of other HTSC compounds. The figure shows hysteresis loops traversed over a broad field range and varied with the temperature. It is observed that as the temperature decreases, the loop area increases, and a strong decrease of the hysteresis width with temperature is appreciated. The large hysteresis is an indication of flux pinning. The area of the hysteresis loops increases as the pinning strength increases and a corresponding increase in the J_c value is observed. Also, at the lower temperatures the ascending and descending field branches are quite symmetric, indicating that bulk pinning is responsible for the observed irreversibility. As the temperature increases, the hysteresis cycles loose their symmetric character, denoting a strong reduction of bulk pinning. Surface barriers become then the main contribution to the magnetic irreversibility of these superconductors, as revealed by values close to zero [221].

The penetration of magnetic flux into a superconductor depends crucially on two elements, geometry and pinning. These are both incorporated in what is usually called the critical-state model, originally due to Bean [42, 43]. Bulk pinning is described in terms of the critical current J_c, while the field profiles depend heavily on the sample geometry. It is important to understand flux profiles and field penetration into thin films. Recently there have been several calculations based upon critical-state models which have yielded field and current distributions in thin films for magnetic fields applied perpendicular to the films, and have shown that there are qualitative differences from bulk geometries. While some of these results have been tested in actual experiments [222], not all aspects of these models are fully understood. Most experimental studies of flux penetration and the critical state have involved measurements of magnetic properties such as the dc magnetization, and there are few investigations of the dynamic properties.

From the previous observations it has become clear that thin films are in a com-

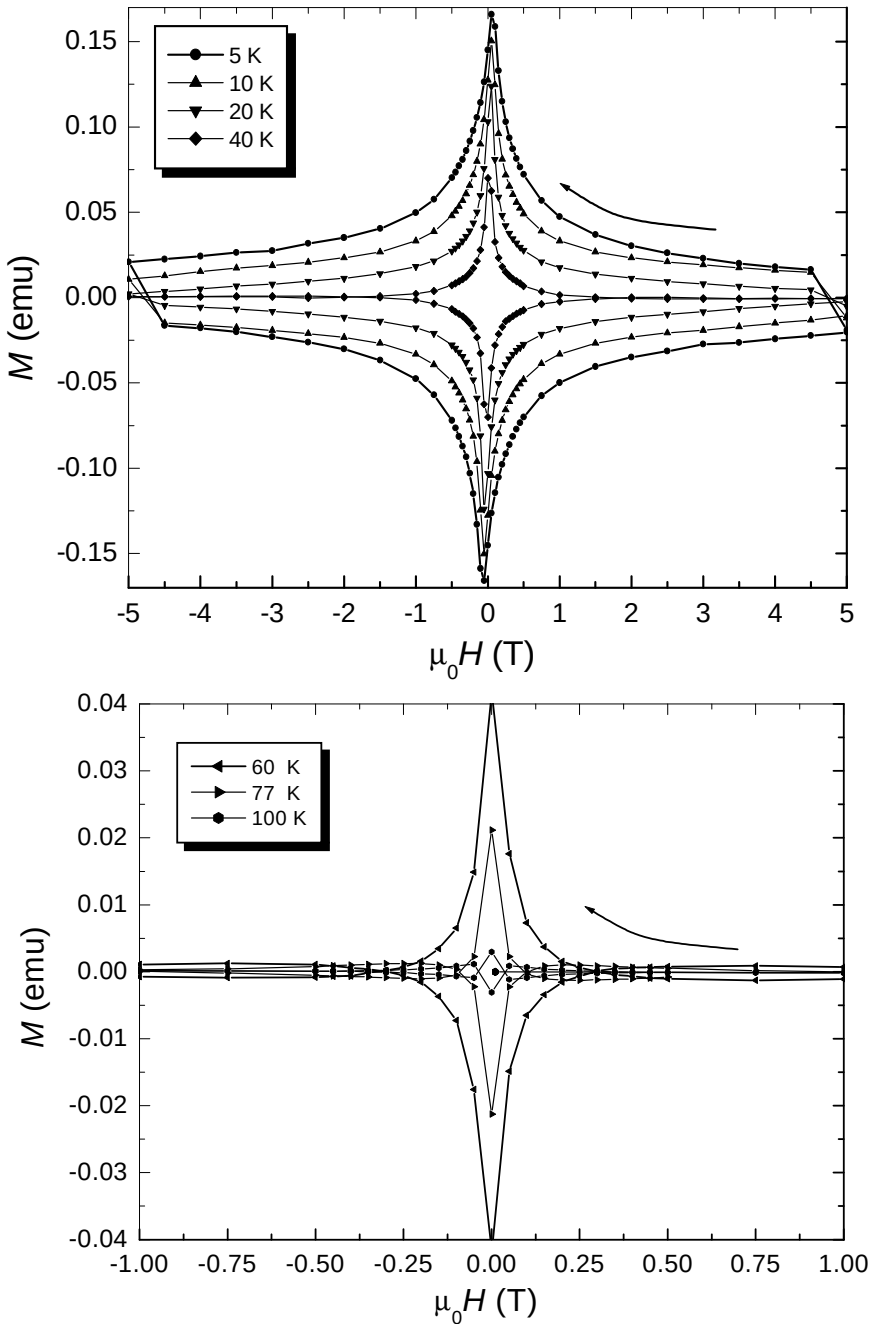

Figure 7.6: *High-field hysteresis loops of the* $(Hg_{0.9}Re_{0.1})Ba_2CaCu_2O_{6+\delta}$ *thin film cycled over the same field scan, -5 T* $\leq H_{app.} \leq$ *+5 T , over a range of temperatures, showing the appearance of bulk pinning effects at low temperatures and low fields.*

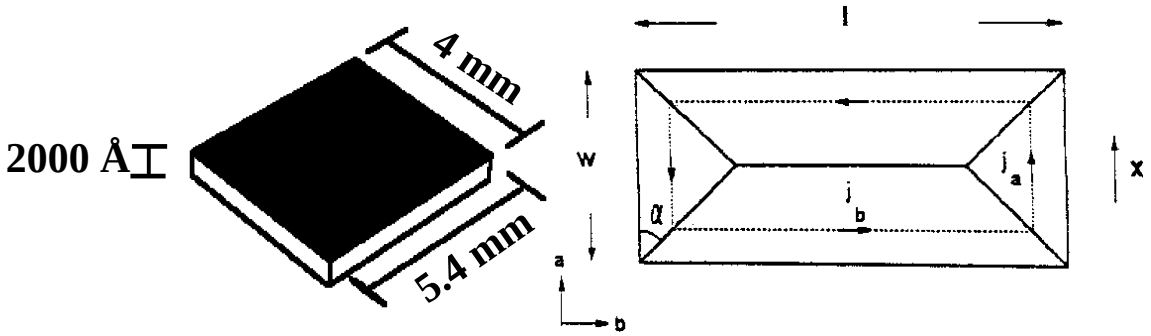

Figure 7.7: *Left: Prepared form of* $(Hg_{0.9}Re_{0.1})Ba_2CaCu_2O_{6+\delta}$ *thin film used Right: Current path in a rectangular film sample.*

plete critical state already at very low fields: The current J_c flows everywhere in the sample. From here it follows a simple proportionality between the critical current density J_c and the magnetic moment of the sample:

$$m\,[\mathrm{emu}] = \frac{J_c}{2}\int \mathbf{r}\times\hat{\mathbf{J}}\;dV \tag{7.6}$$

It should be noted on the following presented measurements that the measured points could be always recorded 3-4 minutes after reaching a new field value. As long as it was not the case, the penetrating field perturbations made measurements impossible. According to this, the measured values represent the magnetic moments that that were relaxing during 3-4 minutes.

Fully textured $(Hg_{0.9}Re_{0.1})Ba_2CaCu_2O_{6+\delta}$ HTSC thin film had a rectangular structure as shown on the left-hand side of Fig. 7.7. Assuming that the current takes a path as in right-hand side of Fig. 7.7 one gets for the magnetic moment

$$m\,[\mathrm{emu}] = \int_0^{w/2} a(x)\,b(x)J\,d\,dx = \frac{1}{4}\,d\,w^2\left(l-\frac{w}{3}\right)J, \tag{7.7}$$

with the path lengths $a(x) = 2X$ and $b(x) = l-w+2x$ which depend on the depth. Again one can write down the estimated equation of the critical current density J_c of the $(Hg_{0.9}Re_{0.1})Ba_2CaCu_2O_{6+\delta}$ thin films estimated from magnetization (M) measurements as follows

$$m\,[\mathrm{emu}] = \frac{1}{4}10^{-12}d[\mathrm{\AA}]w^2[\mathrm{mm}^2]\left(\ell[\mathrm{mm}]-\frac{w[\mathrm{mm}]}{3}\right)J_c[\mathrm{A/cm}^2] \tag{7.8}$$

where m, d, w, and ℓ are the magnetic moment, thickness ($\approx 2000\,\text{Å}$), width, and length of the thin film. The critical current density (J_c) as a function of applied magnetic fields and temperatures was calculated using the total area covered by the film ($4\,\text{mm} \times 3\,\text{mm}$). Because the sample size was used instead of the grain size, the calculated J_c represents the inter-grain critical current J_c in the sample. During the experimental work, precursor targets with the different sets of starting materials have been prepared to grow the Hg-HTS thin films on (100) single crystals $SrTiO_3$ substrates with PLD. Figures 7.8-top, -middle, and-bottom display the critical current densities J_c as a function of applied magnetic at the temperature 5 K for $(Hg_{0.9}Re_{0.1})Ba_2CaCu_2O_{6+\delta}$ films prepared by the target no 1, no 2, and no 3, respectively. Hysteresis loops of the $(Hg_{0.9}Re_{0.1})Ba_2CaCu_2O_{6+\delta}$ thin films as a function of the applied field are shown in the insets of Figs. 7.8 for the temperatures 5 K and 77 K. Compared to the films prepared from the first and the second target, the film prepared from the third target shows a much wider hysteresis loop, higher irreversibility field, and higher J_c at the same temperature. This clearly demonstrates that the pinning force of the HTSC $(Hg_{0.9}Re_{0.1})Ba_2CaCu_2O_{6+\delta}$ thin films is significantly enhanced using the preparing method of the third target, the irreversibility behavior, and the J_c are greatly improved as well. Figure 7.9 shows the critical current density J_c as a function of the applied magnetic fields and temperatures for the $(Hg_{0.9}Re_{0.1})Ba_2CaCu_2O_{6+\delta}$ thin film. The calculated critical current density of the $(Hg_{0.9}Re_{0.1})Ba_2CaCu_2O_{6+\delta}$ film was 1.2×10^7 A/cm^2 at 5 K and $\approx 2 \times 10^6$ A/cm^2 at 77 K, which is in the range of the best reported results on Hg-1212 films. These films have been fabricated by different methods as by reacting TlBaCaCuO precursor films in controlled Hg-vapor pressure through Tl−Hg exchange [223], by oxygen annealing of HgRe-1223 films [108, 136], and by multilayer deposition of HgO/M-Ba-Ca-Cu-O multilayer precursor films [215]. J_c falls off exponentially with the field over the measured temperatures. Two field dependences are discernible: a weak dependence at lower temperature ($T \leq 20$ K) and a strong dependence at higher temperature ($T \geq 40$ K). The change of the field dependence is attributed to a transition from a vortex lattice at low temperature to a vortex liquid at high temperature [224]. These data are again much higher than the best result achieved in other Hg-samples.

Figure 7.10 shows the temperature dependence of the critical current density, for

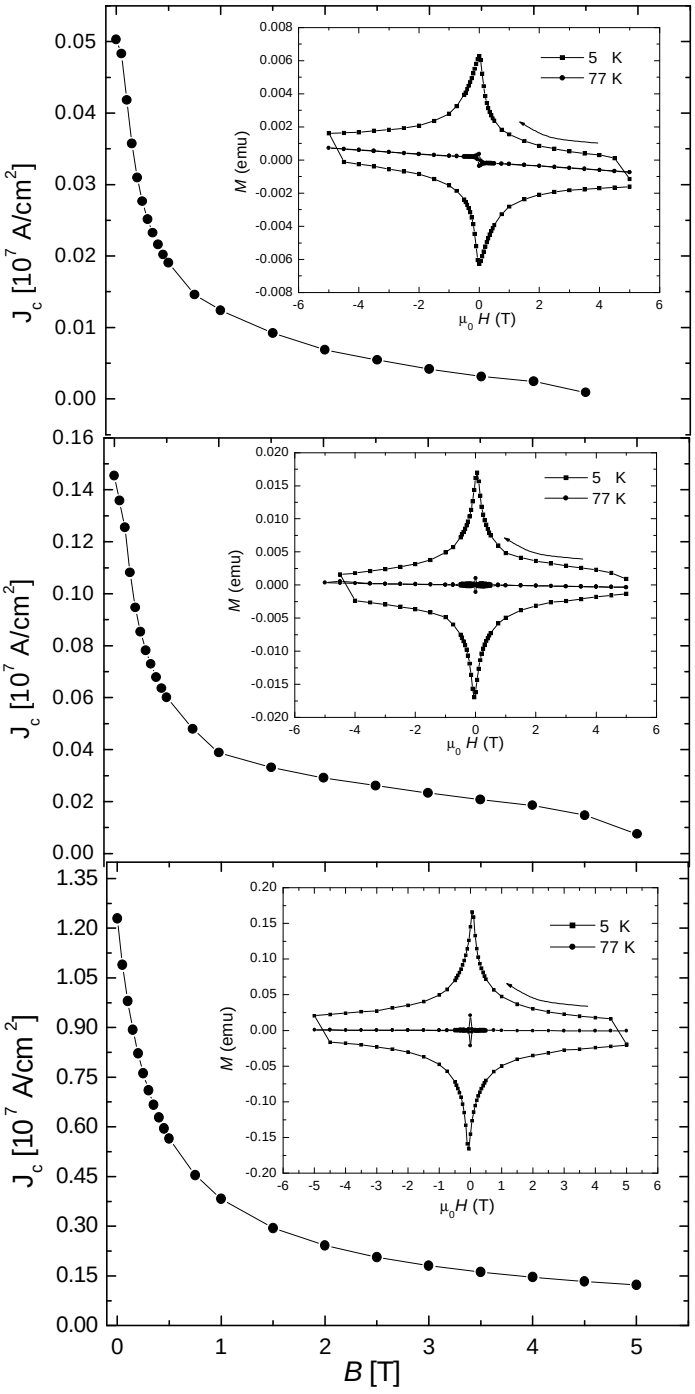

Figure 7.8: *The critical current density J_c as a function of applied magnetic field at 5 K for different $(Hg_{0.9}Re_{0.1})Ba_2CaCu_2O_{6+\delta}$ thin films prepared from different targets. The insets show the hysteresis loops as a function of the applied field for the temperatures 5 K and 77 K.*

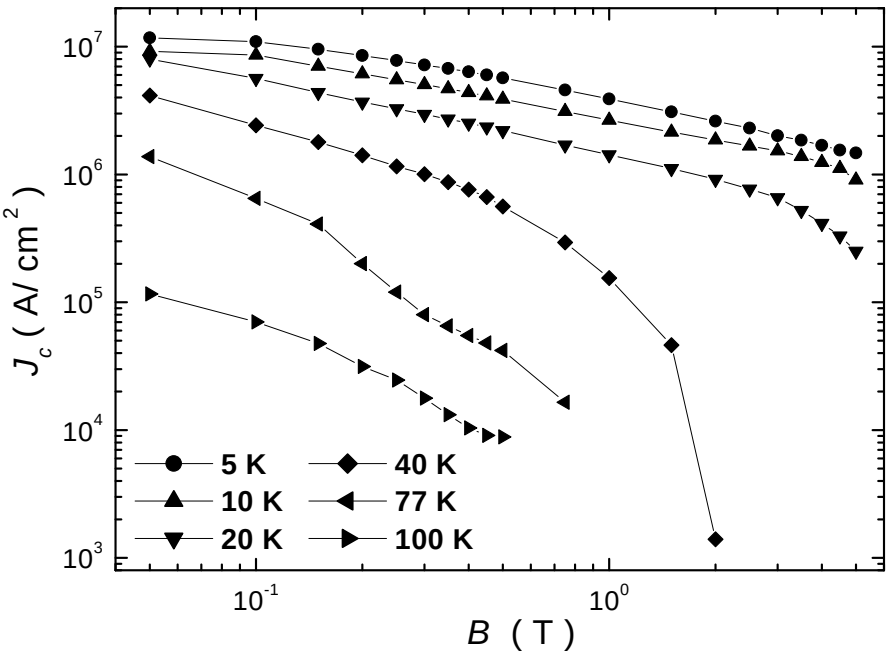

Figure 7.9: *The critical current density J_c as a function of the applied magnetic fields and temperatures for the $(Hg_{0.9}Re_{0.1})Ba_2CaCu_2O_{6+\delta}$ thin film. Two field dependences are discernible: a weak dependence at lower temperature ($T \leq 20$ K) and a strong dependence at higher temperature ($T \geq 40$ K). All lines are guides for the eye.*

a (Hg, Re)-1212 thin film at fields between 0.02 T and 5 T. Three regimes of behavior are identified. In regime II ($T_I < T < T_{II}$), J_c decays more slowly with temperature compartment with regime I ($T < T_I$) and regime III ($T > T_{II}$), J_c. Regime I is characterized by a strong temperature dependence. The rapid decrease in J_c at low temperature is caused by the degradation of superconductivity in weak link regions with increasing temperature, as reported by Matsushita et al. [225]. By observing the history effect of J_c, they concluded that the strong temperature dependence of J_c originates from weak links in the Pb-doped Bi-2223 tapes at temperatures below 30 K, compared to 20 K (T_I) for the (Hg, Re)-1212 thin films studied here. In regime II, J_c follows an exponential decay. This temperature dependence arises from thermally activated depinning of vortices that reduces the flux density gradient [224]. The most rapid decay of J_c occurs in regime III, which is due to giant flux creep at high temperature. Note

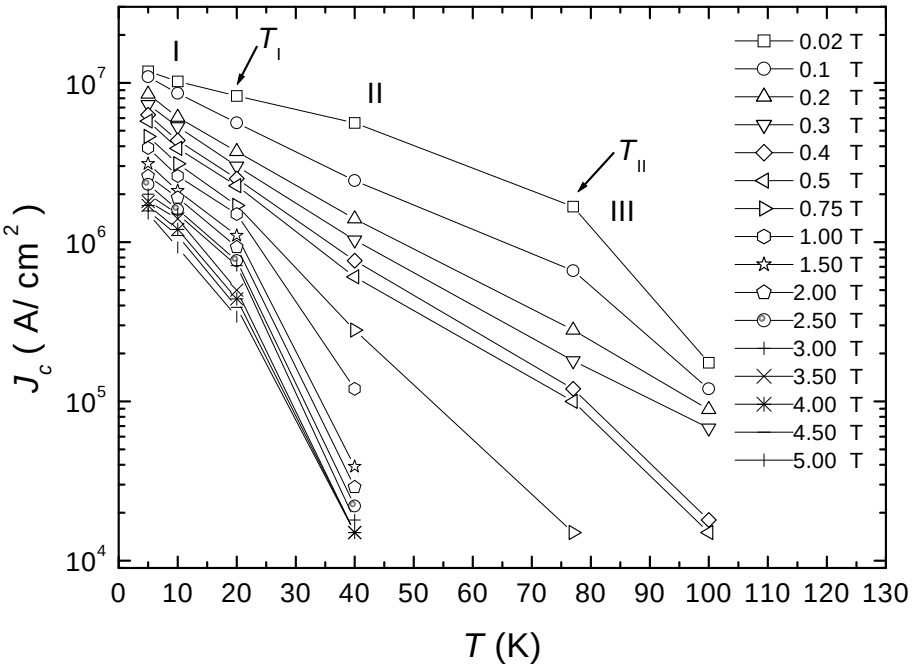

Figure 7.10: *The critical current density J_c versus temperature of a (Hg,Re)-1212 thin film as a function of the magnetic field. The three regimes of temperature dependence were discussed in the text. All lines are guides for the eye.*

that regime II almost disappears as the field increases ($\geq$ 1 T).

Note that the current density estimated by Bean model equation is a magnetization critical current density, J_c, which is distinctly different from a transport critical current density, J_c^{tran}.

Anderson [142] and Kim [144] modified the Bean model [42, 43], by considering the case where J_c varies with the local magnetic field suggesting that J_c should decrease with increasing local magnetic field and has the form,

$$J_c\,(B,T) = \frac{J_c\,(T)}{(1+B/B_0)} \tag{7.9}$$

where B_0 is a material parameter. This model is shown as a dotted line and was fairly consistent with our J_c results for $(Hg_{0.9}Re_{0.1})Ba_2CaCu_2O_{6+\delta}$ thin films (Fig. 7.11). Recently, Xu [205] has modified the previous equation using the following form,

$$J_c\,(B,T) = \frac{J_c\,(T)}{(1+B/B_0)^{\beta}} \tag{7.10}$$

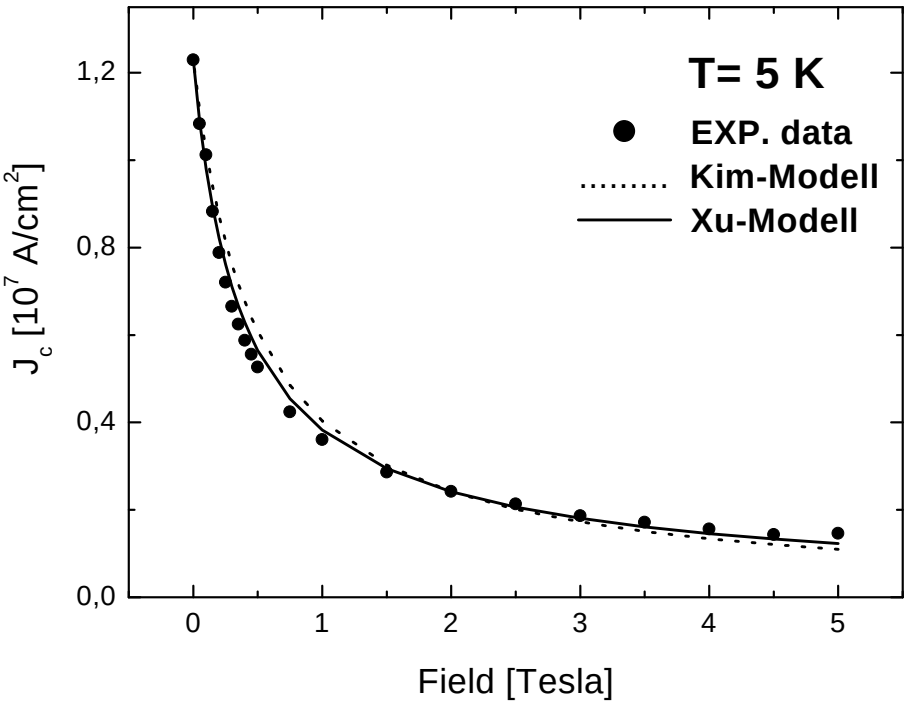

Figure 7.11: *Magnetic field dependence of the critical current density of the* $(Hg_{0.9}Re_{0.1})Ba_2CaCu_2O_{6+\delta}$ *thin film and fit of the model of Xu with* β*= 0.85, which changes for* β*= 1 into the Anderson-Kim model.*

where β is a dimensionless constant and depends on the details of flux pinning. A range of different cases, corresponding to $1/4 < \beta < 4$ has been derived from the collective flux-pinning theory by [226]. This fit is shown as a solid line in Fig. 7.11 and is in perfect agreement with the data.

Chapter 8

Normal and mixed state Hall effect

8.1 A short review of the Hall effect in High-T_c superconductors

The Hall effect of high temperature superconductors (HTSCs) has been studied extensively in both the normal and the mixed-state. One of the most remarkable observations in the normal and the mixed-state of HTSCs is the unconventional behavior of the Hall effect. In the normal state, Hall effect measurements provide information on the sign, concentration, and mobility of charge carriers. The most important result obtained from Hall effect measurements in the normal state (above T_c) is that the charge carriers in the copper-oxide planes of the lanthanum, yttrium, bismuth, thallium, and mercury based HTSC compounds are holes. The exception is $(Nd_{1-x}Ce_x)_2CuO_4$ superconductors, with electron-like conduction [227, 228].

The Hall effect in the mixed state of HTSCs is of an anomalous nature: below T_c, the sign change of the Hall resistivity in the mixed state of both high-T_c and low-T_c superconductors has been one of the most puzzling and controversial transport phenomena [229, 230]. In the normal state the Hall sign is determined by the topology of the Fermi surface, while in the superconducting state it is determined by the vortex motion. Near the transition is a range of temperatures and magnetic fields where the sign of the Hall effect is opposite to that in the normal state. So

far, two kinds of sign reversals have been observed. The first is a simple, single sign reversal and the second is a double sign reversal from positive to negative and then to positive again as the temperature decreases. The distinction between the two is that the single sign reversal is observed for the case of relatively low anisotropy while the double sign reversal is observed in the case of relatively high anisotropy, where in the most anisotropic materials and weak pinning materials in the mixed state, the Hall effect often displays two successive sign changes. This has been observed in bismuth [231], thallium [232], and mercury [233] based compounds. A single sign reversal of the Hall resistivity was first observed in yttrium-based compounds $YBa_2Cu_3O_{7-\delta}$ by Galffy et al.[234], where the sign changes from positive to negative with decreasing temperature. A double sign reversal has been also reported in $YBa_2Cu_3O_{7-\delta}$ thin films in very low magnetic fields [235]. Recently, even a third sign reversal has been reported for $HgBa_2Ca_{n-1}Cu_nO_{2n+2+\delta}$ [236] with columnar defects. This observation is quite meaningful because this multiple sign reversal was predicted by Kopnin, who expected the possibility of a third sign reversal of the Hall effect when the system remains moderately clean. If $B < B_{c2}$, this third reversal would even occur at low temperatures [237]. This multiple sign reversal is possible if there are localized or almost localized energy states in the superconducting state. The universality of the phenomenon in question is indicative of its connection with some general properties of the mixed state of type-II superconductors, namely with peculiarities of the motion of magnetic flux vortex lines (vortices) in these superconducting materials. Various models have been proposed to interpret these Hall anomalies, but they have not been able to explain all the experimental results.

When a type II superconductor in a magnetic field is cooled down from a normal state into a superconducting state a quantized magnetic flux (vortex) is created inside the superconducting medium. Among the first theories of vortex motion stands the pioneering work of Bardeen and Stephen [186] (1965, to be referred to as BS), whose description of the forces acting on the vortices is as follows: in the absence of a driving current, the only force acting on the vortices is a viscous drag. However, upon application of a transport current, the vortices move perpendicular to the current direction due to the Lorentz force $\mathbf{f}_{\mathrm{L}} = \mathbf{J} \times \mathbf{B}$, where $\mathbf{J}$ is the applied current density and $\mathbf{B}$ is the average magnetic induction. This neglects any forces resulting from interaction between vortex lines. In this scenario, we can not detect

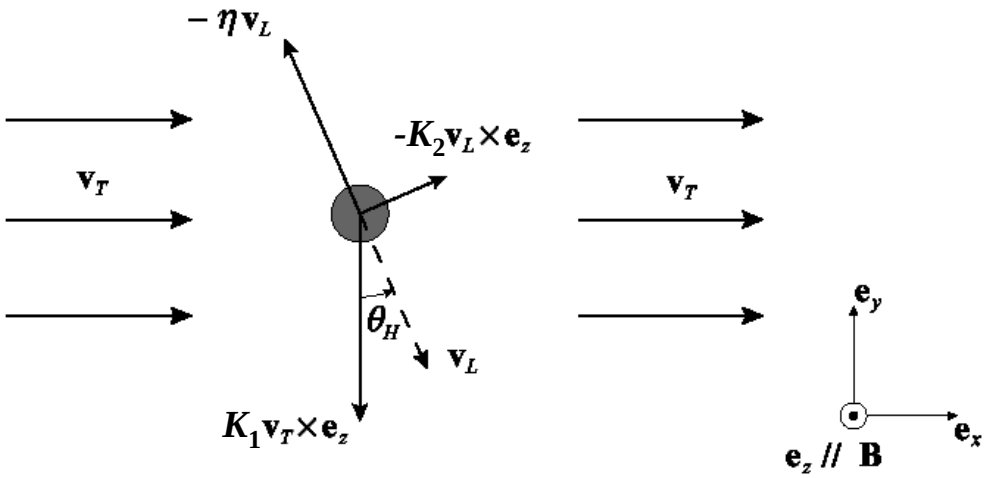

Figure 8.1: *Schematically description of the stationary state of the different forces appearing in the vortex equation of motion (8.1).*

the Hall voltage because the electric field arising by vortex motion is parallel to the current direction. In order to solve this discrepancy to the experimental results, Nozieres and Vinen [238] (1966, to be referred to as NV) considered the transverse force, Magnus force, as a possible origin of the longitudinal component of vortex velocity. This force plays the same role as the Lorentz force for electrons. Kopnin, Ivlev, and Kalatsky [239] proposed vortex-traction force by the transport supercurrent.

According to the classical models [186, 238], the moving vortices should generate a Hall voltage with the same sign as observed in the normal state because normal electrons in the vortex cores effectively produce this voltage. In the absence of pinning, the vortices will move under the influence of the Lorentz force $\mathbf{f}_{\rm L}$ in the direction perpendicular to $\mathbf{J}$, but this moving flux tube will generate quasiparticles which will subject the vortices to a damping force $\mathbf{f}_{\rm d}$. This damping force is velocity dependent and is commonly assumed to be directed opposite to the vortex velocity, $\mathbf{f}_{\rm d} = -\eta\mathbf{v}_{\rm L}$, where η is a constant determined by the vortex and the conductivity in the normal state; the vortex velocity will increase until $\mathbf{f}_{\rm L}$ and $\mathbf{f}_{\rm d}$ balance each other. For the purpose of simplification, the case of a single vortex in a superconductor will be considered, and we shall derive formally the equation of motion of a single vortex in the absence of pinning according to the

Bardeen-Stephen and the Nozire-Vinen models [186, 238], as shown schematically in Fig.8.1. The situation shown is that of a superconductor in the vortex state, with the magnetic field in the z direction perpendicular to the plane with a current applied in the x direction. In the stationary state the equation of motion follows

$$(K_1\mathbf{v}_\mathrm{T} - K_2\mathbf{v}_\mathrm{L}) \times \mathbf{e}_\mathrm{z} - \eta\mathbf{v}_\mathrm{L} = 0, \tag{8.1}$$

where $\mathbf{v}_\mathrm{T}$ is related to the applied transport current (providing the driving force) by $\mathbf{J} = n_s e\mathbf{v}_\mathrm{T}$ (with n_s being the density of superconducting carriers, e their charge, and $\mathbf{v}_\mathrm{T}$ their velocity), $\mathbf{v}_\mathrm{L}$ is the velocity of the straight vortex, and $\mathbf{e}_\mathrm{z}$ a unit vector in z direction. With a very intuitive view emerging from, for example, the Bardeen-Stephen theory, the different terms can be justified as follows (see Fig. 8.1):

* $K_1\mathbf{v}_\mathrm{T} \times \mathbf{e}_\mathrm{z}$ is the Lorentz force resulting from the interaction between the transport current, $\mathbf{J} = n_s e\mathbf{v}_\mathrm{T}$, and the magnetic field $\mathbf{B}$,

* $-K_2\mathbf{v}_\mathrm{L} \times \mathbf{e}_\mathrm{z}$ can be seen as the consequence of the Lorentz force acting on the normal charge carriers localized in the vortex core, moving at the vortex velocity $\mathbf{v}_\mathrm{L}$,

* $-\eta\mathbf{v}_\mathrm{L}$ is simply a viscous drag force or a frictional force opposed for the vortex motion, due to the scattering of these localized charges.

Note that $\eta > 0$, whereas both K_1 and K_2 have the same sign as the charge e in this simple model. More precisely, the damping coefficient η comes from the interactions between the excited, nonsuperconducting states localized in the vortex core and the imperfections of the background material made of positive ions, leading to a finite characteristic collision time for the excited states. The coefficients K_1 and K_2 have multiple and more complex origins. They are in general determined by hydrodynamic (Magnus) and core forces, arising from the interactions between the superflow around the vortex and the excitations of the superconducting condensate (both localized in the vortex core and delocalized in the whole charged fluid). The interface between the vortex core and the bulk superfluid also plays an major but non-trivial role in the determination of the different factors in the equation of motion [240].
In the mixed state of a type-II superconductor, Josephson has shown that vortices

moving with velocity $\mathbf{v}_{\rm L}$ generate a perpendicular dc electric field $\mathbf{E}$ which results in a flux-flow resistivity. This electric field is given by [241]

$$\mathbf{E} = -\mathbf{v}_{\rm L} \times \mathbf{B}. \tag{8.2}$$

where $\mathbf{B}$ is the magnetic field and $\mathbf{E}$ is the measured longitudinal electric field. We can actually use this relation to directly relate the equation of motion to the different components of the resistivity tensor. For the sake of simplicity, we consider here a conductor which is invariant under a $\pi/2$ rotation around the z-axis, such that the properties along the x and y directions are equivalent. Hence the resistivity tensor (defined by the relation $\mathbf{E} = \rho\mathbf{J}$) has the form

$$\rho = \begin{pmatrix} \rho_{xx} & -\rho_{yx} \\ \rho_{yx} & \rho_{xx} \end{pmatrix},$$

where ρ_{xx} is the longitudinal resistivity and ρ_{yx} is the transverse resistivity. ρ_{xx} is symmetric in the magnetic field, namely $\rho_{xx}(\mathbf{B}) = \rho_{xx}(-\mathbf{B})$, whereas ρ_{yx} is anti-symmetric, that is $\rho_{yx}(\mathbf{B}) = -\rho_{yx}(-\mathbf{B})$, such that ρ_{yx} is in fact strictly identified as the Hall resistivity.
From the above definitions and Eq. (8.2) [241], one gets

$$\mathbf{v}_{\rm L} = \frac{n_s e}{B}(\rho_{yx}\mathbf{v}_{\rm T} + \rho_{xx}\mathbf{v}_{\rm T} \times \ \mathbf{e}_{\rm z})$$

If we define the conductivity tensor σ as the inverse of ρ,

$$\sigma = \begin{pmatrix} \sigma_{xx} & -\sigma_{yx} \\ \sigma_{yx} & \sigma_{xx} \end{pmatrix},$$

one obtains

$$\sigma_{xx} = \frac{\rho_{xx}}{\rho_{xx}^2 + \rho_{yx}^2} \quad \text{and} \quad \sigma_{yx} = \frac{\rho_{yx}}{\rho_{xx}^2 + \rho_{yx}^2} \ ,$$

and then the equation of motion becomes

$$\mathbf{v}_{\rm T} = \frac{B}{n_s e}(\sigma_{yx}\mathbf{v}_{\rm L} - \sigma_{xx}\mathbf{v}_{\rm L} \times \mathbf{e}_{\rm z}) \ .$$

We see that, even in absence of complex situations such as pinning and vortex-vortex interactions, the simplest equation of motion (8.1) of a single vortex has terms that will contribute to the Hall effect : one gets

$$\sigma_{yx}^v = \frac{n_s e}{B} \ \frac{K_2}{K_1} \tag{8.3}$$

for the vortex contribution to the Hall conductivity. The Hall component of the electric response of a type II superconductor is therefore an integral part of the vortex dynamics, and should not be neglected in the analysis of resistivity measurements. A complete picture of the vortex response can indeed only be obtained from both longitudinal and transverse (Hall) components of the resistivity. Of course, the longitudinal resistivity ρ_{xx} represents by far the main part of the vortex motion, since the Hall angle, defined by

$$\tan \theta_H = \rho_{yx}/\rho_{xx} \tag{8.4}$$

is experimentally usually very small (of the order of 10^{-1} to 10^{-2}). However, there are some features in the vortex dynamics that are only observable in the Hall response. But the Hall-effect is not as simple as predicted by the classical models [186, 238], where the classical models of vortex motion predict that the superconducting and normal states will have the same Hall sign, and thus cannot explain this anomaly. In the superconducting state no generally expected theory to explain the Hall-effect exists; it remains controversial even after over 40 years of research on the subject. For example, as we have mentioned before, some experiments [231, 232, 233, 236] show that the sign of the Hall effect can actually reverse as the temperature is swept down through the region of the transition temperature T_c at lower magnetic fields or as the magnetic field is swept down through the region of the upper critical field B_{c2}. Some predict a Hall sign reversal below T_c caused by pinning effects [242], others argue that the anomaly cannot be due to pinning [243, 244], whilst others even predict no sign reversal at all [186]. In the mixed state, the sign reversal of the Hall resistivity has been attributed to anomalous vortex motion [245], superconducting fluctuations [230], or to a difference between charge densities in the core and far outside the vortices [246]. Despite many efforts, there remains a significant lack of understanding about the mechanism responsible for the anomalous Hall effect. Even the basic question of whether the sign change is due to the intrinsic property of vortex dynamics or some extrinsic property like pinning is unsolved.

A remarkable aspect of the mixed-state Hall effect is the scaling behavior between the Hall resistivity ρ_{yx} and the longitudinal resistivity ρ_{xx}. Luo et al. [247] have discovered a striking power-law behavior between their Hall effect and resistivity data on $YBa_2Cu_3O_{7-\delta}$ thin films. At fixed field, they found that $\rho_{yx} = A\rho_{xx}^{\beta}$

with β=1.7. Later scaling relations have also been observed in single crystals of $YBa_2Cu_3O_{7-\delta}$ [248] and $Bi_2Sr_2CaCu_2O_8$ [249] and in films of $Tl_2Ba_2CaCu_2O_8$ [232, 250, 251] and $HgBa_2CaCu_2O_6$ [233]. However, the reported values of the scaling exponent β are quite scattered, the highest value being $\beta = 2$, whereas values as low as 0.8 can be found [252].

Another interesting feature concerning the Hall effect of HTSCs is the universal temperature dependence of the cotangent of the Hall angle, ($\cot\theta_H \sim T^2$), in the normal state [253, 254]. Many models have been proposed to explain this behavior. Anderson's Luttinger-liquid model [253] seems to be one of the most popular, being supported by various studies. In this model the unconventional Hall effect is explained by the assumption of two different scattering rates, a transport scattering time and a Hall (transverse) scattering time. Anderson has proposed a non-Fermi liquid (Luttinger-Liquid) theory for describing the electronic properties or anomalous features of transport data of the HTSCs [253]. Within this theoretical picture, the spin−charge separation in the Cu-O planes into spinons and holons results in two different relaxation rates, a longitudinal transport relaxation rate τ_{tr}^{-1} related to the holon scattering and a transverse Hall relaxation rate τ_H^{-1} related to the spinon scattering. The normal state transport of the spin-charge separation state exhibits the following properties under optimal conditions: the longitudinal resistivity is linearly temperature-dependent ($\tau_{tr}^{-1} \sim T$) and the Hall effect involves a second scattering rate which leads to a T^2 dependence of the Hall angle ($\tau_H^{-1} \sim T^2$), resulting in the Hall coefficient $R_H \sim \rho_{xx} \tan\theta_H / B$.

In the most cases a clear $1/T$ dependence of the Hall coefficient was found for HTSCs. However, recently, virtually T independence of R_H (as in conventional metals) at moderate temperatures has been reported by Ando et al. in underdoped samples [255]. Together with a quadratic temperature dependence of the in plane resistivity, the same T^2 dependence of the normal state Hall angle results.

In this study, systematic measurements on the Hall effect as a function of the temperature on magnetic fields up to 12 T in epitaxial $(Hg_{0.9}Re_{0.1})Ba_2CaCu_2O_{6+\delta}$ (HgRe-1212) HTSC thin films were reported. The measurements of the longitudinal resistivity were performed simultaneously. The results have been published in 2004 [256]).

8.2 Experimental setup and procedures

The films ($d \approx 2500$ Å) were prepared by pulsed laser deposition onto (100) aligned $SrTiO_3$ substrates followed by post-annealing, and possess critical current densities $\approx 1.2 \times 10^7$ A/cm^2 at 5 K, $\approx 2 \times 10^6$ A/cm^2 at 77 K, and $T_c = 124$ K (resistive midpoint). After preparation and initial characterization, the films were patterned to a 9-probe geometry with strip dimensions of 700 μm $\times$ 220 μm (upper inset in Fig. 8.2) by photolithography and wet etching. Pads 3 and 5 or 4 and 6 were used to measure the in-plane or longitudinal resistivity ρ_{xx} and pads 5-6 were used to measure the transverse resistivity ρ_{yx}, while the current was applied between contacts 1 and 2 ($I \parallel ab$-plane). The geometry allows simultaneous measurements of the longitudinal or (magneto-)resistivity and the Hall effect (we take $\mathbf{B}\|\mathbf{z}\|\mathbf{c}$ and $\mathbf{J}\|\mathbf{x}$). The experiments were performed in a ^{4}He system, with variable temperature insert (VTI) cryostat. A superconducting magnet provided magnetic fields up to 12 T. The sample is placed in the main chamber of the ^{4}He system. Experiments were carried out in magnetic fields ranging from 0 to 12 T. According to the sample dimensions, a current of I_x = 0.1 mA corresponds to a current density $\mathbf{J}$ of about 180 A/cm^2. Since it is practically impossible to have a contact geometry such that the Hall probes are perfectly face to face along the width of the sample, the Hall signal will invariably contain a component of magnetoresistance which, in certain cases, can even hide interesting features of the Hall effect. This problem of the spurious effects due to Hall contacts misalignments or to inhomogeneous current flow is overcome by measuring the magnetoresistance, which is symmetric in the B field, and the Hall resistance, which is asymmetric in the B field, for both magnetic field orientations at a given temperature, such that the longitudinal contribution can be subtracted from the total voltage measured, leaving only the desired Hall contribution, i.e., $\rho_{yx} = [\rho_{yx}(+B) - \rho_{yx}(-B)]/2$.

8.3 Results

8.3.1 Temperature dependence of Hall resistivity

The longitudinal resistivity ρ_{xx} of $(Hg_{0.9}Re_{0.1})Ba_2CaCu_2O_{6+\delta}$ thin films measured in the temperature interval 30 K $< T <$250 K in different magnetic fields up to

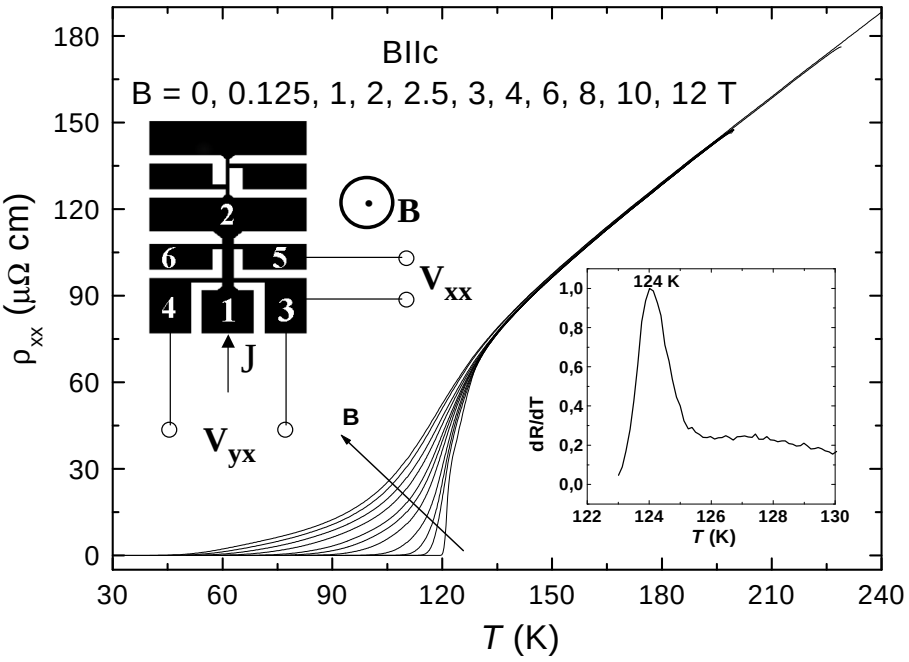

Figure 8.2: *Longitudinal resistivity for* $(Hg_{0.9}Re_{0.1})Ba_2CaCu_2O_{6+\delta}$ *thin films under applied magnetic fields from 0 to 12 T. The upper inset is a schematic diagram of the Hall bar pattern for Hall measurements. The lower inset illustrates the determination of* T_c *as the maximum of the temperature derivative of the resistivity.*

12 T is shown in Fig. 8.2. The data reveal no significant field dependence in the normal state. The critical temperature, determined at the maximum of the temperature derivative of the resistivity, is T_c=124 K at zero applied field (lower inset in Fig. 8.2). The simultaneously measured ρ_{yx}-data is shown in Fig. 8.3-a. In the normal state ρ_{yx} is proportional to the magnetic field, and positive at all temperatures (Fig. 8.3-a), indicating that conduction is due to hole-like carriers as in other HTSCs [257]. Figure 8.3-b shows the corresponding plot of ρ_{yx} in the mixed state on magnified scales so that the double sign reversal can be observed. Below T_c, ρ_{yx} is negative at lower fields (B $\leq$ 2.5 T), turning positive with increasing field. As can be seen in Fig. 8.3-b, the Hall sign change occurs in a limited range, while it cannot be observed at high magnetic fields (B $>$ 2.5 T). Though the anomaly is still observable, it is too small to induce a sign reversal. The negative resistivity is present around the critical temperature and in low fields only. The sign change of the Hall effect in the mixed state has been observed

in strongly anisotropic materials [258, 259, 260] and also in the newly discovered superconductor MgB_2 [261]. Even though all the materials cited here show a Hall anomaly, the sign change occurs only in some regime and it always disappears at high enough magnetic fields. In Dorsey's model [262, 263], the negative Hall resistivity in the mixed state is attributed to the hydrodynamic (Magnus) force on the body of the vortex which is opposite to the direction of the Lorentz force. In the time dependent Ginzburg-Landau theory the total conductivity σ_{yx} consists of two components: one is from the quasiparticle excitation and the other from the vortex motion. It was suggested that the sign of ρ_{yx} depends on the competition of a positive term and a negative term of the Hall conductivity.

In high-T_c cuprates, the Hall coefficient is considered to be controlled by both the transport scattering rate τ_{tr}^{-1} and a transverse or Hall scattering rate τ_H^{-1} [264], and it has a temperature dependence $R_H = \rho_{xx}\,\tan\theta_H/B \propto \tau_H/\tau_{tr}$ [265]. The observed temperature dependence of the Hall coefficient R_H is well known for other cuprate families [266] and is also observed in poly-crystalline Hg-1212 samples with a purity of 85 %. The temperature dependence of the Hall resistivity ρ_{yx} of $(Hg_{0.9}Re_{0.1})Ba_2CaCu_2O_{6+\delta}$ thin films in the normal state for the magnetic fields up to 12 T is plotted in Fig. 8.4. As expected and shown in Fig. 8.4, the normal Hall resistivity ρ_{yx} varies inversely with the temperature. It shows that ρ_{yx} is strongly temperature dependent at high magnetic fields which is not the case at very low magnetic fields. In high temperature superconductors, it was found that ρ_{yx} is linearly dependent on $1/T$ which is a remarkable and puzzling property. In the temperature interval 140 K $< T <$ 200 K, the data of the Hall resistivity ρ_{yx} of the present $(Hg_{0.9}Re_{0.1})Ba_2CaCu_2O_{6+\delta}$ thin film are fitted well by

$$\rho_{yx}(\mu\Omega\,\mathrm{cm}) = BR_H = B\frac{\mathrm{A}}{T+\mathrm{B}} \tag{8.5}$$

where and A and B are constants. The temperature and magnetic field given in units of K and T, respectively. The fitting results are illustrated in Fig. 8.4 as thin solid lines. We obtain A=35.54 ($\mu\Omega$ cm K T^{-1}) and B=104.14 ($\mu\Omega$ cm K T^{-1}).

The Hall coefficient R_H of $(Hg_{0.9}Re_{0.1})Ba_2CaCu_2O_{6+\delta}$ thin films is calculated from the relation $R_H = \rho_{yx}/B$. At different magnetic fields, checks were made in the normal state to ensure that the Hall coefficient was linear in applied magnetic fields. The measured R_H-data is shown in Fig. 8.5. Figure 8.5 shows that R_H

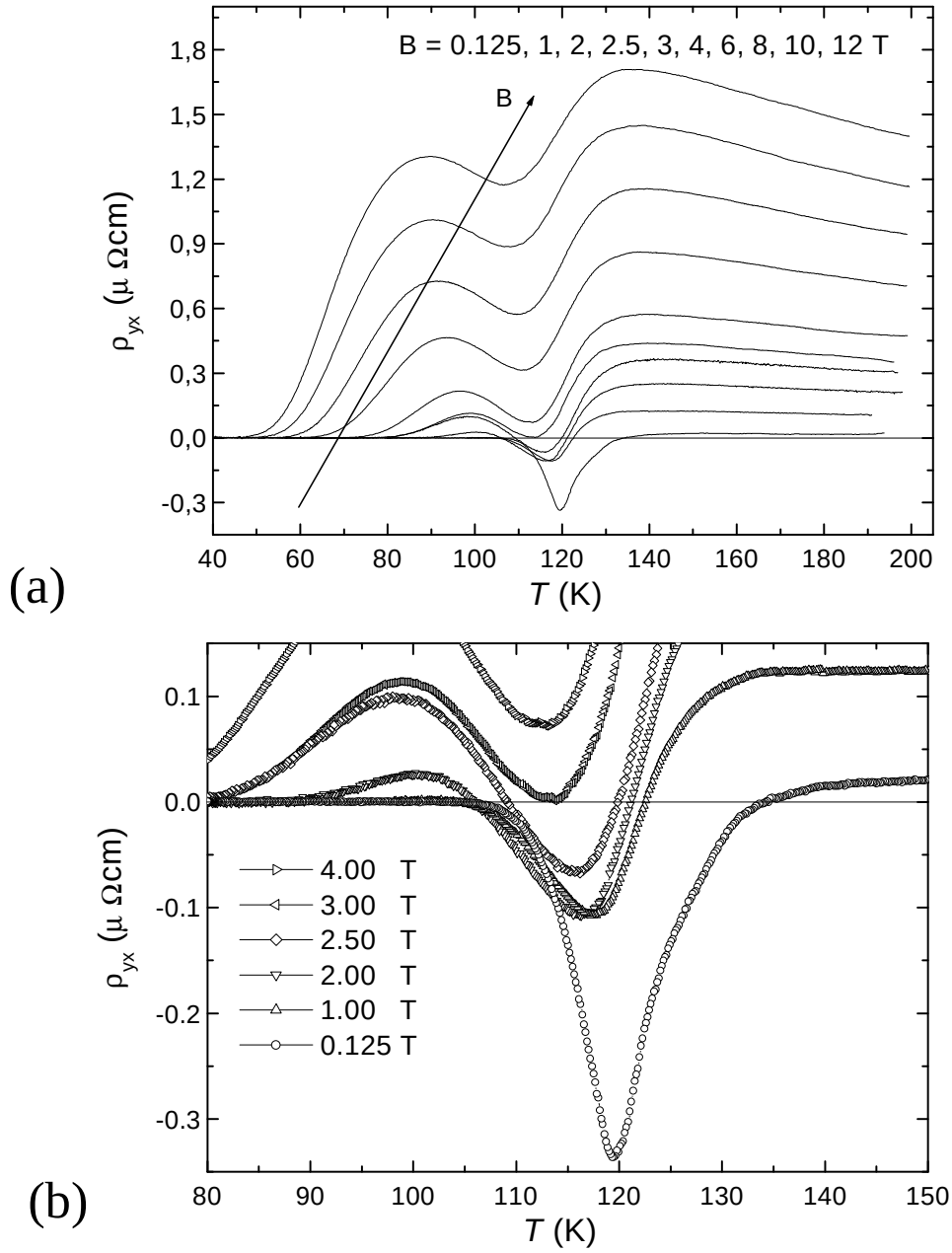

Figure 8.3: *Hall resistivity ρ_{yx} as a function of temperature for the $(Hg_{0.9}Re_{0.1})Ba_2CaCu_2O_{6+\delta}$ thin films. In (a), overview of the measured ρ_{yx}-data for both normal and superconducting states is given. The applied magnetic fields are indicated. (b) Corresponding plot of ρ_{yx} on magnified scales so that the sign reversals can be observed.*

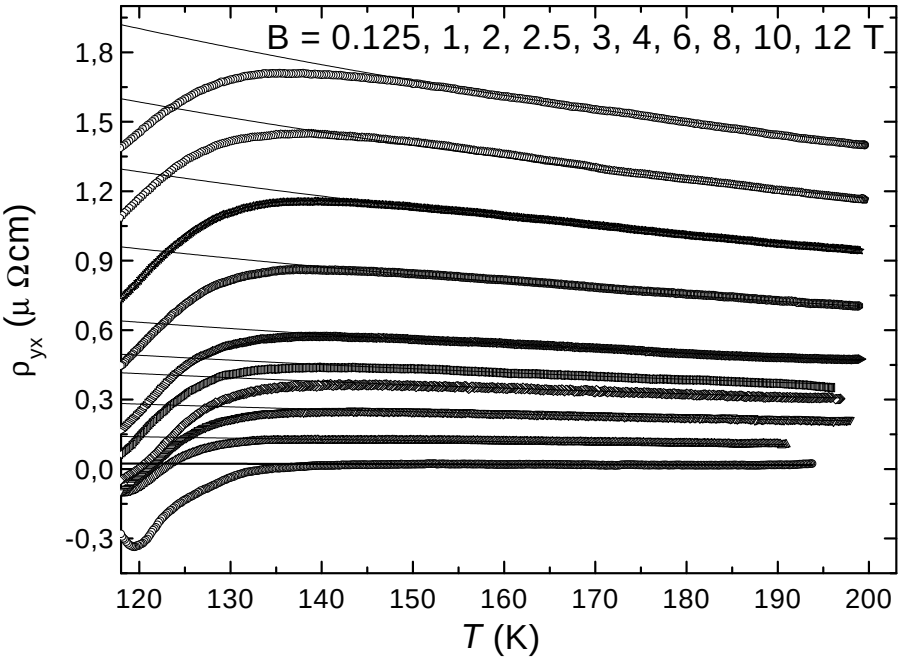

Figure 8.4: *Hall resistivity ρ_{yx} as a function of temperature for $(Hg_{0.9}Re_{0.1})Ba_2CaCu_2O_{6+\delta}$ thin films. The fitted curves correspond to $\rho_{yx} = R_H B$, where R_H is given by equation (8.5).*

reveals strong T dependence in both the normal and superconducting states. Figure 8.5-top demonstrates that R_H is positive at all temperatures for $B > 3$ T, where above T_c, R_H is positive and decreases with increasing temperature. The Hall coefficient R_H increases as the temperature decreases, and then drops sharply as the superconducting transition temperature is approached. Figure 8.5 also demonstrates that the T_c (onset) values obtained from the Hall measurements are in agreement with those from the magnetization and the resistivity measurements. In the theoretical model proposed by Anderson [264], the temperature dependence of the Hall coefficient in the normal state is expected to vary as

$$R_H^{-1} = aT + b \tag{8.6}$$

where a and b are temperature-independent constants. In the inset of Fig. 8.5-top, we plot the temperature dependence of the inverse Hall coefficient R_H^{-1} at B= 6 T and 12 T. Interestingly, R_H^{-1} varies approximately linearly with T at all

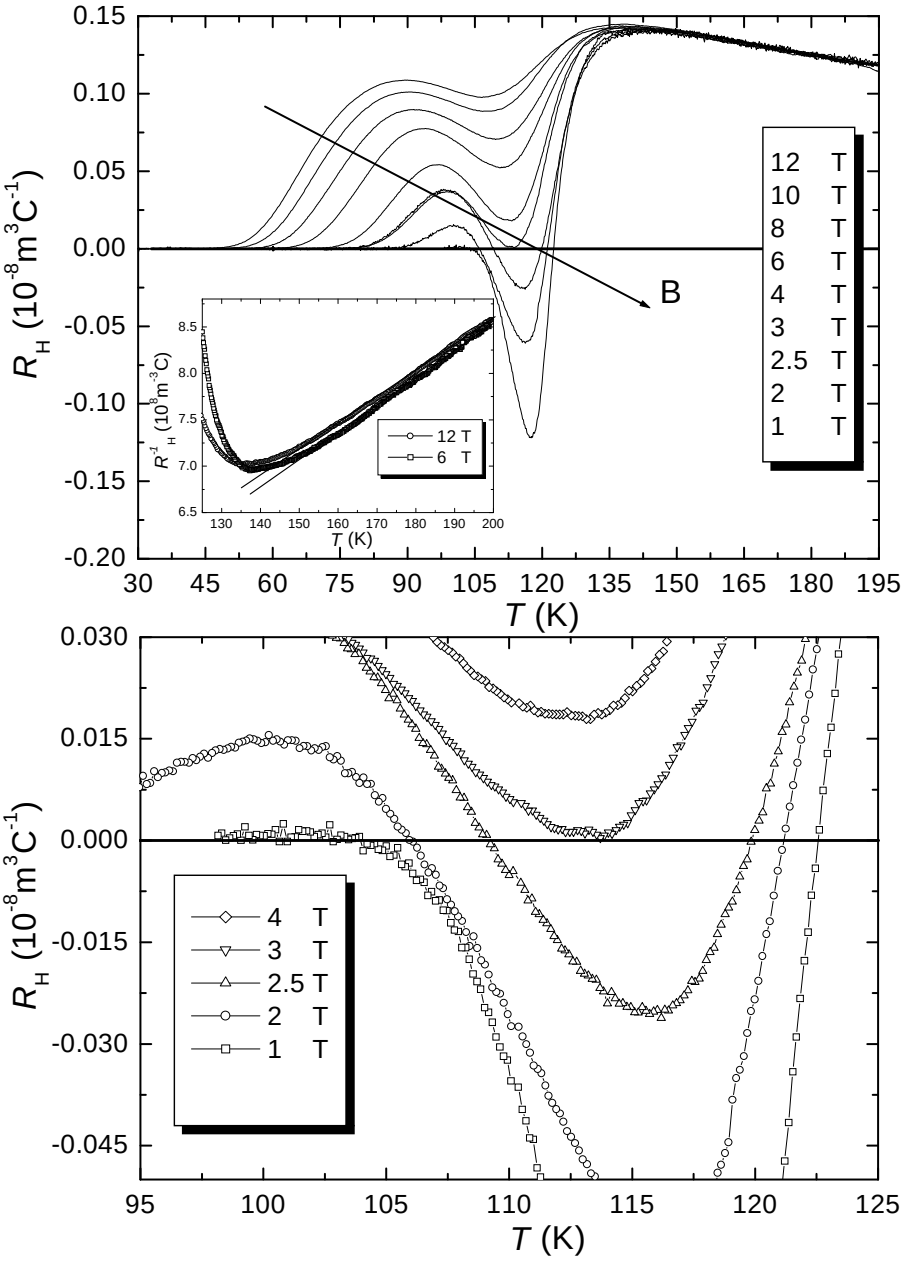

Figure 8.5: *Temperature dependence of the Hall coefficient R_H of the $(Hg_{0.9}Re_{0.1})Ba_2CaCu_2O_{6+\delta}$ thin film for various magnetic fields B up to 12 T (top) and an enlarged version for the low-temperature region (bottom), where the sign reversal of R_H occurs for $B < 4$ T. The inset in the upper figure shows the temperature dependence of the inverse Hall coefficient R_H^{-1} for magnetic fields B 6 and 12 T. The thin solid lines are fits to experimental data using equation (8.6).*

temperatures in the normal state. The fitting results are illustrated in the inset of Fig. 8.5-top as the thin solid lines. The Hall coefficient R_H gradually deviates from the linear T dependence in the mixed-state. Figure 8.5-bottom shows the behavior of R_H in the mixed state. Below T_c, R_H reverses its sign at lower fields, where R_H decreases rapidly and changes sign from positive to negative. The negative sign Hall anomaly increases significantly when the magnetic field is reduced below 4 T. After reaching a minimum R_H, it increases again until zero is approached. The general behavior is qualitatively the same as that observed in hole-doped high-T_c cuprates.

8.3.2 Temperature dependence of Hall angle

The Hall effect for the case of free flux-flow without pinning was analyzed using by Bardeen and Stephen [186] and Nozieres and Vinen [238] models. They described the occurrence of Hall effects in superconductors in terms of the forces presented above in sec. 8.1. In addition, they predicted the Hall angle to remain the same as that in the normal state at a field equal to that in the core. Both groups derived the same flux-flow resistivity, $\rho_{xx} = \rho_n \frac{B}{B_{c2}}$, where ρ_n is the normal resistivity; however, they obtained different Hall resistivities, $\rho_{yx} = (\frac{eB}{m})\tau_H \rho_n \frac{B}{B_{c2}}$ for the Bardeen and Stephen model and $\rho_{yx} = (\frac{eB}{m})\tau_H \rho_n$ for the Nozieres and Vinen model. Therefore, the magnetic field dependence of the Hall angle for BS and NV model is given by

$$\tan\theta_H = \frac{\rho_{yx}}{\rho_{xx}} = \left(\frac{eB}{m}\right)\tau_H = \omega_c \tau_H, \tag{8.7}$$

for the Bardeen and Stephen model, with $\omega_c = eB/m$, and

$$\tan\theta_H = \frac{\rho_{yx}}{\rho_{xx}} = \left(\frac{eB_{c2}}{m}\right)\tau_H = \omega_{c2} \tau_H, \tag{8.8}$$

for the Nozieres and Vinen model, with $\omega_{c2} = eB_{c2}/m$, where τ_H is the transverse Hall relaxation time. The Nozieres and Vinen model reach the same longitudinal resistivity as the Bardeen and Stephen model, and have a Hall effect B_{c2}/B times larger. If viewing vortex dynamics in real superconductors as that of independent vortices, that is, no correlation among vortices, the NV work would predict a large Hall angle. Experimentally, however, the Hall angle is usually small. More

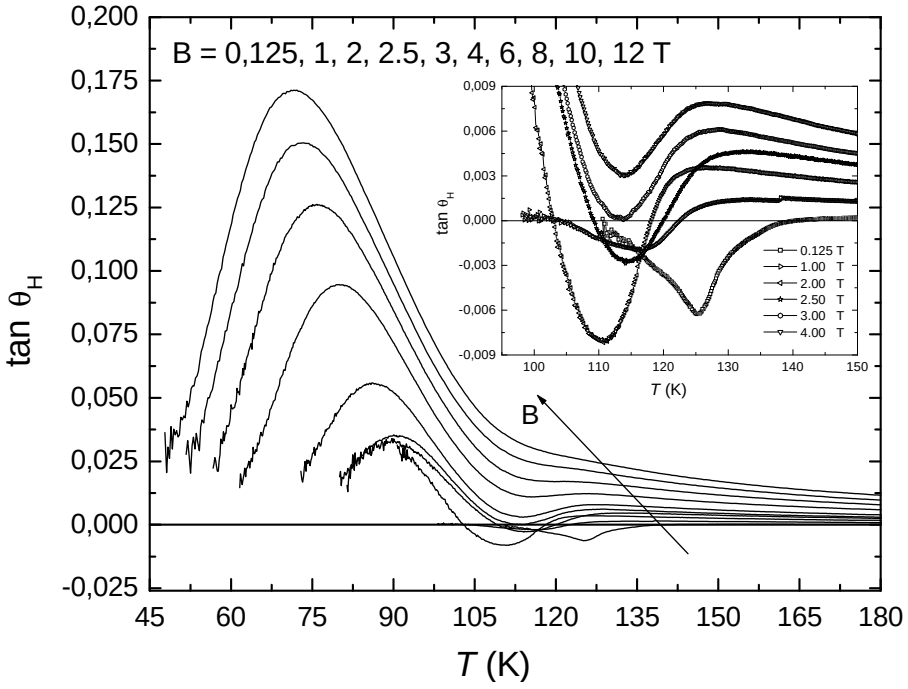

Figure 8.6: *Temperature dependence of the tangent of the Hall angle in magnetic fields up to 12 T for the* $(Hg_{0.9}Re_{0.1})Ba_2CaCu_2O_{6+\delta}$ *thin film.*

puzzling is that the Hall angle can change sign, sometimes even more than once. The data of the temperature dependence of the tangent of the Hall angle ($\tan\theta_H$) measured on a $(Hg_{0.9}Re_{0.1})Ba_2CaCu_2O_{6+\delta}$ film is shown in Fig. 8.6. The tangent of the Hall angle was computed as the ratio of the Hall resistance to the longitudinal resistance $\tan\theta_H = \rho_{yx}/\rho_{xx}$ as discussed in sec. 8.1. Hall-angle measurements at different fields produce similar curves displaced vertically from each other. The Hall angle is a measure of the direction in which the vortices are moving. At magnetic fields $B \leq 2.5$ T, $\tan\theta_H$ changes from positive above T_c to negative below T_c. As the temperature decreases, a dip and then a peak at slightly lower temperatures occur. For fields above 1 T, the dip is located nearly field-independent at 114 K, the peak shifts to lower temperatures with increasing fields. This is in agreement with data in Hg-1223 films [236, 267], but has not been observed in data on the highly anisotropic Bi- and Tl-systems [232, 251], where the peak is located at a constant temperature as fields increase.

The cotangent of the Hall angle ($\cot\theta_H$), which is defined as the ratio be-

tween the longitudinal resistivity ρ_{xx} (determined by the transport scattering time, i.e., $\rho_{xx} \propto \tau_{tr}^{-1} \propto T$) and the transverse resistivity ρ_{yx} (determined by the transport scattering time and the transverse or Hall scattering time, i.e., $\rho_{xy} \propto \tau_{tr}^{-1}\tau_H^{-1} \propto T^3$) was calculated at different fields B:

$$\cot \theta_H = \rho_{xx}/\rho_{yx} = \omega_c^{-1}\tau_H^{-1}. \tag{8.9}$$

The cotangent of the Hall angle becomes one of the essential quantities since it is dependent on τ_H only and exhibits in the normal state (above 130 K) a quadratic temperature dependence as was expected by Anderson [253], i.e.,

$$\cot \theta_H = \alpha T^2 + \beta, \quad T > T_c \tag{8.10}$$

where α and β are temperature-independent constants. The parameter α is related to the spinon bandwidth W_s ($\alpha \propto W_s^{-1}$) and β is an additive term due to magnetic impurity scattering.

The T^2 dependence of cot θ_H for $(Hg_{0.9}Re_{0.1})Ba_2CaCu_2O_{6+\delta}$ thin films is shown in Fig. 8.7. The transition from the mixed to the normal state may be observed in the abrupt drop of cot θ_H just below the transition temperature. It should be noted that in fields ranging from 1 to 12 T the data fall on approximately straight lines in the temperature interval between 130 and 200 K. The solid lines in Fig. 8.7 represent fits to Eq. (8.10). When looking to the linear part in all the curves of Fig. 8.7, we clearly observe a systematic evolution with varying the magnetic field. First, the slope $\alpha = d(\cot\theta_H)/d(T^2)$ decreases systematically with increasing the magnetic field, and second the intercept $\beta = \cot\theta_H(T = 0)$ becomes nonzero for fields > 4 T. However, the parameters change from $\alpha = 1.9304 \times 10^{-2}$ K^{-2} and β = -0.42363 $\times 10^2$ for B = 1 T to $\alpha = 0.27931 \times 10^{-2}$ K^{-2} and $\beta = -0.04561 \times 10^2$ for B = 12 T. The parameter β is a measure of the in-plane impurity scattering rate. All of the previous Hall effect experiments reveal a unified picture of the Hall effect in various high-T_c cuprate systems. While the increase of β corresponds to a reduction of mobility, the change of α was attributed to the variation in the true carrier density [268, 269]. The slope calculated for a magnetic field of 8 T, $\alpha = 0.42802 \times 10^{-2}$ K^{-2}, is in agreement with data from Chien [254] in a Zn-doped single-crystal $YBa_2Cu_{3-x}Zn_xO_{7-\delta}$, where $\alpha = 0.51100 \times 10^{-2}$ K^{-2} obtained also for $B = 8$ T. A relation between the slope α and the bandwidth

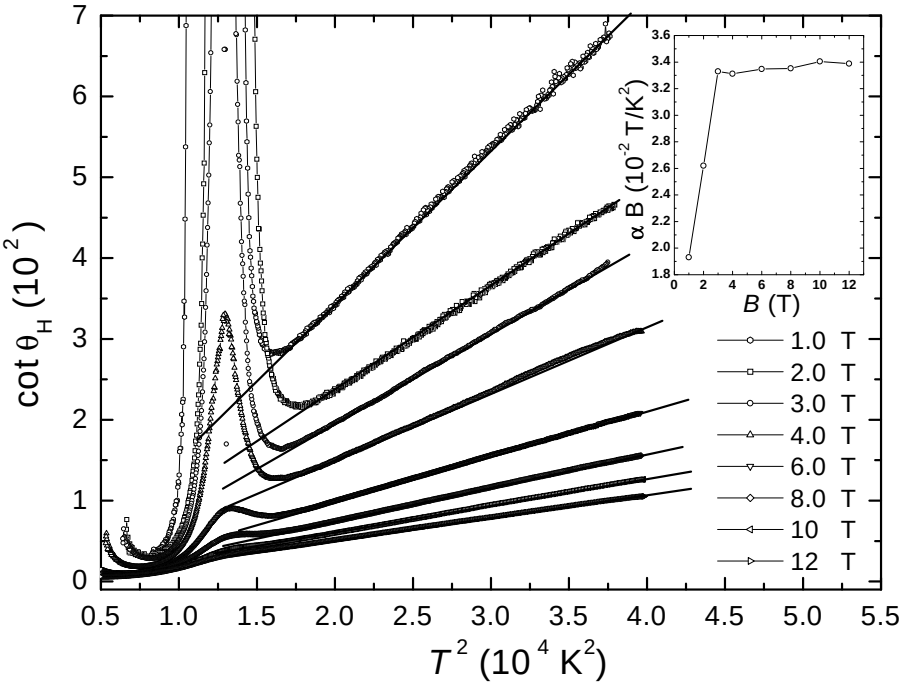

Figure 8.7: *T^2 dependence of the cotangent of the Hall angle in fields ranging from 1 to 12 T for the $(Hg_{0.9}Re_{0.1})Ba_2CaCu_2O_{6+\delta}$ thin film. The solid lines show fits of the data to cot $\theta_H = \alpha T^2 + \beta$. The inset illustrates the field dependence of the calculated value αB.*

W_s of the spin carriers (spinons) was derived by Chien, Wang, and Ong [254]:

$$\alpha B = \frac{k_B^2 \phi_0 n_H}{W_s^2} \tag{8.11}$$

where k_B is the Boltzmann constant, $\phi_0 = h/e$ the normal flux quantum, W_s the bandwidth for spin-spin scattering, and n_H the two-dimensional spin carrier density. From the experimental data the value of W_s according to the equation of Chien (Eq. 8.11) was calculated. For this purpose the result of the fit, $\alpha = 4.32 \times 10^{-3} 1/\mathrm{K}^2$ at 8 T, was used. This result in $W_s = 1543$ K, which is in agreement with the value found by Chien [254] of 830 K and the expected bandwidth of $W_s = 1400$ K, according to the respective Anderson Theory [253, 254]. In fields above 2 T and in the normal state, it should be noted that the calculated value αB from Fig. 8.7 is constant as inferred in Eq. (8.11) (see inset in Fig. 8.7).
The universality of the quadratic temperature dependence of the cotangent of

the normal state Hall angle has been recently discussed by Yoichi Ando et al. [255]. There the authors found the same T^2 dependence of the normal state Hall angle, however, resulting essentially from a temperature independent Hall coefficient R_H and a quadratic temperature dependence of the in plane resistivity. They investigated underdoped $YBa_2Cu_3O_{7-\delta}$ and $La_{2-x}Sr_xCuO_4$. From their measurements they conclude that the relaxation rate of the quasiparticles on the Fermi arc, a small portion of the Fermi surface (FS) near the Brillouin-zone diagonals, changes proportional to T^2, which incidentally is the same as the behavior of conventional Fermi liquids. As temperature or doping is increased more carriers contribute. However, for the optimally doped case investigated here the temperature dependence of the Hall effect is still puzzling.

8.3.3 Scaling behavior in the mixed state Hall effect

Another striking feature is also observed in the Hall behavior of $(Hg_{0.9}Re_{0.1})Ba_2Ca Cu_2O_{6+\delta}$ thin films. In the decreasing part of the data, at low temperature, the data follows the scaling relation $\rho_{yx} = A\rho_{xx}^{\beta}$, as first noted by Luo [247]. In Fig. 8.8, $|\rho_{yx}|$ is plotted vs. ρ_{xx} in double logarithmic scale for constant magnetic fields up to 12 T. The scaling exponent β in $\rho_{yx} = A\rho_{xx}^{\beta}$ significantly increases from $\beta = 1.0$ to 1.7 during increasing the field from 1 to 12 T (see lower inset in Fig. 8.8), which is different from reported data in highly anisotropic systems, where $\beta \approx 2$ has been observed for $Bi_2Sr_2CaCu_2O_{8\delta}$ crystals [249] and $Tl_2Ba_2Ca_2Cu_3O_{10+\delta}$ films [232, 250, 251]. Other similar studies resulted in β = 1.5-2.0 for $YBa_2Cu_3O_{7-\delta}$ crystals [248], $YBa_2Cu_3O_{7-\delta}$ films [247], and $HgBa_2CaCu_2O_y$ films [233, 267]. Even more interestingly, $\beta \approx 1$ was observed in the $HgBa_2CaCu_2O_y$ thin films [270] after heavy-ion irradiations. The scaling behavior between ρ_{yx} and ρ_{xx} has been discussed in a number of models. Theoretically, Dorsey and Fisher [262, 263] developed a scaling theory near the vortex-glass transition with an exponent β= 1.7 in a three-dimensional vortex system with weak disorder and they explained the experimental results of Luo et al. for $YBa_2Cu_3O_{7-\delta}$ films [247]. In the model, the exponent β is universal, but the sign of the Hall effect is material specific and possibly related to microscopic pairing processes. A phenomenological model was put forward by Vinokur et al. [243]. According to their model, the scaling behavior of the Hall resistivity in the mixed state of HTSCs is a general feature of any vortex state in the presence

of the quenched disorder and thermal noise. They proposed a universal Hall scaling theory based on a force balance equation where the Lorentz force $\mathbf{f}_{\mathrm{L}}$ acting on a vortex is balanced by the usual frictional force -$\eta\mathbf{v}_{\mathrm{L}}$ and the Hall force $\vartheta\mathbf{v}_{\mathrm{L}} \times \mathbf{e}_{\mathrm{z}}$. When the Lorentz force $\mathbf{f}_{\mathrm{L}}$ exceeds the pinning force in region of constant current density $\mathbf{J}$, motion begins. The equation for the forces acting on the vortices in the absence of pinning is then

$$\eta\mathbf{v}_{\mathrm{L}} + \vartheta\mathbf{v}_{\mathrm{L}} \times \mathbf{e}_{\mathrm{z}} = \phi_0\mathbf{J} \times \mathbf{e}_{\mathrm{z}} \,, \tag{8.12}$$

with the the Lorentz force $\mathbf{f}_{\mathrm{L}} = \phi_0\mathbf{J} \times \mathbf{e}_{\mathrm{z}}$ balanced by the two velocity-dependent forces, $\mathbf{v}_{\mathrm{L}}$ being the average velocity of vortices, and $\mathbf{e}_{\mathrm{z}}$ being the unit vector along the vortex lines (in the direction of the magnetic field). The term on the right-hand side of Eq. (8.12) is the Lorentz force acting on the vortex line due to the presence of the transport current. The coefficient ϑ is related to the Hall angle, due to $\vartheta = \eta\tan\theta$, η being the usual viscous drag coefficient and ϑ the Hall drag coefficient. The vectors $\eta\mathbf{v}_{\mathrm{L}}$ and $\vartheta\mathbf{v}_{\mathrm{L}} \times \mathbf{e}_{\mathrm{z}}$ are mutually perpendicular as illustrated in in Fig.8.1.

In this model the Hall conductivity is independent of disorder and is directly linked to the microscopic processes determining the single vortex equation of motion. Using the force balance equation for a stationary moving vortex, Vinokur et al. argued that pinning just renormalizes the drag force term (the first term on the left-hand side of Eq. (8.12)), not affecting the second, Hall conductivity term. In their model the exponent β should be 2 and independent of the pinning strength. Their main results are that Hall conductivity $\sigma_{yx}(\approx \rho_{yx}/\rho_{xx}^2)$ does not depend on disorder and the scaling exponent β is exactly 2, which can be summarized as

$$\rho_{yx} = \frac{\Psi}{\phi_0 B}\rho_{xx}^2 \,, \tag{8.13}$$

where ϕ_0 is the flux quantum, and Ψ is a pinning independent parameter related to the Hall angle. The coefficient A introduced in the scaling relation $\rho_{yx} = A\rho_{xx}^{\beta}$ is related to Ψ via $A = \frac{\Psi}{\phi_0 B}$ if we let β be equal to 2. The result was consistent with the observed exponent in Bi-, Tl- and Hg-based superconductors only for the Hall data measured in high magnetic fields [249, 250, 267]. After this discussion about the $\beta = 2$ value of the exponent, now the experimental data leading to different results shall be discussed. First, one has to note that these values are usually lying between 1.4 and 1.8, quite often around 1.5 to 1.6 [248, 271, 272],

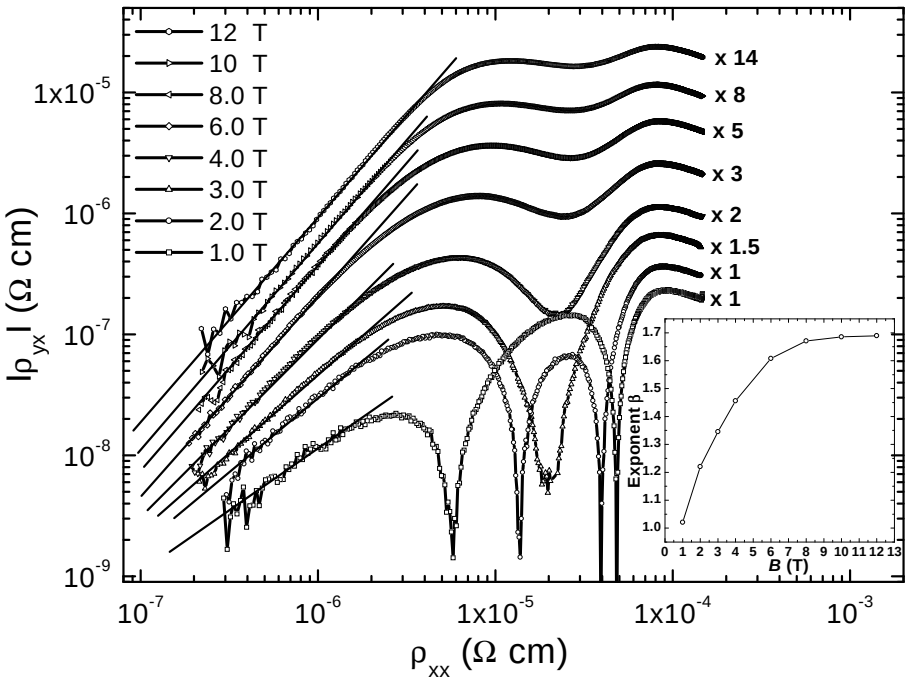

Figure 8.8: *Log-log plot of $|\rho_{yx}|$ vs. ρ_{xx} obtained by temperature sweeps for $(Hg_{0.9}Re_{0.1})Ba_2CaCu_2O_{6+\delta}$ thin films, for the fields up to 12 T. For clarity, the data are multiplied by different factors in order to obtained a shift along the vertical axis. The thin solid lines represent fits to the data according to $\rho_{yx} = A\rho_{xx}^{\beta}$. The inset illustrates the field dependence of the exponent β.*

but values as low as 0.8 can be found [252]. Please note that this scattering of data is apparently not related to the different compounds, but really seems to be the result of a sample dependence. Another important finding in some of these works is the field dependence of the exponent β, as observed in the inset of Fig. 8.8 for the $(Hg_{0.9}Re_{0.1})Ba_2CaCu_2O_{6+\delta}$ thin film. The same kind of behavior is also observed by other authors as already reported in the mixed-state Hall effect of twinned $YBa_2Cu_3O_7$ crystals [273]. Wang et al. [245] have proposed another phenomenological model. This modifies the exponent in such a way that $\beta = 1.5$ for strong pinning and $\beta = 2$ for weak pinning, and the Hall sign reversal is a pinning effect, which agrees with the results reported for YBCO crystals [273, 274], Hg-1212 films [233], and the data on the $(Hg_{0.9}Re_{0.1})Ba_2CaCu_2O_{6+\delta}$ thin films in this work.

8.3.4 Field dependences of the longitudinal resistivity, the Hall resistivity, and the Hall angle for $(Hg_{0.9}Re_{0.1})Ba_2CaCu_2O_{6+\delta}$ thin films

Figure 8.9 shows the magnetic-field dependences of the longitudinal resistivity ρ_{xx} and the Hall resistivity ρ_{yx} for $(Hg_{0.9}Re_{0.1})Ba_2CaCu_2O_{6+\delta}$ thin films at various temperatures. The longitudinal resistivity ρ_{xx} increases monotonically with increasing temperature. At higher fields and for $T \geq 90$ K, the Hall resistivities of $(Hg_{0.9}Re_{0.1})Ba_2CaCu_2O_{6+\delta}$ thin films has a nearly linear dependence on the field. The sign of the Hall resistivity in the low-field region near the transition temperature becomes negative, which is opposite to the positive sign of the Hall resistivity for the normal state. The inset in Fig. 8.9-bottom presents the Hall resistivities ρ_{yx} for $T \geq$90 K in the low-field region, where the sign reversal of the Hall resistivities ρ_{yx} occurs for $T = 110$ K and $T = 120$ K.
In Fig. 8.10, the tan θ_H as a function of the magnetic field up to 12 T is plotted. A crossover field B^* divides the tan θ_H curve into two parts having different slopes. In this figure, the arrow denotes the crossover field B^* for $T = 90$ K.

8.3.5 Temperature dependence of Hall conductivity

The Hall conductivity, which has been discussed in paragraph 8.1, is strictly related to vortex dynamics, hence the notation σ_{yx}^v. Although the equation of motion (8.1) corresponds to a hydrodynamic, mean-field description of the vortex contribution, the fluctuations might also be taken into account in this term, for example through a Ginzburg-Landau derivation. Aside from this vortex term, the total Hall conductivity also contains contributions from the delocalized excitations, expressed as the product of the normal state Hall conductivity σ_{yx}^n times the normal-like excited states fraction (1-g) (representing the normal fluid density) [240]. The equation for the total Hall conductivity is then

$$\sigma_{yx} = (1 - \mathrm{g})\, \sigma_{yx}^n + \sigma_{yx}^v\, (\mathrm{g})\ , \tag{8.14}$$

where σ_{yx}^v depends in general on the superconducting density g. From Eq. (8.1), the Hall conductivity can be decomposed into two parts, one being the delocalized quasiparticles contribution, seen as the normal fluid Hall effect, the other being the vortex flow Hall effect.

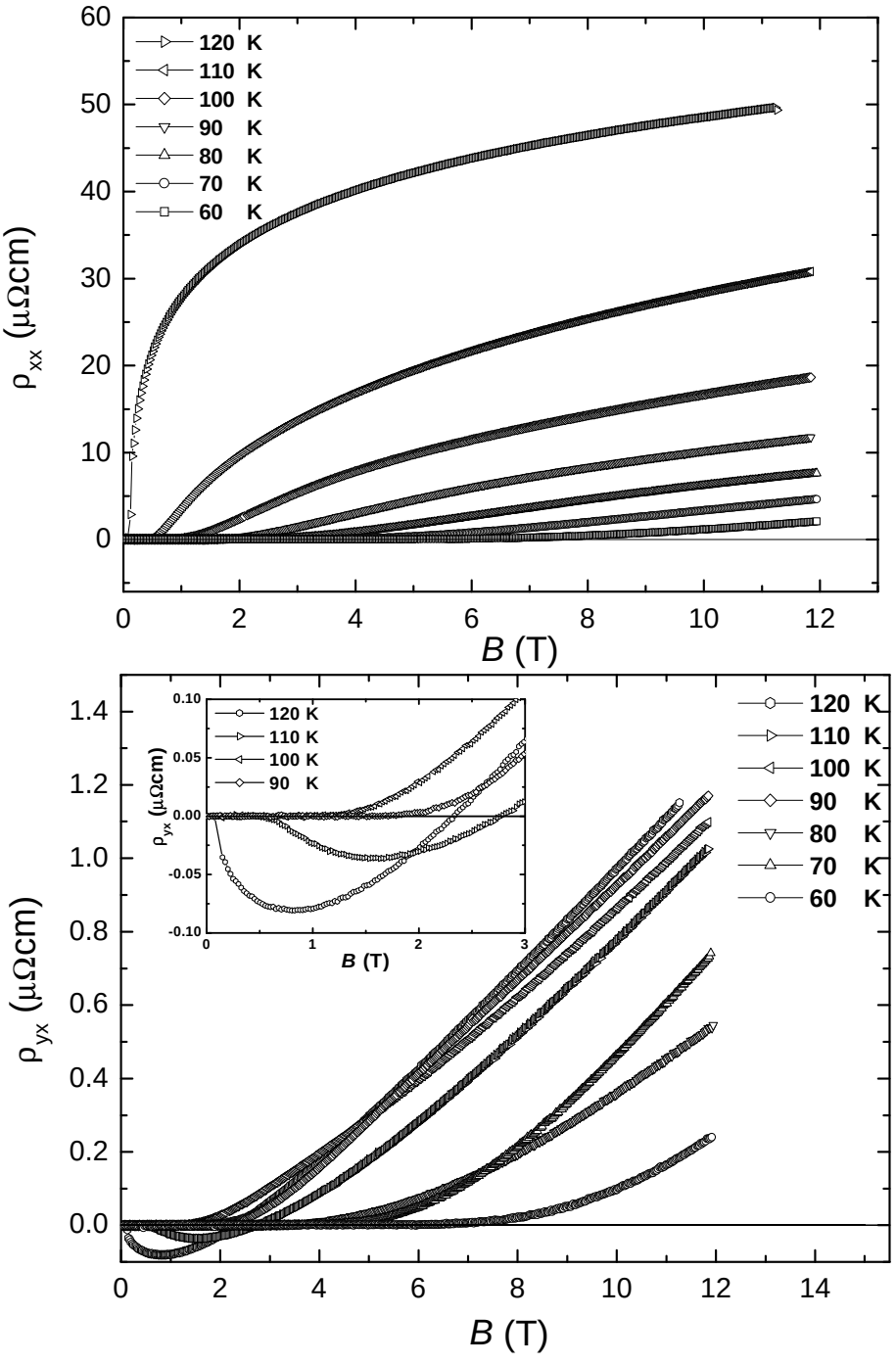

Figure 8.9: *The magnetic field dependences of ρ_{xx} (top) and ρ_{yx} (bottom) for $(Hg_{0.9}Re_{0.1})Ba_2CaCu_2O_{6+\delta}$ thin films. The inset in the lower figure is an enlarged version for the low-field region, where the sign reversal occurs for $T = 110$ K and $T = 120$ K.*

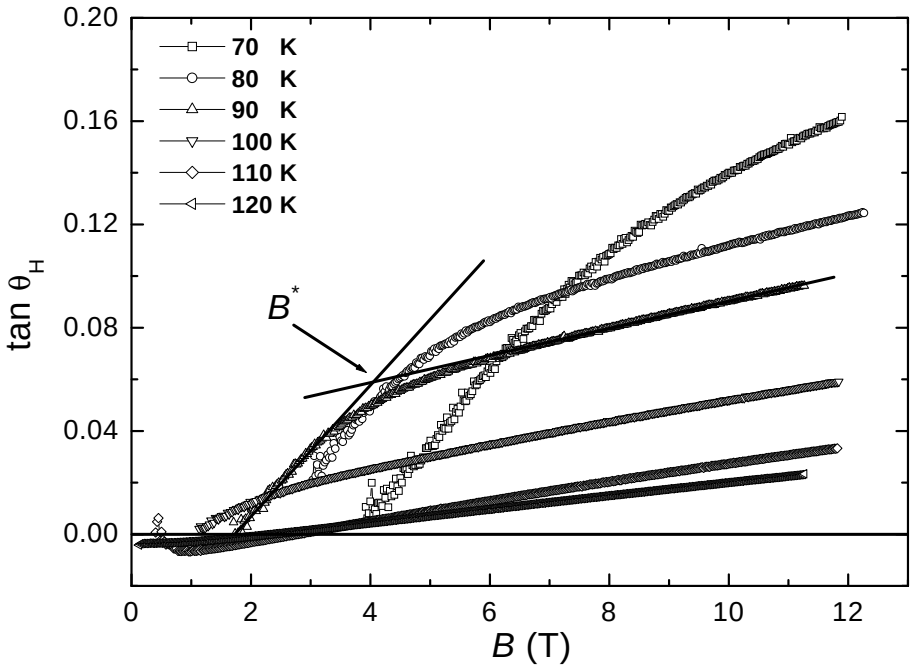

Figure 8.10: *Magnetic field dependence of the Hall angle in the* $(Hg_{0.9}Re_{0.1})Ba_2CaCu_2O_{6+\delta}$ *thin film for various temperatures. The arrow denotes the crossover field* B^* *for* $T = 90$ *K.*

Dorsey and co-workers [263, 275, 276], Kopnin, Ivlev, and Kalatsky [239] consider a time-dependent Ginzburg-Landau (TDGL) theory modified to take into account 2 mechanisms responsible for the Hall voltage in superconductors: the usual effect of the magnetic field on the normal current, and the vortex traction by the superflow. The time dependent Ginzburg-Landau (TDGL) theory has been shown to be quite successful in describing the Hall effect in the superconducting state [239, 263, 275, 276]. According to the TDGL theory, the vortex Hall conductivity σ_{yx}^{v} plays an important role in determining the Hall sign at low fields. For the BCS model of superconductivity, the contribution of the vortex traction is proportional to the energy derivative of the quasiparticle density of states. According to the theoretical results of their theory, the Hall conductivity can be expressed by two contributions. The first contribution due to the vortex motion is proportional to $1/B$ and is dominant in the low-field region. The second contribution, which originates from quasiparticles, is proportional to B. The Hall conductivity σ_{yx} in the superconducting state should be the sum of the two terms:

$$\sigma_{yx}(B) = \sigma^q_{yx} + \sigma^v_{yx} \ , \tag{8.15}$$

where σ^v_{yx} represents a superconducting contribution, arising from the motion of the magnetic vortices and superconducting fluctuations, and should be proportional to $1/B$. The second term on the right-hand side of Eq. (8.16), σ^q_{yx}, describes the contribution arising from the quasiparticles, normal carriers, inside and around the vortex core and denotes the normal (delocalized quasiparticles) component, written as $(1 - \mathrm{g})\ \sigma^n_{yx}$ in Eq. (8.14). This term has the same sign as the normal state and is proportional to B.
Accordingly, σ_{yx} should be of the form

$$\sigma_{yx}(B) = C_1/B \ + \ C_2 B \ , \tag{8.16}$$

where the coefficients C_1 and C_2 are independent of field B, but are expected to depend on the temperature T. Depending on details of the electronic structure of the materials, the coefficients C_1 and C_2 may have opposite signs and hence allow for a sign change of the total Hall conductivity [239, 263].
Equation (8.16) has been satisfyingly used to fit the experimental data in some cases [277, 278]. At low fields, σ_{yx} should be proportional to $1/B$, and such a field dependence has been observed by Samoilov et al. in $Tl_2Ba_2Ca_{n-1}Cu_nO_{2n+4+\delta}$ films [251]. Their results indicate that the C_2B term in Eq. (8.16) should be replaced by a field-independent term. However; this behavior is different from experimental results on $YBa_2Cu_3O_{7-\delta}$ which obey Eq. (8.16) at high fields [265]. In some materials, the equation above is not adequate to fit the data. Measurements on $YBa_2Cu_3O_{7-\delta}$ [265, 277, 279] have shown that the experimental data can be well described by Eq. 8.16 except for the low-field regime. Compared to $YBa_2Cu_3O_{7-\delta}$, besides the field dependent terms of Eq. (8.16), the total Hall conductivity contains an additional B-independent contribution C_3 in the high-field regime [251, 279, 280, 281]. Thus, the total Hall conductivity σ_{yx} is expected to add up to

$$\sigma_{yx}(B) = C_1/B \ + \ C_2 B \ + C_3, \tag{8.17}$$

the component C_3 is added for better fitting.

The Hall conductivities of $(Hg_{0.9}Re_{0.1})Ba_2CaCu_2O_{6+\delta}$ fully textured HTSC thin films are investigated for a magnetic field parallel to the c-axis and in the magnetic

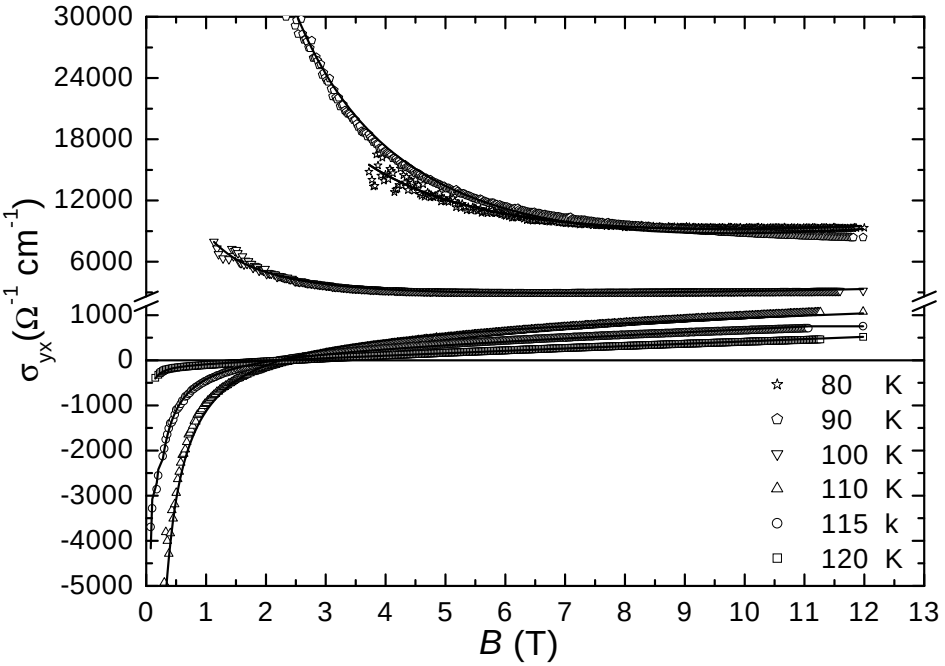

Figure 8.11: *The magnetic field dependences of the Hall conductivity at various temperatures as indicted for* $(Hg_{0.9}Re_{0.1})Ba_2CaCu_2O_{6+\delta}$ *thin films. Solid line represent a fit to the data as described in the text.*

fields up to 12 T. The motivation for doing this was to check whether the previous analysis of the field dependence of the Hall conductivity based on the TDGL theory was valid even at this high field. To determine the Hall conductivity first the Hall and longitudinal resistivities defined as $\rho_{yx} = E_y/J$ and $\rho_{xx} = E_x/J$, respectively were measured. The Hall conductivity is obtained by $\sigma_{yx} = \rho_{yx}/\rho_{xx}^2 + \rho_{yx}^2$. A plot of the magnetic field dependences of the Hall conductivity of $(Hg_{0.9}Re_{0.1})Ba_2CaCu_2O_{6+\delta}$ film at temperatures close and below $T_c = 124$ is shown in Fig. 8.11. The mixed-state Hall conductivity for these compounds is described by Eq. (8.17).

Analysis of the magnetic field dependences of the Hall conductivity over the whole mixed state region reveals that σ_{yx} contains a B^{-1} term that is negative near T_c and changes sign on cooling between 110 K and 100 K and a field-independent positive contribution. It may be noted that the experimental data can be well described by Eq. (8.17) for the low and high-field regime.

The fitting results, which are illustrated in Fig. 8.11 as solid lines, describe very well the whole set of data for σ_{yx} as a sum of these three components. The data are fitted well in all temperatures region by using Eq. (8.17) especially for 110 K and 120 K, indicating that the above theory describes very well the experimental data of $(Hg_{0.9}Re_{0.1})Ba_2CaCu_2O_{6+\delta}$ thin films. In this figure, the downward curves, as approaching zero field, show a sign reversal, but the upward curves do not. If the curve is downward, C_1/B is negative, but if the curve is upward, it is positive.

The first coefficient C_1 varies from -44 $T\Omega^{-1}cm^{-1}$ at 120 K to 15358 $T\Omega^{-1}cm^{-1}$ at 70 K. The second coefficient C_2 of the term linear in B shows a weak temperature dependence in the region of 90 K $\leq T \leq$ 120 K. This T dependence of C_2 is different from the cases of $YBa_2Cu_3O_{7-\delta}$ [277, 282] and of underdoped and slightly overdoped $La_{2-x}Sr_xCuO_4$ single-crystal thin films [280], in which C_2 increases rapidly below T_c with decreasing T. Harris et al. interpreted the rapid increase by the suppression of the quasiparticle scattering rate below T_c [282]. The third coefficient C_3 increases from 51 $\Omega^{-1}cm^{-1}$ to 700 $\Omega^{-1}cm^{-1}$ on cooling below T_c. But the present Re-doped Hg-1212 thin films shows the same behavior as reported for $HgBa_2CaCu_2O_y$ thin films near T_c [281].

Conclusions

Mercury superconductors possess excellent superconducting properties, even above 77 K. Critical current densities of the order 10^5 A/cm^2 at 77 K and irreversibility fields of $\mu_0 H_{irr}$ (100 K) = 0.5 T demonstrate the great application potential of these superconductor materials. This work studies the preparation, characterization, and electronic properties of thin films of the high-temperature superconductor $HgBa_2Ca_{n-1}Cu_nO_{2n+2+\delta}$. The synthesis of high-quality Hg-based cuprate films is one of the most difficult challenges in the synthesis of high T_c cuprates so far. The major difficulty stems from the high volatility of Hg and HgO.

The main goal of this thesis was to achieve a reliable technology for reproducible high quality thin film preparation by understanding the film growth mechanism, the phase formation, and the influence of different synthesis routes with cationic substitutions.

Fully textured $(Hg_{0.9}Re_{0.1})Ba_2CaCu_2O_{6+\delta}$ HTSC thin films were successfully prepared by pulsed laser deposition (PLD) of a precursor on (100)-oriented $SrTiO_3$ substrates and then followed by annealing in controlled mercury vapor. In this two-step process, mercury is provided to the enclosed sample through thermal evaporation. Conditions for reproducible film preparation have been found. Stable $Re_{0.1}Ba_2CaCu_2O_{6+\delta}$ precursor films were successfully used for the preparation of mercury films with a long-term stability of their superconducting properties. After deposition the substrates with the precursor films were sealed into quartz tubes sandwiched by a $(Hg_{0.9}Re_{0.1})Ba_2CaCu_2O_y$ pellet on the film side and a $Re_{0.1}Ba_2CaCu_2O_y$ pellet on the substrate side. The $(Hg_{0.9}Re_{0.1})Ba_2CaCu_2O_y$ pellet provides the Hg-atmosphere to transform the precursor film into the $(Hg_{0.9}Re_{0.1})Ba_2CaCu_2O_{6+\delta}$ film. The samples annealed in close proximity of the stoichiometric bulk pellet showed excellent superconducting characteristics with high reproducibility while those placed as little as a centimeter away were not super-

conducting at all. The magnetic susceptibility for as-prepared Hg-based cuprate thin films has a sharp onset near 120 K. The transition to the superconducting state, measured by a susceptibility measurement, remains stable without apparent changes during 14 months. The diffraction patterns indicate epitaxial texture in Hg,Re-containing HTSC thin films, corresponding to the tetragonal structure of space group P4/mmm and with lattice parameters a=3.85 Å and c=12.520 Å. The diffraction peaks were assigned to the (00ℓ) peaks from the Hg-1212 phase, which indicates that the c-axis of the film is perpendicular to the surface. The full width at half maximum (FWHM) of the rocking curve of the (005) peak is 0.3 °, showing a high degree of c-axis orientation. The ϕ-scan of the (104) reflection peaks of the $(Hg_{0.9}Re_{0.1})Ba_2CaCu_2O_{6+\delta}$ thin film verified the alignment of the a- and b-axes between film and substrate. The fourfold symmetry of the ϕ-scan reveals that the film deposited on STO has good in plane orientation. Further oxygen annealing did not improve the quality of the films.

After preparation and initial characterization, the films were patterned by photolithography and wet etching. The films exhibit sharp superconducting transitions at T_c= 124 K with transition width $\Delta T_c \simeq 2$ K. The resistive transitions have been investigated in magnetic fields up to 12 T parallel and perpendicular to the c-axis. The activation energy of thermally activated flux-motion for both magnetic field orientations have been determined. The field dependence of the activation energy follows a power law $U(B) \propto 1/B^{\alpha}$ with $\alpha = 0.57$ for $B \perp c$, in agreement with theoretical models. The $U(B)$ line for $(Hg_{0.9}Re_{0.1})Ba_2CaCu_2O_{6+\delta}$ films is comparable to those reported for other high T_c cuprates.

The irreversibility line for the $(Hg_{0.9}Re_{0.1})Ba_2CaCu_2O_{6+\delta}$ thin films has been deduced from the electrical resistance measurements and investigated as a function of reduced temperature (1-T/T_c). The result of the irreversibility line is compared with published data for other high T_c cuprates. At different temperatures magnetization loops were measured with a magnetic field applied normal to the film in a SQUID magnetometer and the corresponding critical current densities J_c were calculated. The calculated critical current density of the $(Hg_{0.9}Re_{0.1})Ba_2CaCu_2O_{6+\delta}$ films was 1.2×10^7 A/cm^2 at 5 K and $\approx 2 \times 10^6$ A/cm^2 at 77 K, which is in the range of the best results reported in literature.

Further, this work presents experimental results of the anisotropy of flux flow resistivity in $(Hg_{0.9}Re_{0.1})Ba_2CaCu_2O_{6+\delta}$ thin films. Under variation of the angle

θ between the field direction and the c-axis of the film, the anisotropic properties of the vortex state and the depinning field $B_{dp}(\theta)$ have been studied. The measured angular dependence $B_{dp}(\theta)$ shows a cusp for $\theta = 90\,^{\circ}$. The films exhibit a rather low critical field anisotropy of 7.7. The angular dependence $B_{dp}(\theta)$ close to T_c resembles the functional form expected for an anisotropic vortex flux liquid, which consists of pancake vortices and in-plane vortex segments. This way of determining the anisotropy yields an effective anisotropy of the material relevant for estimations of the useful range in the T-B-θ phase space of the material.
Systematic measurements of the longitudinal and Hall resistivities in $(Hg_{0.9}Re_{0.1})Ba_2CaCu_2O_{6+\delta}$ epitaxial thin films were performed. The magnetic field and the temperature dependence of the normal and mixed-state Hall effect have been measured in$(Hg_{0.9}Re_{0.1})Ba_2CaCu_2O_{6+\delta}$ HTSC thin films in fields up to 12 T with the magnetic field perpendicular to the ab plane and the current flowing in the ab plane. Measurements of the longitudinal and transversal resistivity were performed simultaneously. Above the critical temperature T_c, the longitudinal resistivity ρ_{xx} increases linearly with temperature, whereas the Hall resistivity ρ_{yx} varies inversely proportional to T. Near T_c and in fields below 3 T, a double sign reversal of the Hall resistivity is observed. The cotangent of the normal state Hall angle, namely cot $\theta_H = \alpha T^2 + \beta$, follows a universal $T^{\,2}$ dependence in all magnetic fields. Close to the zero-resistance state, the Hall resistivity ρ_{yx} scales to a power law of the longitudinal resistivity ρ_{xx}. The scaling behavior between ρ_{yx} and ρ_{xx} shows a strong field dependence. The scaling exponent β in ρ_{yx} =A ρ_{xx}^{β} increases from 1 to 1.7 as the field increases from 1 to 12 T. The total Hall conductivity for these compounds is well described by $\sigma_{yx}(B) = C_1/B + C_2B + C_3$. The successes mentioned above are the key element for the preparation of the $HgBa_2Ca_{n-1}Cu_nO_{2n+2+\delta}$ thin films.

Bibliography

[1] J. G. Bednorz and K. A. Müller, Z. Phys. B **64**, 189 (1986).

[2] H. Kamerlingh Onnes, Comm. Phys. Lab. Leiden **122**, 81 (1911).

[3] W. Meissner and R. Ochsenfeld, Naturwiss. **21**, 787 (1933).

[4] F. London and H. London, Proc. R. Soc. A **149**, 71 (1935).

[5] V. L. Ginzburg and L. Landau, Zh. Eksp. Teor. Fiz. **20**, 1064 (1950).

[6] H. Fröhlich, Phys. **79**, 845 (1950).

[7] E. Maxwell, Phys. Rev. **78**, 477 (1950).

[8] C. A. Reynolds, B. Serin, W. H. Wright, and L. B. Nesbitt, Phys. Rev. **78**, 487 (1950).

[9] J. Bardeen, L. N. Cooper, and J. R. Schrieffer, Phys. Rev. **108**, 1175 (1957).

[10] F. London, Superfluids, Wiley, New York, Vol. **1** (1950), Vol. **2** (1954), Dover, New York (1961).

[11] B. D. Josephson, Phys. Lett. **1**, 251 (1962).

[12] J. Gavaller, Appl. Phys. Lett. **23**, 480 (1973).

[13] R. J. Cava, A. Santoro, D. W. Johnson Jr., and W. W. Rhodes, Phys. Rev. B **35**, 6716 (1987).

[14] J. M. Tarascon, L. H. Greene, W. R. McKinnon, G. W. Hull, and T. H. Geballe, Science **235**, 1373 (1987).

[15] C. W. Chu, P. H. Hor, R. L. Meng, L. Gao, Z. J. Huang, and Y. Q. Wang, Phys. Rev. Lett. **58**, 405 (1987).

[16] M. K. Wu, J. R. Ashburn, C. J. Torng, P. H. Hor, R. L. Meng, L. Gao, Z. J. Huang, Y. Q. Wang, and C. W. Chu, Phys. Rev. Lett. **58**, 908 (1987).

[17] U. Endo, S. Koyama, and T. Kawai, Jpn. J. Appl. Phys. **27**, L1476 (1988).

[18] S. S. P. Parkin, V. Y. Lee, E. M. Engler, A. I. Nazzal, T. C. Huang, G. Gorman, R. Savoy, and R. Beyers, Phys. Rev. Lett. **60**, 2539 (1988).

[19] H. Maeda, Y. Tanaka, and M. Fukutomi, T. Asano, Jpn. J. Appl. Phys. **27**, L209 (1988).

[20] Z. Z. Sheng and A. M. Hermann, Nature **332**, 138 (1988).

[21] Z. Z. Sheng, W. Kiehl, J. Bennett, A. El Ali, D. Marsh, G. D. Mooney, F. Arammash, J. Smith, D. Viar, and A. M. Hermann, Appl. Phys. Lett. **52**, 1738 (1988).

[22] L. Gao, Z. J. Huang, R. L. Meng, P. H. Hor, J. Bechtold, Y. Y. Sun, C. W. Chu, Z. Z. Sheng, A. M. Hermann. Nature **332**, 623 (1988).

[23] R. M. Hazen, L. W. Finger, R. J. Angel, C. T. Prewitt, N. L. Ross, C. G. Hadidiacos, P. J. Heaney, D. R. Veblen, Sheng, A. El. Ali, and A. M. Hermann, Phys. Rev. Lett. **60**, 1657 (1988).

[24] D. D. Berkley, E. F. Skelton, N. E. Moulton, M. S. Osofsky, W. T. Lechter, V. M. Browning, and D. H. Liebenberg, Phys. Rev. B **47**, 5524 (1993).

[25] C. W. Chu, L. Gao, F. Chen, Z. J. Huang, R. L. Meng, and Y. Y. Xue, Nature **365**, 323 (1993).

[26] Z. Iqbal, T. Datta, D. Kirven, A. Lungu, J. C. Barry, F. J. Owens, A. G. Rinzler, D. Yang, and F. Reidinger, Phys. Rev. B **49**, 12322 (1994).

[27] A. Schilling, M. Cantoni, J. D. Guo, and H. R. Ott, Nature **363**, 56 (1993).

[28] A. Schilling, O. Jeandupeux, J. D. Guo, and H. R. Ott, Physica C **216**, 182 (1993).

[29] A. Schilling, O. Jeandupeux, S. Buchi, H. R. Ott, C. Rossel, Physica C **235-240**, 229 (1994).

[30] P. Dai, B. C. Chakoumakos, G. F. Sun, K. W. Wong, Y. Xin, and D. F. Lu, Physica C **243**, 201 (1995).

[31] For a review, see for example, J. S. Schilling and S. Klotz, in Physical Properties of High Temperature Superconductors III, edited by D. M. Ginsberg (World Scientific, Singapore, 1992), p 59; C. W. Chu et al., in Frontiers of High Pressure Research, edited by H. D. Hochheimer and R. D. Etters (Plenum, New York, 1991), p. 383; R. J. Wijngaarden et al., ibid., p. 399.

[32] E. V. Antipov, S. M. Loureiro, C. Chaillout, J. J. Capponi, P. Bordet, J. L. Tholence, S. N. Putilin, and M. Marezio, Physica C **215**, 1 (1993).

[33] B. A. Scott, E.Y. Suard, C.C. Tsuei, D.B. Mitzi, T.R. Mcguire, B.-H. Chen and D. Walker, Physica C **230**, 239 (1994).

[34] E. M. Kopnin, E. V. Antipov, J. J. Capponi, P. Bordet, C. Chaillout, S. de Brion, M. Marezio, A. P. Bobylev, and G. van Tendeloo, Physica C **243**, 239 (1994).

[35] L. Gao, Y. Y. Xue, F. Chen, Q. Xiong, R. L. Meng, D. Ramirez, C. W. Chu, J. H. Eggert, and H. K. Mao, Phys. Rev. B **50**, 4260 (1994).

[36] 1. J. Nagamatsu, N. Nakagawa, T. Muranaka, Y. Zenitani, and J. Akimitsu, Nature **410**, 63 (2001).

[37] R. D. Parks, Superconductivity (Marcel Dekker, Inc., New York, p.357, 1969).

[38] A. A. Abrikosov, J. Experim. Theoret. Phys. (USSR) **32**, 1442 (1957) (translation: Soviet Phys. JETP **5**, 1174 (1957).

[39] A. C. Rose-Innes and E. H. Rhoderick, Introduction to Superconductivity, Pergamon Press, Oxford 170 (1978).

[40] W. Buckel, VCH, Weinheim (1990)

[41] R. P. Huebener, Magnetic Flux Structures in Superconductors, edited by P. Fulde (Springer, Berlin, 1992).

[42] C. P. Bean, Phys. Rev. Lett. **8**, 250 (1962).

[43] C. P. Bean, Rev. Mod. Phys. **36**, 31 (1964).

[44] T.P. Sheahan, Introduction to High-Temperature Superconductivity, New York: Plenum Press (1994).

[45] T. T. M. Palstra, B. Batlogg, R. B. van Dover, L. F. Schneemeyer, J. V. Waszczak, Phys. Rev. B **41**, 6621 (1990).

[46] E. H. Brandt, Physica C **1**, 195 (1992).

[47] M. Kawasaki, K. Takahashi, T. Maeda, R. Tsuchiya, M. Shinohara, O. Ishiyama, T. Yonezawa, M. Yoshimoto, H. Koinuma, Science **266**, 1540 (1994).

[48] T. Nakamura, H. Inada, M. Iiyama, Jpn. J. Appl. Phys. **36**, 90 (1997).

[49] S.N. Putilin, E.V. Antipov, O. Chmaissem, and M. Marezio, Nature **362**, 226 (1993).

[50] A. Tsukamoto, T. Sugano, S. Adachi, and K. Tanabe, Appl. Phys. Lett. **73**, 990 (1998).

[51] L. Krusin-Elbaum, C.C. Tsuei, A. Gputa, Nature **373**, 679 (1995).

[52] Q.-R. Zhang, X.-J. Chen, Physica C **282-287**, 905 (1997).

[53] S. Uchida, Jpn. J. Appl. Phys. **32**, 3784 (1993).

[54] J. R. Waldram, 1996 Superconductivity of Metals and Cuprates, IOP Publishing Ltd.

[55] Z. Z. Shena and A. M. Hermann, Nature **332**, 138 (1988).

[56] C. W. Chu, IEEE Trans. Appl. Supercond. **7**, 80 (1997).

[57] S. N. Putilin, E. V. Antipov, and M. Marezio, Physica C **212**, 266 (1993).

[58] Y. S. Yao, Y. J. Su, W. Liu, Z. X. Liu, H. Gong, J. W. Li, G. H. Cao, F. Wu, Z. X. Zhao, Physica C **224**, 91 (1994).

[59] E. M. Kopnin, E. V. Antipov, J. J. Capponi, P. Bordet, C. Chaillout, S. de Brion, M. Marezio, A. P. Bobylev, and G .V. Tendeloo, Physica C **243**, 222 (1995).

[60] K. A. Lokshin, D. A. Pavlov, M. L. Kovba, E. V. Antipov, I. G. Kuzemskaya, L. F. Kulikova, V. V. Davydov, I. V. Morozov, and E. S. Itskevich, Physica C **300**, 71 (1998).

[61] E. V. Antipov, A. M. Abakumov, S. N. Putilin, Supercond. Sci. Technol. **15**, R31 (2002).

[62] V. Shelke, R. K. Singh, Supercond. Sci. Technol **10**, 58 (1996).

[63] C. Acha, S. M. Loureiro, C. Chaillout, J. L. Tholence, J. J. Capponi, M. Marezio, and M. Nunez-Regueiro, Solid State Comm. **102**, 1 (1997).

[64] T. Tatsuki, A. Tokiwa-Yamamoto, A. Fukuoka, T. Tamura, X.-J. Wu, Y. Moriwaki, R. Usami, S. Adachi, K. Tanabe, and S. Tanaka, Jpn. J. Appl. Phys. **35**, L205 (1996).

[65] D. Thopart, J. Hejtmanek, D. Pelloquin, C. Martin, A. Maignan, Physica C **336**, 143 (2000).

[66] P. C. W. Fung , J. C. L. Chow, and Z. L. Du, Elecrmckem. Soc. Proc. **95-9**, 91 (1995).

[67] J. C. L. Chow, P. C. W. Fung, C. C. Lam, and H. M. Shao, Supercond. Sci. Technol. **8**, 887 (1995).

[68] S. N. Putilin, I. Bryntse, and E. V. Antipov, Mat. Res. Bull. **26**, 1299 (1991).

[69] S. S. P. Parkin, V. Y. Lee, A. I. Nazzal, R. Savoy, T. C. Huang, G. Gorman, and R. Beyers, Phys. Rev. B **38**, 6531 (1988).

[70] B. A. Hunter, J. D. Jorgensen, J. L. Wagner, P. G. Radaelli, D. G. Hinks, H. Shaked, R. L. Hitterman, and R. B. Von Dreele, Physica C **221**, 1 (1994).

[71] P. G. Radaelli, J. L. Wagner, B. A. Hunter, M. A. Beno, G. S. Knapp, J. D. Jorgensen, and D. G. Hinks, Physica C **216**, 29 (1993).

[72] A. R. Armstrong, W. I. F. David, I. Gameson, P. P. Edwards, J. J. Capponi, P. Bordet, and M. Marezio, Phys. Rev. B **52**, 551 (1995).

[73] J. L. Wagner, P. G. Radaelli, D. G. Hinks, J. D. Jorgensen, J. F. Mitchell, B. Dabrowski, G. S. Knapp, and M. A. Beno, Physica C **210**, 447 (1993); Q. Huang, J. W. Lynn, R. L. Meng, and C. W. Chu, **218**, 356 (1993); and P. G. Radaelli, J. L. Wagner, B. A. Hunter, M. A. Beno, G. S. Knapp, J. D. Jorgensen, D. G. Hinks, **216**, 29 (1993).

[74] Deutscher G, Nature **397**, 410 (1999).

[75] Ya. G. Ponomarev, C. S. Khi, K. K. Uk, M. V. Sudakova, S. N. Tchesnokov, M. A. Lorenz, M. A. Hein, G. Muller, H. Piel, B. A. Aminov, A. Krapf, and W. Kraak Physica C **315**, 85 (1999).

[76] A. A. Abrikosov, Physica C **317-318** (Proc. of the Euroconference on Anomalous Complex Superconductors, held in Aghia Pelagia, Crete, Greece, Sep. 26-Oct. 3, 1998), 154 (1999).

[77] J. Halbritter, Journ. Low Temp. Phys. **105**, 1249 (1996).

[78] C. Phillips, Phys. Rev. Lett. **72**, 3863 (1994).

[79] K. Byczuk, J. Spalek, Phys. Rev. B **53**, R518 (1996).

[80] V. Z. Kresin, S. A. Wolf, and Y. N. Ovchinnikov, Phys. Rev. B **53**, 11831 (1996).

[81] X. Chen, Z. Xu, Z. Jiao, and Q. Zhang, Phys. Lett. A **229**, 247 (1997).

[82] A. J. Leggett, Phys. Rev. Lett. **83**, 392 (1999).

[83] S. Chakravarty, H.-Y. Kee, and K. Volker, Nature **428**, 53 (2004).

[84] J. Y. T. Wei, C. C. Tsuei, P. J. M. van Bentum, Q. Xiong, C. W. Chu, and M. K. Wu, Phys. Rev. B **57**, 3650 (1998).

[85] S. Chakravarty, A. Sudbo, P. W. Anderson, and S. Strong, Science **261**, 337 (1993).

[86] H. Kotegawa, Y. Tokunaga, K. Ishida, G. -q. Zheng, Y. Kitaoka, K. Asayama, H. Kito, A. Iyo, H. Ihara, K. Tanaka, K. Tokiwab, and T. Watanabeb, J. Phys. Chem. Solids **62**, 171 (2001).

[87] A. Perali, C. Castellani, C. D. Castro, and M. Grilli, Phys. Rev. B **54**, 16216 (1996).

[88] J. L. Tallon, J. W. Loram, G. V. M. Williams, J. R. Cooper, I. R. Fisher, J. D. Johnson, M. P. Staines, and C. Bernhard, physica status solidi (b) **215**, 531 (1999).

[89] S. A. Kivelson, E. Fradkin, V. J. Emery, Nature **393**, 550 (1998).

[90] C. M. Varma, Phys. Rev. Lett. **83**, 3538 (1999).

[91] S. Chakravarty, R. B. Laughlin, D. K. Morr, and C. Nayak, Phys. Rev. B **63**, 94503 (2001).

[92] S. Sachdev, Rev. Mod. Phys. **75**, 913 (2003).

[93] I. Bryntse, Studies of high temperature superconductors **23**, ISBN: 1-56072-472-2.

[94] V. A. Alyoshin, D.A. Mikhailova, and E.V. Antipov, Physica C **271**, 197 (1996).

[95] D. Sedmidubsky, J. Leitner, K. Knizek, and M. Nevriva, 15th ICCT, Porto, (1998).

[96] A. Sin, P. Odier, A. G. Cunha, M. T. D. Orlando, S. Piol, E. Baggio-Saitovictch, and X. Obradors, Supercond.Sci. and Technol. **12**, 1175 (1999).

[97] Y. Q. Wang, R. L. Meng, Y. Y. Sun, Z. J. Huang, K. Ross, and C. W. Chu, Appl. Phys. Lett. **63**, 3084 (1993).

[98] A. Gupta, J. Z. Sun, and C.C. Tsuei, Science **265**, 1075 (1994).

[99] C. C. Tsuei, A. Gupta, G. Trafas, and D. Mitzi, Science **263**, 1259 (1994).

[100] J. Z. Wu, S. H. Yun, A. Gapud, B. W. Kang, W. N. Kang, S. C. Tidrow, T. P. Monahan, X. T. Cui, and W. K. Chu, Physica C **277**, 219 (1997).

[101] Y. Yu, H. M. Shao, Z. Y. Zheng , A. M. Sun, M. J. Qin, X. N. Xu, S. Y. Ding, X. X. Yao, J. Zhou, Z. M. Ji, S. Z. Yang, and W. L. Zhang, Physica C **289**, 199 (1997).

[102] Z. L. Xiao, G. Jakob, B. Hensel, and H. Adrian, Physica C **341-348**, 2393 (2000).

[103] Y. Sun, J. D. Guo, X. L. Xu, G. J. Lian, Y. Z. Wang, and G. C. Xiong, Physica C **312**, 197 (1999).

[104] B. W. Kang, A. A. Gapud, X. Fei, T. Aytug, J. Z. Wu, Appl. Phys. Lett. **72**, 1766 (1998).

[105] S. H. Yun, J. Z. Wu, Appl. Phys. Lett. **68**, 862 (1996).

[106] F. Foong, B. Bedard, Q. L. Xu, S. H. Liou, Appl. Phys. Lett. **68**, 1153 (1996).

[107] Y. Tsabba, S. Reich, Physica C**254**, 21 (1995).

[108] W. N. Kang, R. L. Meng, C. W. Chu, Appl. Phys. Lett. **73**, 381 (1998).

[109] R. L. Meng, L. Beauvais, X. N. Zhang, Z. J. Huang, Y. Y. Sun, Y. Y. Xue, and C. W. Chu, Physica C **216**, 21 (1993).

[110] A. Yamamoto, M. Itoh, A. Fukuoka, S. Adachi, H. Yamauchi, and K. Tanabe, J. Mater. Res. **14**, 644 (1999).

[111] O. Chmaissem, Q. Huang, S. N. Putilin, M. Marezio and A. Santoro, Physica C **212**, 259 (1993).

[112] Q. M. Lin, Z. H. He, Y. Y. Sun, L. Gao, Y. Y. Xue, and C. W. Chu Physica C **254**, 207 (1995).

[113] A. Tokiwa-Yamamoto, K. Isawa, M. Itoh, S. Adachi, and H. Yamauchi, Physica C **216**, 250 (1993).

[114] M. Paranthaman, Physica C **222**, 7 (1994).

[115] H. M. Shao, L. J. Shen, J. C. Shen, X. Y. Hua, P. F. Yuan, and X. X. Yao, Physica C **232**, 5 (1994).

[116] R. Usami, S. Adachi, M. Itoh, T. Tatsuki, A. Tokiwa-Yamamoto, and K. Tanabe, Physica C **262**, 21 (1996).

[117] Y. Morwaki, T. Tatsuki, A. Tokiwa-Yamamoto, T. Tamura, S. Adachi, and K. Tanabe. J. Mater. Sci. Lett. **16**, 115 (1997).

[118] T. Tsuchiya, K. Fueki, Physica C **288**, 47 (1997).

[119] P. V. P. S. S. Sastry, K. M. Amm, D. C. Knoll, S. C. Peterson, C. H. Wolters, and J. Schwartz, J. Supercond. **11**, 49 (1998).

[120] P. V. S. Sastry, K. M. Amm, D. C. Knoll, S. C. Peterson, and J. Schwartz, Physica C **300**, 125 (1998).

[121] A. G. Cunha, M. T. D. Orlando, K. M. B. Alves, L. G. Martinez, F. G. Emmerich, and E. Baggio-Saitovitch, Physica C **356**, 97 (2001).

[122] K. Isawa, A. Tokiwa-Yamamoto, M. Itoh, S. Adachi, and H. Yamauchi, Physica C **217**, 11 (1993).

[123] R. Puzniak, J. Karpinski, A. Wisniewski, R. Szymczak, M. Angst, H. Schwer, R. Molinski, and E. M. Kopnin, Physica C **309**, 161 (1998).

[124] Ch. Wolters, K. M. Amm, Y. R. Sun, and J. Schwartz, Physica C **267**, 164 (1996).

[125] R. L. Meng, B. R. Hickey, Y. Y. Sun, Y. Cao, C. Kinalidis, J. Meen, Y. Y. Xue, and C. W. Chu, Physica C **260**, 1 (1996).

[126] K. Kishio, J. Shimoyama, A. Yoshikawa, K. Kitazawa, O. Chmaissem, and J. D. Jorgensen, J. Low Temp. Phys. **105**, 1359 (1996).

[127] J. C. Miller, R. F. Haglund, Jr. (Eds.) *Laser Ablation Mechanisms and Applications*, Proceedings, Oak Ridge, TN, USA, Springer-Verlag (1991).

[128] Gupta, A. In Pulsed Laser Deposition of Thin Films; Chrisey, D. B., Hubbler, G. K., Eds; Wiley: New York, 265 (1994).

[129] J. T. Cheung, H. Sankur, CRC Crit. Rev. Sol. St. Mat. Sci. **15**, 63 (1988).

[130] H. Sankur, J. T. Cheung, Appl. phys. A **A47**, 271 (1988).

[131] D. J. Ehrlich, J. Y. Tsao, *laser Microfabrication* (*Film Processes and Lithography*), Academic Press, Boston, (1989).

[132] R. J. Cava, B. Batlogg, J. J. Krajewski, R. Farrow, L. W. Jr. Rupp, A. E. White, K. Short, W. F. Peck, and T. Kometani, Nature **332**, 814 (1988).

[133] M. A. Subramanian, J. Gopalakrishnan, C. C. Torardi, T. R. Askew, R. B. Flippen, A. W. Sleight, J. J. Lin, and S. J. Poon, Science **240**, 495 (1988).

[134] J. Hofer, J. Karpinski, M. Willemin, G. I. Meijer, E. M. Kopnin, R. Molinski, H. Schwer, C. Rossel, and H. Keller, Physica C **297**, 103 (1998).

[135] K. Fujinami, H. Suematsu, M. Karppinen, and H. Yamauchi, Physica C **307**, 202 (1998).

[136] W. N. Kang, S.-I. Lee, C. W. Chu, Physica C **315**, 223 (1999).

[137] W. Kraus and G. Nolze, J. Appl. Cryst. **29**, 301 (1996).

[138] L. Méchin, P. Berghuis, and J. E. Evetts, Physica C **302**, 102 (1998).

[139] R. Rössler, J. D. Pedarnig, D. Bäuerle, E. J. Connolly, and H. W. Zandbergen, Applied Physics A **71**, 245 (2000).

[140] P. Wagner, F. Hillmer, U. Frey, H. Adrian, T. Steinborn, L. Ranno, A. Elschner, I. Heyvaert, and Y. Bruynseraede, Physica C **215**, 123 (1993).

[141] F. Gömöry, Supercond. Sci. Technol. **10**, 523 (1997).

[142] P. W. Anderson, Phys. Rev. Lett. **9**, 309 (1962).

[143] P. W. Anderson and Y. B. Kim, Rev. Mod. Phys. **36** 39 (1964).

[144] Y. B. Kim, C. F. Hempstead, A. R. Strnad, Phys. Rev. Lett. **9**, 306 (1962); Y. B. Kim, C. F. Hempstead, A. R. Strnad, Phys. Rev. **129**, 528 (1963).

[145] M. Tinkham, *Introduction to superconductivity*, 2nd ed.(McGraw-Hill, New York, 1996).

[146] M. R. Beasley, R. Labusch, and W. W. Webb, Phys. Rev. **181**, 682 (1969).

[147] Y. Yeshurn, A. P. Malozemoff, Phys. Rev. Lett. **60**, 2202 (1988).

[148] M. Tinkham, Phys.Rev. Lett. **61**, (1988) 1658.

[149] R. Ikeda, T. Chmi, T. Tsuneto, J. Phys. Soc. Jpn. **60**, 1051 (1991).

[150] D. S. Fisher, M. P. A. Fisher, D. A. Huse, Phys. Rev. B **43**, 130 (1991).

[151] Y. Iye, T. Tamegai, H. Takeya, H. Takei Jpn. J. Appl. Phys. pt. **226**, L1850 (1987).

[152] J. R. Thompson, Y. R. Sun, H. R. Kerchner, D. K. Christen, B. C. Sales, B. C. Chakoumakos, A. D. Marwick, L. Civale, and J. O. Thompson, Appl. Phys. Lett. **60**, 2306 (1992).

[153] L. Civale, A. D. Marwick, T. K. Worthington, M. A. Kirk, J. R. Thompson, L. Krusin-Elbaum, Y. Sun, J. R. Clem, and F. Holtzberg Phys. Rev. Lett. **67**, 648 (1991).

[154] V. Geshkenbein, A. Larkin, M. Feigelman, V. Vinokur, Physica C **162-164**, 239 (1989).

[155] N. Y. Fogel, V. G. Cherkasova, O. A. Koretzkaya, A. S. Sidorenko, Phys. Rev. B **55**, 85 (1997).

[156] K. C. Woo, K. E. Gray, R. T. Kampwirth, J. H. Kang, S. J. Stein, R. East, D. M. McKay, Phys. Rev. Lett. **63**, 1877 (1989).

[157] H. Yamasaki, K. Endo, S. Kosaka, M. Umeda, S. Yoshida, K. Kajimura, Phys. Rev. Lett. **70**, 3331 (1993).

[158] J. T. Kucera, T. P. Orlando, G. Virshup, J. N. Eckstein, Phys. Rev. B **46**, 11004 (1992).

[159] J. S. Satchell, R. G. Humphreys, N. G. Chew, J. A. Edwards, M. J. Kane, Nature **334**, 331 (1988).

[160] S. Zhu, D. K. Christen, C. E. Klabunde, J. R. Thompson, E. C. Jones, R. Feenstra, D. H. Lowndes, and D. P. Norton, Phys. Rev. B **46**, 5576 (1992).

[161] T. T. M. Palstra, B. Batlogg, R. B. van Dover, L. F. Schneemeyer, and J. V. Waszczak, Appl. Phys. Lett. **54**, 763 (1989).

[162] Y. Moriwaki, T. Sugano, A. Tsukamoto, C. Gasser, K. Nakanishi, S. Adachi, and K. Tanabe, Physica C **303**, 65 (1998).

[163] H. Takei, H. Kugai, Y. Torii, K. Tada, Physica C **210**, 109 (1993).

[164] M. Rupp, A. Gupta, and C. C. Tsuei, Appl. Phys. Lett. **67**, 291 (1995).

[165] T. Nabatame, J. Sato, Y. Saito, K. Aihara, T. Kamo, and S. Matsuda, Physica C **193**, 390 (1192).

[166] J. Löhle, J. Karpinski, A. Morawski, and P. Wachter, Physica C**266**, 104 (1996).

[167] A. Salem, G. Jakob, and H. Adrian, Physica C **402**, 354 (2004).

[168] V. Vulcanescu, L. Fruchter, A. Bertinotti, D. Colson, G. Le Bras, and J.-F. Marucco, Physica C **259**, 131 (1996).

[169] J. R. Clem, Supercond. Sci. Technol. **11**, 909 (1998).

[170] R. Puzniak, R. Usami, K. Isawa, H. Yamauchi, Phys. Rev. B **52**, 3756 (1995).

[171] Y.-R. Sun, J. Schwartz, Phys. Rev. B **53**, 5830 (1996).

[172] M. S. Kim, S. I. Lee, S. C. Yu, N.H. Hur, Phys. Rev. B **53**, 9460 (1995).

[173] Y. S. Song, M. Hirabayashi, H. Ihara, M. Tokumoto, Phys. Rev. B **50**, 16644 (1994).

[174] Y. C. Kim, J. R. Thompson, J. G. Ossandon, D. K. Christen, M. Paranthaman, Phys. Rev. B **51**, 11767 (1995).

[175] M. Couach, A.F. Khoder, R. Calemczuk, Ch. Marcenat, J.L. Tholence, J. J. Capponi, M.F. Gorius, Phys. Lett. A **188**, 85 (1994).

[176] G. Lebras, J. Hammann, A. Bertinotti, D. Colson, A. Forget, J. Marucco, V. Viallet, Czech. J. Phys. **46**, 1769 (1996).

[177] D. Zech, J. Hofer, H. Keller, C. Rossel, P. Bauer, J. Karpinski, Phys. Rev. B **53**, R6026 (1996).

[178] Y. Iye, S. Nakamura, T. Tamegai, Physica C **159**, 433 (1988).

[179] Y. Iye, S. Nakamura, T. Tamegai, T. Terashima, Y. Bando, Physica C **185-189**, 273 (1991).

[180] Y. Iye, S. I. Oguro, T. Tamegai, W. R. Datars, N. Motohira, K. Kitazawa, Physica C **199**, 154 (1991).

[181] J. N. Li, K. Kadowaki, Z. Tranawski, Z. Koziol, J. J. M. Franse, Physica C **161**, 313 (1989).

[182] J. N. Li, K. Kadowaki, Z. Tranawski, Z. Koziol, J.J. M. Franse, Physica C **185-189**, 1875 (1991).

[183] H. Raffy, S. Labdi, O. Laborde, P. Monceau, Phys. Rev. Lett. **66**, 2515 (1991).

[184] A. Walkenhorst, C. Tom-Rosa, C. Stlzel, G. Jakob, M. Schmitt, and H. Adrian Physica C **177**, 165 (1991).

[185] C. M. Fu, V. V. Moshchalkov, W. Boon, K. Temst, Y. Bruynseraede, G. Jakob, T. Hahn, H. Adrian, Physica C **205**, 111 (1993).

[186] J. Bardeen, M. J. Stephen, Phys. Rev. B **140**, A1197 (1965).

[187] A. Walkenhorst, Master's thesis, TH Darmstadt (1990).

[188] G. Blatter, V. B. Geshkenbein, A. I. Larkin, Phys. Rev. Lett **68**, 875 (1992).

[189] V. P. Mineev, Phys. Rev. B **65**, 012508 (2001).

[190] V. G. Kogan. Phys. Rev. B **38**, 7049 (1988).

[191] M. W. Coffey and Z. Hao. Phys. Rev. B **44**, 5230 (1991).

[192] M. Tachiki and S. Takahashi. Solid State Commun. **70**, 291 (1989).

[193] M. Tachiki and S. Takahashi. Solid State Commun. **72**, 1083 (1989).

[194] G. Jakob, Ph.D. thesis, TH Darmstadt (1993).

[195] D. Feinberg, Physica C **194**, 126 (1992).

[196] R. P. Huebener 1979 Magnetic Flux Structure in Superconductors (Berlin: Springer).

[197] H. Obara, S. Kosaka, Y. Yokoyama, M. Umeda, and Y. Kimura, Phys. Rev. B **44**, 4532 (1991).

[198] C. J. Liu, C. Schlenker, J. Schubert, and B. Stritzker, Phys. Rev. B **48**, 911 (1993).

[199] G. Fuchs, E. S. Vlakhov, K. A. Nenkov, T. Staiger, and A. Gladun Physica C **247**, 340 (1995).

[200] P. J. Kung, M. E. McHenry, M. P. Maley, P. H. Kes, D. E. Laughlin, and W. W. Mullins, Physica C **249**, 53 (1995).

[201] D. Majer, E. Zeldov, and M. Konczykowski, Phys. Rev. Lett. **75**, 1166 (1995).

[202] Y. Xu, M. Suenaga, A. R. Moodenbaugh, and D. O. Welch, Phys. Rev. B **40**, 882 (1989).

[203] J. R. Clem. Rev. B **43**, 7837 (1991).

[204] D. H. Kim, K. E. Gray, R. T. Kampwirth, J. C. Smith, D. S. Richeson, T. J. Marks, J. H. Kang, J. Talvacchio, and M. Eddy, Physica C **177**, 431 (1991).

[205] M. Xu, D. Shi, and R.F. Fox, Phys. Rev. Lett. **42**, 10773 (1990).

[206] L. T. Sagdahl, S. Gjolmesli, T. Laegreid, K. Fossheim, and W. Assmus, Phys. Rev. B **42**, 6797 (1990).

[207] L. W. Lombardo, D. B. Mitzi, A. Kapitulnik, and A. Leone, Phys. Rev. B **46**, 5615 (1992).

[208] Z. J. Huang, Y. Y. Xue, R. L. Meng, and C. W. Chu, Phys. Rev. B **49**, 4218 (1994).

[209] J. B. Shi, B. S. Ch'IOU, and H. C. Ku, Jpn. J. Appl. Phys. **31**, L461 (1992).

[210] P. de Rango, B. Giordanengo, Ft. Tournier, A. Sulpice, J. Chaussy, G. Deutscher, J. L. Genicon, P. Lejay, R. Redou, B. Raveu, and L. Miu, Phys. Rev. B **46**, 1172 (1992).

[211] M. F. Tai, G. F. Chang, and M. W. Lee, Phys. Rev. B **52**, 1176 (1995).

[212] Y. Yeshurun and A. P. Malozemoff, Phys. Rev. Lett. **60**, 2202 (1987).

[213] D. R. Nelson, Phys. Rev. Lett. **60** (1988) 1973; A. Houghton, R. A. Pecovits, and A. Sudb, Phys. Rev. B **40**, 6763 (1989).

[214] M. P. A. Fisher, Phys. Rev. Lett. **62** (1989) 1415; D. Fisher, M. P. A. Fisher, and D. A. Huse, Phys. Rev. B **43**, 130 (1990).

[215] Y. Moriwaki, T. Sugano, S. Adachi, K.Tanabe, and A. Tsukamoto, IEEE Tras. Appl. Superconductivity **9**, 2390 (1999).

[216] U. Welp, G. W. Crabtree, J. L. Wagner, D. G. Hinks, P. G. Radaelli, J. D. Jorgensen, and J. F. Mitchell, Appl. Phys. Lett. **63**, 693 (1993).

[217] J. R. Thompson, L. Krusin-Elbaum, D. K. Christen, K. J. Song, M. Paranthaman, J. L. Ullmann, J. Z. Wu, Z. F. Ren, J. H. Wang, J. E. Tkaczyk, and J. A. DeLuca, Appl. Phys. Lett. **71**, 536 (1997).

[218] J. L. Tallon, C. Bernhard, Ch. Niedermayer, J. Shimoyama, S. Hahakura, K. Yamaura, Z. Hiroi, M. Takano, K. Kishio, J. Low Temp. Phys. **105**, 1379 (1996).

[219] K.-Yvon and M. Francois, Z. Phys. B **76**, 413 (1989).

[220] C. Cantoni, A. Schilling, N.-U. Nissen, and H. R. Ott, Physiea C **215**, 11 (1993).

[221] N. Chikumoto, M. Konczykowski, N. Motohira, A.P. Malozemoff, Phys. Rev. Lett. **69**, 1260 (1992).

[222] B. A. Willemsen, J. S. Derov, and S. Sridhar, Phys. Rev. B **56**, 11989 (1997).

[223] S. L. Yan, Y. Y. Xie, J. Z. Wu, T. Aytug, A. A. Gapud, B. W. Kang, L. Fang, M. He, S. C. Tidrow, K. W. Kirchner, J. R. Liu, W. K. Chu, Appl. Phys. Lett. **73**, 2989 (1998).

[224] G. Blatter, M. V. Feigel'man, V. B. Geshkenbein, A. I. Larkin, and V. W. Vinokur, Rev. Mod. Phys. **66**, 1125 (1994).

[225] T. Matsushita, E. S. Otabe, B. Ni, T. Hikata, and K. Sato, Cryogenics **31**, 949 (1991).

[226] H. J. Jensen, J. Phys. Condens. Matter **6**, L149 (1994).

[227] Y. Tokura, H. Takagi, and S. Uchida, Nature **337**, 345 (1989).

[228] H. Takagi, S. Uchida, and Y. Tokura, Phys. Rev. Lett. **62**, 1197 (1989).

[229] S. J. Hagen, A. W. Smith, M. Rajeswari, J. L. Peng, Z. Y. Li, R. L. Greene, S. N. Mao, X. X. Xi, S. Bhattacharya, Qi Li, and C. J. Lobb. Phys. Rev. B **47**, 1064 (1993).

[230] W. Liu, T. W. Clinton, A. W. Smith and C. J. Lobb, Phys. Rev. B **55**, 11802 (1997).

[231] S. N. Artemenko, I. G. Gorlova, and Yu. I. Latyshev, Phys. Lett. A **138**, 428 (1989).

[232] S. J. Hagen, C. J. Lobb, R. L. Greene, and M. Eddy, Phys. Rev. B **43**, 6246 (1991).

[233] W. N. Kang, S. H. Yun, J. Z. Wu, and D. H. Kim, Phys. Rev. B **55**, 621 (1997).

[234] M. Galffy and E. Zirgiebl. Solid State Commun. **68**, 929 (1988).

[235] W. Gob, W. Liebich, W. Lang, I. Puica, R. Sobolewski, R. Rossler, J. D. Pedarnig, and D. Bauerle, Phys. Rev. B **62**, 9780 (2000).

[236] W. N. Kang, B. W. Kang, Q. Y. Chen, J. Z. Wu, Y. Bai, W. K. Chu, D. K. Christen, R. Kerchner and S.-I. Lee, Phys. Rev. B **61**, 722 (2000).

[237] N. B. Kopnin, Phys. Rev. B **54**, 9475 (1996).

[238] P. Nozieres, W.F. Vinen, Philos. Mag. **14**, 667 (1966).

[239] N. B. Kopnin, B. I. Ivlev and V. A. Kalatsky, J. Low Temp. Phys. **90**, 1 (1993).

[240] V. Berseth, Ph.D. thesis, Lausanne, EPFL (1999).

[241] B. D. Josephson, Phys. Letters **16**, 242 (1965).

[242] Wang, Z. D. and Ting, C. S. Phys. Rev. Lett. **67**, 3618 (1991).

[243] V. M. Vinokur, V. B. Geshkenbein, M. V. Feigelman, and G. Blatter , Phys. Rev. Lett.**71**, 1242 (1993).

[244] Bhattacharya, S., Higgins, M. J., and Ramakrishnan, T. V. Phys. Rev. Lett. **73**, 1699 (1994).

[245] Z. D. Wang, J. Dong, and C. S. Ting, Phys. Rev. Lett. **72**, 3875 (1994).

[246] M. V. Feigel'man, V. B. Geshkenbein, A. I. Larkin, and V. M. Vinokur, JETP Lett. **62**, 835 (1995).

[247] J. Luo, T. P. Orlando, J. M. Graybeal, X. D. Wu, R. Muenchausen, Phys. Rev. Lett **68**, 690 (1992).

[248] J. P. Rice, N. Rigakis, D. M. Ginsberg, J. M. Mochel, Phys. Rev. B **46**, 11050 (1992).

[249] A. V. Samoilov, Phys. Rev. Lett **71**, 617 (1993).

[250] R. C. Budhani, S. H. Liou and Z. X. Cai. Phys. Rev. Lett. **71**, 621 (1993).

[251] A. V. Samoilov, Z. G. Ivanov, and L.-G. Johansson, Phys. Rev. B **49**, 3667 (1994).

[252] M. Cagigal, J. Fontcuberta, M. A. Crusellas, J. L. Vicent, and S. Piol, Physica C **248**, 155 (1995).

[253] P. W. Anderson, Phys. Rev. Lett.**67**, 2092 (1991).

[254] T. R.Chien, Z. Z. Wang, and N. P. Ong, Phys. Rev. Lett.**67**, 2088 (1991).

[255] Y. Ando, Y. Kurita, S. Komiya, S. Ono, and K. Segawa, Phys. Rev. Lett. **92**, 197001 (2004).

[256] A. Salem, G. Jakob, and H. Adrian, Physica C **415**, 62 (2004).

[257] J. Roa-Rojas, P. Pureur, L. Mendona-Ferreira, M. T. D. Orlando, and E Baggio-Saitovitch, Supercond. Sci. Technol. **14**, 898 (2001).

[258] M. Cagigal, A. Seffar, J. Fontcuberta, M. A. Crusellas, J. L. Vincent, and S. Piol, Physica C **235-240**, 3177 (1994).

[259] W. Lang, W. Göb, I. Puica, and R. Sobolewski, Physica C **341**, 1829 (2000).

[260] T. S. Kayed, Cryst. Res. Technol. **38**, 946 (2003).

[261] R. Jin, M. Paranthaman, H. Y. Zhai, H. M. Christen, D. K. Christen, and D. Mandrus, Phys. Rev. B **64**, 220506(R) (2001).

[262] A. T. Dorsey and M. P. A. Fisher, Phys. Rev. Lett.**68**, 694 (1992).

[263] A. T. Dorsey, Phys. Rev. B**46**, 8376 (1992).

[264] P. W. Anderson, The Theory of Superconductivity in High-Tc Cuprates, Princeton University Press, New Jersey, (1997).

[265] J. M. Harris, H. Wu, N. P. Ong, R. L. Meng, and C. W. Chu, Phys. Rev. B **50**, 3246 (1994).

[266] For a review, see N. P. Ong, in Physical Properties of High-Temperature Superconductors, edited by D. M. Ginsberg, World Scientific, Singapore, 459 (1990).

[267] W. N. Kang, Wan-Seon Kim, Sung-Ik Lee, B. W. Kang, J. Z. Wu, Q. Y. Chen, W. K. Chu, and C. W. Chu, Physica C **341-348**, 1235 (2000).

[268] J. C. Chen, Yunhui Xu, M. K. Wu, Weiyan Guan, Phys. Rev. B, 5839 **53** (1996).

[269] P. Xiong and G. Xiao, Phys. Rev. B**47**, 5516 (1993).

[270] W. N. Kang, B. W. Kang, Q. Y. Chen, J. Z. Wu, S. H. Yun, A. Gapud, J. Z. Qu, W. K. Chu, D. K. Christen, R. Kerchner, and C. W. Chu, Phys. Rev. B**59**, R9031 (1999).

[271] Y. Eltsev and Ö. Rapp, Phys. Rev. B **57**, 3237 (1998).

[272] H. C. Yang, L. M. Wang, and H. E. Horng, Phys. Rev. B **56**, 99 (1997).

[273] W. N. Kang , D. H. Kim, S. Y. Shim, J. H. Park, T. S. Hahn, S. S. Choi, W. C. Lee, J. D. Hettinger, K. E. Gray, and B. Glagola , Phys. Rev. Lett. **76**, 2993 (1996).

[274] G. D'Anna, V. Berseth, L. Forro, A. Erb, and E. Walker, Phys. Rev. B**61**, 4215 (2000).

[275] S. Ullah and A. T. Dorsey, Phys. Rev. B**44**, 262 (1991).

[276] R. J. Troy and A. T. Dorsey, Phys. Rev. B **47**, 2715 (1993).

[277] D. M. Ginsberg and J.T. Manson, Phys. Rev. B **51**, 515 (1995).

[278] X. G. Qiu, G. Jakob, V. V. Moshchalkov, Y. Bruynseraede, and H. Adrian, Phys. Rev. B **52**, 12994 (1995).

[279] C. C. Almasan, S. H. Han, K. Yoshiara, M. Buchgeister, D. A. Gajewski, L. M. Paulius, J. Herrmann, M. B. Maple, A. P. Paulikas, Chun Gu, and B. W. Veal, Phys. Rev. B **51**, 3981 (1995).

[280] Y. Matsuda, T. Nagaoka, G. Suzuki, K. Kumagai, M. Suzuki, M. Machida, M. Sera, M. Hiroi, and N. Kobayashi, Phys. Rev. B **52**, 15749 (1995).

[281] W.-S. Kim, W. N. Kang, S. J. Oh, M.-S. Kim, Y. Bai, S.-I. Lee, C. H. Choi, and H.-C. Ri, Physica C **324**, 77 (1999).

[282] J. M. Harris, N. P. Ong, P. Matl, R. Gagnon, L. Taillefer, T. Kimura, and K. Kitazawa, Phys. Rev. B **51**, 12053 (1995).

List of Publications

Publications closely related to the present work:

Resistivity and irreversibility line of $(Hg_{0.9}Re_{0.1})Ba_2CaCu_2O_{6+\delta}$ HTSC thin films
Abouelwafa Salem, Gerhard Jakob, and Hermann Adrian,Physica C **388-389**, 747 (2003).

Superconductivity in high-quality $(Hg_{0.9}Re_{0.1})Ba_2CaCu_2O_{6+\delta}$ HTSC thin films
Abouelwafa Salem, Gerhard Jakob, and Hermann Adrian, Phys. Stat. Sol. (c) **1**, 1961 (2004).

Preparation, scaling behavior of activation energy, Hall effect, and flux- flow anisotropy of thin films
Abouelwafa Salem, Gerhard Jakob, and Hermann Adrian , Physica C **402/4**, 354 (2004).

Normal and mixed state Hall effect in $(Hg_{0.9}Re_{0.1})Ba_2CaCu_2O_{6+\delta}$ fully textured HTSC thin films
Abouelwafa Salem, Gerhard Jakob, and Hermann Adrian, Physica C **415**, 62 (2004).

Mixed-state Hall Angle in $(Hg_{0.9}Re_{0.1})Ba_2CaCu_2O_{6+\delta}$ superconducting thin films
Abouelwafa Salem, Gerhard Jakob, and Hermann Adrian, Submitted to Phys.

Stat. Sol. (c).

Temperature behavior of the Hall conductivity in $(Hg_{0.9}Re_{0.1})Ba_2CaCu_2O_{6+\delta}$ superconducting thin films
Abouelwafa Salem, Gerhard Jakob, and Hermann Adrian, Submitted to Physica C .

Additional publications related to the field of semiconductors:
thermal and electrical transport properties of Tl_2Te single crystals
Gamal Ata, Abouelwafa Salem, M. M. Nassary, and A. T. Nagat, Semicond. Sci. Technol. **11**, 516 (1996).

Some physicals properties of Ga_2Se single crystals
Gamal Ata, Abouelwafa Salem, M. M. Nassary, and A. T. Nagat, Cryst. Res. Technol. **31**, 350 (1996).

Scientific meetings and talks closely related to the present work:

German Physical Society, Spring meeting, University of Regensburg, Germany, March 11-15, 2002.

23rd International Conference on Low Temperature Physics (LT23), Hiroshima, Japan, August 20-27, 2002.

German Physical Society, Spring meeting, University of Dresden, Germany, March 24-28, 2003.

International Conference on Superconductivity and Magnetism (MSM03), Monastir, Tunisia, September 1-4, 2003.

German Physical Society, Spring meeting, University of Regensburg, Germany, March 8-12, 2004.

20th General Conference of the CONDENSED MATTER DIVISION of the European Physical Society, Prague, Czech Republic, 19-23 July, 2004.

Eidesstattliche Erklärung

Hiermit erkläre ich an Eides Statt, daß ich die vorliegende Arbeit selbstsändig und nur unter Verwendung der angegebenen Hilfsmittel angefertigt habe.

Bisher habe ich noch keinen Promotionsversuch unternommen.

Mainz, Dezember 2004